2D AND 3D UNSTEADY AERODYNAMIC ANALYSIS OF A VERY LIGHT AIRCRAFT'S WING

A THESIS SUBMITTED TO
THE GRADUATE SCHOOL OF NATURAL AND APPLIED SCIENCES
OF
MIDDLE EAST TECHNICAL UNIVERSITY

BY

BERKAN ANILIR

IN PARTIAL FULFILLMENT OF THE REQUIREMENTS
FOR
THE DEGREE OF MASTER OF SCIENCE
IN
AEROSPACE ENGINEERING

JULY 2023

Approval of the thesis:

2D AND 3D UNSTEADY AERODYNAMIC ANALYSIS OF A VERY LIGHT AIRCRAFT'S WING

submitted by **BERKAN ANILIR** in partial fulfillment of the requirements for the degree of **Master of Science** i**n Aerospace Engineering, Middle East Technical University** by,

Prof. Dr. Halil Kalıpçılar
Dean, Graduate School of **Natural and Applied Sciences** _____

Prof. Dr. Serkan Özgen
Head of the Department, **Aerospace Engineering, METU** _____

Prof. Dr. Dilek Funda Kurtuluş
Supervisor, **Aerospace Engineering, METU** _____

Examining Committee Members:

Prof. Dr. Ozan Tekinalp
Aerospace Engineering, METU _____

Prof. Dr. Dilek Funda Kurtuluş
Aerospace Engineering, METU _____

Assoc. Prof. Dr. Nilay Sezer Uzol
Aerospace Engineering, METU _____

Asst. Prof. Dr. Özge Başkan Perçin
Aerospace Engineering, METU _____

Asst. Prof. Dr. Emre Kara
Aerospace Engineering, Gaziantep University _____

Date: 17.07.2023

I hereby declare that all information in this document has been obtained and presented in accordance with academic rules and ethical conduct. I also declare that, as required by these rules and conduct, I have fully cited and referenced all material and results that are not original to this work.

Name Last name : Berkan Anılır

Signature :

ABSTRACT

2D AND 3D UNSTEADY AERODYNAMIC ANALYSIS OF A VERY LIGHT AIRCRAFT'S WING

Anılır, Berkan
Master of Science, Aerospace Engineering
Supervisor : Prof. Dr. Dilek Funda Kurtuluş

July 2023, 101 pages

The aim of this thesis is to investigate the unsteady aerodynamics of designed Very Light Aircraft (VLA)'s wing starting from its airfoil to whole wing with numerical simulations. In this regard, Unsteady Reynolds-averaged Navier-Stokes (URANS) simulations have been performed for a single 2D SD7062 airfoil, 2D SD7062 airfoil with a $0.30c$ high cambered single-slotted flap and 3D Very Light Aircraft's wing. In 2D SD7062 airfoil simulation at cruise Reynolds number of 5×10^6, the aerodynamic coefficients, laminar separation bubble parameters, time-averaged velocity streamlines and vortex patterns are revealed and discussed in detail. Also, two-dimensional analyses are compared with the three-dimensional analyses at various pre- and post-stall regimes. In 2D SD7062 airfoil with a flap simulations at cruise, takeoff and landing condition, the influence of flap deflection on the aerodynamic coefficients and unsteady flowfiled are observed. The optimum gap size at landing condition with 35° flap deflection is studied to reach the maximum lift coefficient. In 3D wing simulations at cruise condition, the impact of taper ratio, dihedral angle and wing tip shape on the aerodynamics of a Very Light Aircraft's wing has been investigated. Since the post-stall regimes are also

explored, the stall cell formation is observed just above the stall angle as evident in the mean surface streamlines. The stall cell characteristics with respect to different wing design variables and angles of attack are represented and their effects on the sectional lift distributions and total aerodynamic coefficients are discussed.

Keywords: Unsteady flow, Computational fluid dynamics, Very Light Aircraft, SD7062, Wing design.

ÖZ

ÇOK HAFİF BİR UÇAĞIN KANADININ ZAMANA BAĞLI 2B VE 3B AERODİNAMİK ANALİZİ

Anılır, Berkan
Yüksek Lisans, Havacılık ve Uzay Mühendisliği
Tez Yöneticisi: Prof. Dr. Dilek Funda Kurtuluş

Temmuz 2023, 101 sayfa

Bu tezin amacı, tasarlanmış Çok Hafif Hava Aracı'nın (VLA) kanadının zamana bağlı aerodinamik özelliklerini, kanat profilinden başlayarak tüm kanada kadar nümerik simülasyonlarla incelemektir. Bu bağlamda, tek bir 2B SD7062 kanat kesidi, 0.30 yükseklikli oluklu kanatçığa sahip 2B SD7062 kanat kesidi ve 3B Hafif Hava Aracı'nın kanadı için Zamana Bağlı Reynolds Ortalama Navier-Stokes (URANS) simülasyonları gerçekleştirilmiştir. 2B SD7062 hava kanadı profili simülasyonunda 5×10^6 seyir Reynolds sayısında aerodinamik katsayılar, laminar ayrılma baloncuğun parametreleri, ortalama hızlı akış çizgileri ve iz akış desenleri ayrıntılı bir şekilde ortaya konulmuş ve detaylı olarak tartışılmıştır. Ayrıca, iki boyutlu analizler çeşitli ön ve son taşıma kaybı (stall) rejimlerinde üç boyutlu analizlerle karşılaştırılmıştır. 2B SD7062 kanat profili ile kanatçık simülasyonlarında seyir, kalkış ve iniş koşullarında kanatçık eğiminin aerodinamik katsayılar ve zamana bağlı akış alanı üzerindeki etkisi gözlemlenmiştir. İniş koşulunda 35° flap eğimiyle maksimum taşıma katsayısına ulaşmak için optimum açıklık boyutu araştırılmıştır. Seyir koşulunda 3B kanat simülasyonlarında, Hafif Hava Aracı'nın kanadının aerodinamiği üzerinde sivrilme oranı, dihedral açısı ve kanat ucunun şeklinin etkisi araştırılmıştır. Taşıma kaybı (stall) sonrası rejimleri de

incelendiğinden, yüzeydeki ortalama iz akış hatlarında belirgin olan stall açısının hemen üzerinde stall hücresi oluşumu gözlemlenmiştir. Farklı kanat tasarım değişkenlerine ve hücum açılarına bağlı olarak stall hücresi özellikleri temsil edilmekte ve kesitteki taşıma kuvveti dağılımları ve toplam aerodinamik katsayılar üzerindeki etkileri tartışılmaktadır.

Anahtar Kelimeler: Zamana bağlı akış, Hesaplamalı akışkanlar dinamiği, Çok Hafif Uçak, SD7062, Kanat tasarımı.

To my parents, and my sweet love Aysu

ACKNOWLEDGMENTS

I am deeply grateful to my advisor Prof. Dr. Dilek Funda Kurtuluş for her constant support, guidance and encouragement. Her knowledge and persistence have been of immeasurable value to me and have been essential to the accomplishment of not only my thesis but also my entire academic career. I could not have had a better advisor.

I devote this thesis to my immortal beloved Aysu Papurcu who is the real joy and happiness of my life. I will never be able to thank her enough for the sacrifices she made throughout this process. Your encouragement and support are what made this thesis possible.

I would like to thank wholeheartedly my parents, Gülseren and Rafet, my sister, Tuğçe, and express my endless love to my niece Alptuğ Aras. This study would not be possible without their genuine love and care, and their never-ending confidence and support in me.

Finally, I would like to thank Turkish Aerospace Industry (TUSAŞ) for their support of METU-VLA student project. Computing resources provided by the National Center for High Performance Computing of Turkey (UHeM) under Grant numbers 1011202021 and 4009052021 are greatly acknowledged.

TABLE OF CONTENTS

ABSTRACT v

ÖZ vii

ACKNOWLEDGMENTS x

TABLE OF CONTENTS xi

LIST OF TABLES xiii

LIST OF FIGURES xiv

CHAPTERS

1 INTRODUCTION 1

1.1 Literature Survey 2

1.2 Summary of Objectives and Thesis Outline 9

2 METHODOLOGY 11

2.1 Methodology for 2D SD7062 Airfoil Simulations 11

2.1.1 Turbulence Model 14

2.1.2 Grid Refinement Study 16

2.1.3 Time Refinement Study 18

2.2 Methodology for 2D SD7062 with Single-Slotted Flap 21

2.2.1 Parameters of the flap 23

2.2.2 Grid and time refinement studies 25

2.3 Methodology for 3D Very Light Aircraft's Wing 28

2.3.1 Grid and time refinement studies 30

3 RESULTS 35

3.1 SD7062 Airfoil 35

3.1.1 Mean Aerodynamic Coefficients 35
3.1.2 Mean Velocity Field and Laminar Separation Bubble 39
3.1.3 Unsteady Vortex Patterns and Strouhal Number 45
3.1.4 Analysis of Three-Dimensional Flows 57
3.2 SD7062 Airfoil with Single-Slotted Flap 59
3.2.1 Mean aerodynamic coefficients 60
3.2.2 Effect of Gap Size on the Aerodynamic Performance 72
3.3 3D Very Light Aircraft's Wing with Comparing Various Wing Parameter 75
3.3.1 Mean Aerodynamic Coefficients 75
3.3.2 Flow Structures 78
4 CONCLUSION 91
REFERENCES 95

LIST OF TABLES

TABLES

Table 2.1: Configuration and analyses parameters for 2D SD7062 airfoil simulations 12
Table 2.2: Parameters of the computational domains studied during the grid refinement study for SD7062 airfoil 17
Table 2.3: Mean lift and drag coefficients for different time increments at various angles of attack 20
Table 2.4: Analyses parameters for various flight conditions 22
Table 2.5: Position of slotted flap according to flap deflection, gap, and overlap parameters 24
Table 2.6: The percentage difference in lift and drag coefficients for coarse, medium, and fine grids compared to finest grid results 26
Table 2.7: Time refinement study for L1, L2 and L3 at α = 10° 27
Table 2.8: Wing properties and dimensions 30
Table 2.9: Grid refinement studies for α=10° and α=16° 32
Table 2.10: Time refinement study for α=16° and α=20° 32
Table 3.1: Physical dimensions of laminar separation bubble in terms of the chord length of the airfoil for different angles of attack 43
Table 3.2: Comparison of aerodynamic force characteristics obtained in the two- and three-dimensional analysis 58
Table 3.3: Aerodynamic parameters for different configurations 60

LIST OF FIGURES

FIGURES

Figure 2.1: Computational Domain for SD7062 at 10° angle of attack 12
Figure 2.2: Wall $y+$ distribution around SD7062 airfoil with three different heights of the first cell at α=20° 16
Figure 2.3: Aerodynamic coefficients in 600<$t*$<620 interval at α=10° for different grids 17
Figure 2.4: Aerodynamic coefficients in 600<$t*$<620 interval at α=20° for different grids 18
Figure 2.5: The lift and drag coefficients obtained at different angles of attack using time increments of Δt=0.0005s and Δt=0.00025s 20
Figure 2.6: The mean pressure coefficient distribution around SD7062 airfoil using time increments of Δt=0.0005s and Δt=0.00025s at α=21° and α=22° 21
Figure 2.7: Profile of the main airfoil and the slotted flap with different flap deflections 22
Figure 2.8: Computational domains (*a*) general view and closed views for configurations (*b*) C1 (δf=0°), (*c*) T1 (δf=20°), (*d*) L1 (δf=30°), (*e*) L2 (δf=35°), and (*f*) L3 (δf=40°) 23
Figure 2.9: Definitions of kinematic parameters of the flap 24
Figure 2.10: The mean pressure coefficient around the main airfoil and the flap for L-2 configuration with the fine and finest grids at α = 14° 27
Figure 2.11: Illustration of data sampling process 28
Figure 2.12: Top view of (a) the baseline configuration and (b) the rectangular wing, and front view of (c) the baseline configuration and (d) the rectangular wing 30
Figure 2.13: Time-averaged wall $y+$ distribution around the suction surface of the VLA wing for yp=0.003 mm (2.22×10^{-6}c) at α=16° 33
Figure 2.14: Computational domain and boundary conditions (*a*) Isometric view and (*b*) side view 33

Figure 3.1: Mean aerodynamic force and moment coefficients of the unsteady simulations in comparison with the steady-state simulations for SD7062 airfoil at Re=5×10^6 38
Figure 3.2: Length (lb) and height (Hb) definitions of the laminar separation bubble 41
Figure 3.3: Mean pressure and skin friction coefficients and mean velocity streamlines around SD7062 airfoil for α=12° and α=16° 42
Figure 3.4: Mean pressure and skin friction coefficients and mean velocity streamlines around SD7062 airfoil for α=19° and α=20° 42
Figure 3.5: Mean pressure and skin friction coefficients and mean velocity streamlines around SD7062 airfoil for α=24°, 29°, and 30° 43
Figure 3.6: Streamlines of the mean velocity field from α=0° to α=22° 44
Figure 3.7: Streamlines of the mean velocity field from α=22° to α=30° 45
Figure 3.8: Instantaneous and mean vorticity contours for SD7062 at α=0°, 10°, 16°, and 20° 51
Figure 3.9: Instantaneous aerodynamic force coefficients for SD7062 at α=0°, 10°, 16°, and 20° 52
Figure 3.10: Amplitude spectrum of lift coefficient and instantaneous vorticity at α=19.5° 52
Figure 3.11: Instantaneous aerodynamic force coefficients for SD7062 at α=20°-23° 53
Figure 3.12: Instantaneous aerodynamic force coefficients for SD7062 at α=20°-23° 53
Figure 3.13: Instantaneous and mean vorticity contours for SD7062 at α=24°-27° 54
Figure 3.14: Instantaneous aerodynamic force coefficients for SD7062 at α=24°-27° 54

Figure 3.15: The comparison of mean pressure coefficient distributions around SD7062 airfoil between α=29° and 30° 55
Figure 3.16: Instantaneous and mean vorticity contours for SD7062 at α=28° and 29° 55
Figure 3.17: Instantaneous aerodynamic force coefficients for SD7062 α=28° and 29° 55
Figure 3.18: Instantaneous and mean vorticity contours for SD7062 at α=30° 56
Figure 3.19: Instantaneous aerodynamic force coefficients for SD7062 α=30° 56
Figure 3.20: Strouhal number based on amplitude spectrum of the lift coefficient 56
Figure 3.21: Isometric view of the instantaneous vorticity isosurface of three-dimensional URANS solutions of SD7062 at α=10°, 16°, 20°, 24° and 30° 59
Figure 3.22: Mean aerodynamic coefficients of clean airfoil, retracted, and deployed flap conditions for angles of attack from α=-4° to α=20°, (a) Cl - α, (b) Cl - α at around stall region with bars representing the minimum and maximum peaks in the oscillations, (c) Cd - α, (d) $Cmc4$ - α, (e) $ClCd - \alpha$ curves 67
Figure 3.23: Mean pressure coefficient distributions for C-0 and C-1 configurations at α=16° 68
Figure 3.24: Mean pressure coefficient distribution for L-1 configuration at α=12° and L-2 configuration at α=14° 68
Figure 3.25: Mean pressure coefficient distribution on the main airfoil and the flap for L-2 configuration at α=14° and L-3 configuration at α=16° 69
Figure 3.26: Mean velocity streamlines for C-0, C-1, and T-1 configurations at α=12°, 14°, 16°, and 20° 70
Figure 3.27: Mean velocity streamlines for L-1, L-2, and L-3 configurations at α=0°, 10°, 12°, 14°, 16°, and 20° 71
Figure 3.28: Mean pressure coefficient distribution around the main airfoil and the flap at pre- and post-stall angles of attack for L-2 configuration, (a) Main airfoil, (b) Flap 72

Figure 3.29: Flap positions, and mean aerodynamic coefficients at α=0° and α=12° with five different gap sizes for L-3 configuration, (a) flap positions (b) Cl - α, (c) Cd - α, (d) $ClCd$ - α curves 75
Figure 3.30: Time-averaged aerodynamic coefficients versus angle of attack for VW1, VW2, RW1 and SD7062 airfoil at $Re \approx 5 \times 106$, (a) CL vs. α, (b) CD vs. α, (c) $CLCD$ vs. α, and (d) comparison of URANS and 3D Panel code simulations' results 78
Figure 3.31: Comparison of mid-span sectional lift coefficient of VW1, VW2, RW1 and 2D SD7062 airfoil 85
Figure 3.32: (a) Sectional lift coefficients along the spanwise direction, and (b) mean surface streamlines on the suction side of VW1 and RC1 at α=15° 85
Figure 3.33: Sectional lift coefficients, and mean surface streamlines at (a) α=16°, (b) α=17° and (c) α=18° for VW1, VW2 and RC1 86
Figure 3.34: Schematic dimensions of the stall cell 86
Figure 3.35: Variation of (a) dSC, (b) lSC, (c) wSC, and (d) SSC over angle of attack 87
Figure 3.36: Variation of (a) $Clmin$ with respect to lSC, and (b) CL as a function of SSC 88
Figure 3.37: (a) Mean surface streamlines and location of the slices, (b) mean pressure coefficients, (c) vorticity magnitude contours in the wake, (d) iso-surfaces of Q-criterion ($Q = 20$), and (e) In-plane streamlines on yb=0.06, 0.18, 0.31, 0.50 and 0.66 for RW1 and mean velocity streamlines around SD7062 airfoil at α=20° 89

CHAPTER 1

INTRODUCTION

General aviation industry is getting wider every day, and alternative solutions for the design process of general aviation (GA) aircraft are also getting more important. Regarding to this emphasise, a technique that produces highly precise derivatives is wind tunnel testing. Testing in a wind tunnel has the drawbacks of being expensive and time-consuming. Since the results do not always scale up as easily, the fact that the wind tunnel models are scaled down to fit in the tunnel might significantly alter the outcomes. Due to variations in the Reynolds number and other flow properties, air will behave differently while passing over a smaller body than it does a bigger one. Although it will be very expensive, using a skilled wind tunnel expert and a very precise tunnel can minimize these issues. On the other hand, the use of computer simulation has increased significantly during the last few of decades. A branch of fluid mechanics called computational fluid dynamics (CFD) uses numerical methods and a computer to describe the motion of fluids. CFD is merely a tool for analyzing fluid-flow problems. If it is used correctly, it can provide useful information cheaply and quickly. In order to visualize how a gas or liquid travels and how it affects objects as it passes by, computational fluid dynamics uses applied mathematics, physics, and computer software. The Navier-Stokes equations serve as the basis for computational fluid dynamics. These equations explain the relationship between a flowing fluid's velocity, pressure, temperature, and density. For a given set of fluid parameters, such as density, viscosity (a measure of a fluid's resistance to flow), and surface tension, it is concerned with the solution of the velocity field and, consequently, the pressure field.

Many aerodynamic flows are non-stationary even though most are treated as steady flows. In addition to transient regimes, impulsive starts, maneuvering, periodic flows, and flows that are inherently unstable due to the mechanism of vortex shedding from bluff bodies, there are many more types of non-stationary flows. Also, the most of the elements of aircraft performance, such as agility, essentially depends on the control of the unsteady flowfield around an aircraft. Since then, the accurate prediction of the unsteady flowfield becomes crucial to obtain successful aircraft design that overcomes its design missions. In the thesis, the numerical simulations implemented on Very Light Aircraft's components are proposed. Very Light Aircraft (VLA) is defined as a fixed-wing aircraft with one piston engine, two seaters, a maximum takeoff weight of less than 750 kilograms, and designed according to EASA CS-VLA certification. In order to build a very light category aircraft, Turkish Aerospace Industry (TAI) and Middle East Technical University (METU) worked together. The goal of this project is to have METU students work on a real aircraft design process under the guidance of METU professors and with assistance from TAI staff. The METU VLA project was initiated in March 2018 and is now being worked on by academics and students from the departments of industrial design, mechanical engineering, aerospace engineering, and electrical engineering.

In the following part of the introduction section, the literature review of SD7062 airfoil, aerodynamics of high-lift devices, and wing design parameters and stall cells are proposed.

1.1 Literature Survey

During the conceptual design process of VLA, more than thirty airfoils, such as NACA 4415, GOE 387, Rhode St. Genese 32, and SD7062, were compared

considering manufacturing limitations and their aerodynamic performances at cruise condition. SD7062 has the highest lift-curve-slope ($C_{l\alpha}$) and maximum lift coefficient (C_{lmax}) with a reasonable high stall angle of attack. Also, it shows the best drag characteristic and gentle post-stall quality among other airfoils. Therefore, the airfoil for the VLA wing section is selected as Selig-Donovan 7062 (SD7062) airfoil designed by Selig et al. (1989). SD7062 has a maximum thickness ratio of 14% at 0.255c and maximum camber of 3.5% at 0.388c.

SD7062 airfoil is known as one of the commonly used small wind turbine airfoils in literature. Giguère and Selig (1997) performed wind tunnel experiments to provide an airfoil database for small wind turbine blades at low Reynolds numbers. Lyon et al. (1997) state that SD7062 airfoil has good overall performance under clean wind turbine conditions. However, in dirty-blade conditions, it faces high drag and colossal reduction in maximum lift coefficient. Therefore, if SD7062 airfoil is used as a small wind turbine blade, there should be paid attention to keep wind turbine blades clean to avoid the decrease in performance of airfoil. Also, they described this airfoil as an airfoil designed primarily for use on aircraft. Worasinchai et al. (2011) performed a 0.5 m wind tunnel experiment at Durham University at low Reynolds numbers and high angles of attack on wind turbine blade airfoils, including SD7062 airfoil. In this article, SD7062 was mentioned as applicable to small wind turbine blades' airfoil because of soft stall and high lift characteristics. Mamouri et al. (2019) numerically studied the entropy generation of three popular offshore wind turbine airfoils, S822, S825, and SD7062, using two-dimensional unsteady Reynolds-averaged Navier-Stokes (URANS) method at 1×10^6 Reynolds number for four different angles of attack. They have compared these three airfoils and found out that the SD7062 airfoil has the lowest entropy generation and the best performance at angles of attack higher than 10° compared other two popular offshore wind turbine airfoils. Wright and Wood (2004) performed field test and blade element analysis on 2m/600W small wind turbine conducted in their previous studies. SD7062 has been used in the blade of this wind turbine. SD7062 airfoil provides high aerodynamic efficiency at small wind turbine's

working Reynolds numbers and has a relatively high thickness, which is desirable from a structural perspective.

Performance parameters of an aircraft during landing and takeoff rely heavily on the aerodynamics of its high-lift devices. Flaps have been mainly used for high-lift devices in aircraft design for many years. When the flap is deflected downward (deflection angle is positive), it tends to increase both lift and drag forces. The design engineers aim to acquire a more efficient flap design in terms of best lift capability and low drag contribution.

During the conceptual design process of the VLA, four types of flap configurations (plain flap, split flap, fowler flap and slotted flap) were considered. Gudmundsson (2014) states that single element slotted flap is the most used flap type for modern general aviation aircrafts such as, Cirrus SR22 and Cessna TTx. Its simple mechanical operation makes it easy to control and provides a great deal in weight issues. Also, it offers better aerodynamic performance than plain and split flaps considering its higher maximum lift coefficient and less drag penalty. There is no significant difference between the aerodynamic performance of the slotted flap and fowler flap, but it is decided to use the slotted flap due to structural complexity and manufacturing difficulties of fowler flap. At later design stages, the final shape of the slotted flap was decided with adjusting the length, leading edge curvature, camber ratio and flap length by comparing their C_{lmax}, α_{stall}, L/D and $C_{l\alpha}$. Finally, the 0.30 chord length, moderate leading edge curvature and high camber ratio slotted flap with long slot-lip front airfoil configuration was selected. The details of the configuration are discussed in Sec. 2.2.

In the literature, the flow around high-lift devices and resultant aerodynamic forces have extensively studied both experimentally and numerically. Foster et al. (1970) broadly studied the flow around a slotted flap under two-dimensional flow conditions by wind tunnel experiment and theoretical analysis. The authors concluded that the gap size becomes more critical than the overlap size for optimum lift case. Moreover, close to the optimum flap position, the interference

between the wing's wake and the flap boundary layer becomes weaker. Wentz and Seetharam (1974) have been made wind tunnel measurements of the fowler flap configurations constructred with an airfoil of GA(W)-1 at Reynolds number around 2.5×10^6. The optimum flap deflection, flap gap, and overlap were obtained as a function of lift coefficient. The maximum lift coefficient value of 3.8 was achieved for the 30%c model and 40° flap deflection with a 0.027c gap and -0.007c overlap. Wentz (1977) conducted wind tunnel experiment for an airfoil of GA(W)-2 with 0.20c aileron, 0.25c slotted flap, 0.30c fowler flap, and 0.10c slot-lip spoiler at Re=2.2×10^6. For 0.25c slotted flap case, the authors obtained a maximum lift coefficient of 3.35 for both δ_f=35° and δ_f=40°. The highest maximum lift coefficient is observed when the overlap is close to zero and gap size ranges from 0.01c to 0.03c. Wentz and Ostowari (1983) performed a wind tunnel experiment on GA(W)-1 airfoil with 35° deflected 0.30c fowler flap. The results of different slot-gap and cove shapes were compared. Flow separation within the flap cove does not negatively affect the maximum lift coefficient if reattaches. Moreover, more conventional cove design with flow separation and reattachment produced a slightly higher maximum lift coefficient than the cove shape without flow separation. Demel et al. (2016) have studied two-dimensional PIV measurements on NACA 0014 airfoil with 40° deflected fowler flap for different gap and overlap sizes at α=0°, 10°, and 12° at Re=1×10^6 to investigate the effects of fowler flap gap and overlap sizes on the flow field. At α=0°, an increase in the gap size slightly affects the flow field, whereas increasing the overlap size causes the separation of flow in the trailing edge region of the main wing. At α=12°, which is near the stall angle, increasing the gap energizes and improves the flow at the trailing edge region of the main wing. Graham et al. (2017) performed a wind tunnel experiment to investigate the effect of the gurney flap thickness on SD7062 airfoil performance at Re=1.5×10^5. It is found that the lift force increases by increasing the flap height and decreasing the flap thickness. The post-stall flow structure of the stall cell on the NACA0012 wing with a trailing-edge flap is

investigated by Voogt et al. (2022) with wind tunnel experiment at moderate Reynolds numbers between 1×10^5 and 5×10^5.

Günther et al. (2007) reported the investigation of the single-slotted flap of three-element configuration under three-dimensional flow conditions by wind tunnel experiment and numerical simulations based on URANS solutions. They concluded that the lift and drag increase by increasing the flap deflection. However, the maximum lift coefficient and the lift curve slope ($C_{l\alpha}$) are diminished if the flap deflection is increased to very high angles up to δ_f=45°. Ylilammi et al. (2010) have studied SD7062 airfoil with $0.20c$ plain flap both with wind tunnel experiments and numerical simulations at low Reynolds numbers varying from 8.4×10^4 to 4.2×10^5 for α=0° for various flap deflections. It is found that the lift increments compared to retracted flap cases for flap deflections of δ_f=20° and δ_f=30° for Re=4.2×10^5 are about 0.89 and 1.11, respectively. In the experimental and numerical studies of Jansen (2012) on an airfoil with a trailing edge flap model of the Extra EA-400, it is found that the passive flow separation control methods (vortex generators and cylinders) can lead to delay in flow separation and significant lift gain, especially for large flap deflection case. Therefore, these methods can be used to increase the efficiency of the flap. Li and Liu (2017) performed a large-eddy simulation at Reynolds number (Re) of 1×10^6 to simulate the flow over a single-slotted flap to investigate noise generation around the flap slot. Author proposed that large-scale Karman vortex street in the flap wake is the dominant mechanism for the generation of low-frequency tonal noise.

Smith (1975) contributed to understanding the physics of the flow around a multi-element airfoil elaborating five primary effects of gaps: slat effect, circulation effect, dumping effect, off-surface recovery effect, and fresh boundary layer effect. Woodward et al. (1988) appreciably explained the high-lift aerodynamics of scale effect in low-speed flow on the main airfoil and slotted flap combination. The authors introduced a new classification of five types of scale effects and discussed the examples that greatly extended the understanding of high-lift aerodynamics.

During the conceptual design process of the VLA, the wing design variables, such as aspect ratio, taper ratio, dihedral angle, wing sweep angle were selected based on competitor aircrafts' parameters and well-known design approaches (Raymer, 2018). The main design parameters of the VLA aircraft's wing are given in Sec. 2.3. The baseline configuration for the VLA wing design (Figure 2.12a) has a full wing aspect ratio (AR) of 7.26, a taper ratio (λ) of 0.50, a full span (b) of 9.50 m and a dihedral angle (Γ) of 5° (see Figure 2.12a and Figure 2.12c).

The ratio of the tip-chord to the root-chord is called as taper ratio. In the literature, there is no general trend observed for taper ratio impact on the various aerodynamic characteristics, such as the stall angle of attack, the maximum lift coefficient and the lift curve slope. Brewer and Fisher (1951) performed a wind tunnel test to observe the taper ratio effect for straight and swept wings using NACA0012 airfoil for Reynolds number of 1.4×10^6. For the unswept quarter-chord line wings, both tapered and untapered wings produce the same lift coefficients at low angles of attack. Reducing the taper ratio from 1 to 0.5 leads to a slightly greater lift curve slope and a very close maximum lift coefficient, which is accompanied by a little decrease in the stall angle of attack. McVeigh and Kisielowski (1971) examined the effects of airfoil profiles, taper ratio, wing twist, aspect ratio and Reynolds number in the interval between 3×10^6 and 9×10^6 on the stall characteristics by employing the lifting line theory, which shows good agreement with experimental data in the test case. According to their findings, the taper ratio greatly influences stall characteristics. A decrease in taper ratio from 1 to 0.5 mostly results in raising the maximum lift coefficient at high Reynolds numbers. According to Petrilli et al. (2013)'s analysis of URANS simulations of unsweep wings with a NACA4415 airfoil at a Reynolds number of 3×10^6, the rectangular wing reveals a considerably higher maximum lift coefficient and stall angle of attack than the 0.5 tapered wing. To study the impact of the taper ratio, Traub et al. (2015) conducted a wind-tunnel experiment on an AR=5.5 wing with a S8036 airfoil at two low Reynolds numbers of 1×10^5 and 1.5×10^5. The maximum lift coefficient and the stall angle of attack are essentially invariant to the taper

ratio, with the exception of the low taper ratio of 0.2. The lift curve slope gradually decreases at Re=1×10^5 and shows U-type parabolic variation at Re=1.5×10^5 as the taper ratio increases. Ananda et al. (2015) conducted wind tunnel measurement to interpret the effects of taper ratio, aspect ratio and Reynolds numbers variation on the flat plate wing. They found that, as the taper ratio decreases from 1 to 0.5, the maximum lift coefficients for the wings with aspect ratio of 3 and 4 exhibit an increasing trend at around Reynolds number of 1×10^5. There is no apparent trend of the lift curve slope as a function of the taper ratio observed.

The dihedral refers to the angle of the wing with respect to the ground plane as shown in Figure 1c. The studies in the literature focus more on the stability effect of the dihedral than on its aerodynamic influence because the main goal of adding a dihedral to a wing is to maintain roll stability (Feryn and Campbell, 1965; Washburn and Gloss, 1975; Phillips, 2002). In order to study the aerodynamic impact of the dihedral angle, Traub (2000) conducted wind tunnel tests on the delta wing using a range of dihedral and anhedral angles. For the dihedral at low angles of attack, post-stall regimes are detected, but no clear trend can be seen. The severity of the stall enhances as the dihedral rises. Feryn and Campbell (1965) investigated the effect of dihedral on the stability characteristics along with aerodynamic coefficients for supersonic flow conditions at a Reynold number of 3×10^6. The dihedral angle of 3° causes a slightly greater lift curve slope than no dihedral and 3° anhedral wings.

One of the main focuses of this paper is to examine the flowfield around the VLA wing during the pre-stall and post-stall conditions. Petrilli et al. (2013) and Moens (2019) performed numerical simulations on the finite wings to observe post-stall flow dynamics. Initially, the trailing edge separation is observed prior to the stall, and then the stall cell forms stall-onset. According to the studies in the literature, the stall cell occurs for the trailing edge stalled wings at a moderate to high Reynolds number ranges (Dell'Orso and Amitay, 2018; Manolesos et al., 2014; Winkelmann, 1982; Zarutskaya and Arieli, 2005; Voogt, 2019). It was previously

found that SD7062 airfoil experiences a trailing edge stall at Reynolds number of 5×10^6 (Anilir and Kurtulus, 2023a).

According to several studies (Manoloses et al., 2014; Ragni and Ferreira, 2016; Boiko et al., 1996), the stall cell is defined as a three-dimensional "mushroom-shaped" coherent structure made up of two counter-rotating vortices that form on the suction side of the wing during the shallow stall regime. These vortices are connected by a separation line, to which flow is attached above and reversed below. The stall cell formations were mostly investigated experimentally using oil-flow visualization, tuft visualization and PIV on 2D airfoil-testing, but its presence on the finite wings was not abundantly studied both experimentally and numerically.

1.2 Summary of Objectives and Thesis Outline

The major goal of this study numerically explores the unsteady aerodynamics of designed Very Light Aircraft's wing starting from 2D simulations on its airfoil to 3D simulations on the whole wing. The details of objectives of the thesis, informed by the preceding remarks, are summarized below:

- Investigate the aerodynamic performance of SD7062 airfoil at Reynolds number of 5×10^6 for wide range of pre- and post stall regimes. Also, the instantaneous, time-averaged, and steady solutions around the airfoil are compared to reveal the discrepancies which can be helpful for the aircraft designers during the conceptual design phase.
- Examine the influence of the single slotted flap's deflection angle on the aerodynamic coefficients and the flowfield. In addition, the optimum flap position regarding to the maximum lift coefficient is found by adjusting the flap gap.
- Understand the aerodynamic characteristic of VLA's finite wing and various wing design variables. Moreover, the contribution of the well-

defined stall cell characteristics with respect to different finite wing design variables and angles of attack to the sectional and whole wings' lift coefficients are extensively discussed.

The structure of the thesis is as follows. In Chapter 2, the analyzed bodies, numerical methods, grid and time refinement studies are explained. Chapter 3 covers the presentation and discussion of the numerical simulations. Finally, the summary of thesis is proposed in Chapter 4.

CHAPTER 2

METHODOLOGY

In this part of the thesis, the configuration summaries, numerical methods, computational domains, grid and time refinement studies for 2D SD7062 airfoil, 2D SD7062 airfoil with a single-slotted flap, and 3D Very Light Aircraft's finite wing are explained.

2.1 Methodology for 2D SD7062 Airfoil Simulations

The SD7062 airfoil analyzed in this paper has a rounded trailing edge with a radius of 2.235mm (0.0017c) that 1.6mm (0.0012c) of tool radius and 0.635mm (0.0005c) of skin thickness (Figure 2.1). The chord length of the airfoil is c=1.38m which is equal to the mean aerodynamic chord length of the VLA wing designed. Table 2.1 gives information about the configuration parameters. Reynolds number (Re) is defined based on the mean aerodynamic chord and the freestream velocity, U_∞ as given in Eq. (1). The definitions of the two-dimensional lift coefficient (C_l), drag coefficient (C_d) and pressure coefficient (C_p) are shown in Eqs. (2-4), respectively.

$$Re = \frac{\rho_\infty U_\infty c}{\mu_\infty} \qquad 1$$

$$C_l = \frac{F_l}{\frac{1}{2}\rho_\infty U_\infty^2 c} \qquad 2$$

$$C_d = \frac{F_d}{\frac{1}{2}\rho_\infty U_\infty^2 c} \qquad 3$$

$$C_p = \frac{p - p_\infty}{\frac{1}{2}\rho_\infty U_\infty^2} \qquad 4$$

where ρ_∞ is the freestream density, U_∞ is freestream velocity, and μ_∞ refers to the dynamic viscosity of the air, F_l is the lift force per unit span, F_d is the drag force per unit span, p is the static pressure and p_∞ is the static pressure of the freestream.

Table 2.1: Configuration and analyses parameters for 2D SD7062 airfoil simulations

Altitude	Sea-level
Mach Number / Velocity	0.156 / 53.07 m/s
Reynolds Number	~5.000.000
Angles of Attack (α)	From 0° to 10° with 2° increment From 11° to 30° with 1° increment
Turbulence Model	k-ω SST

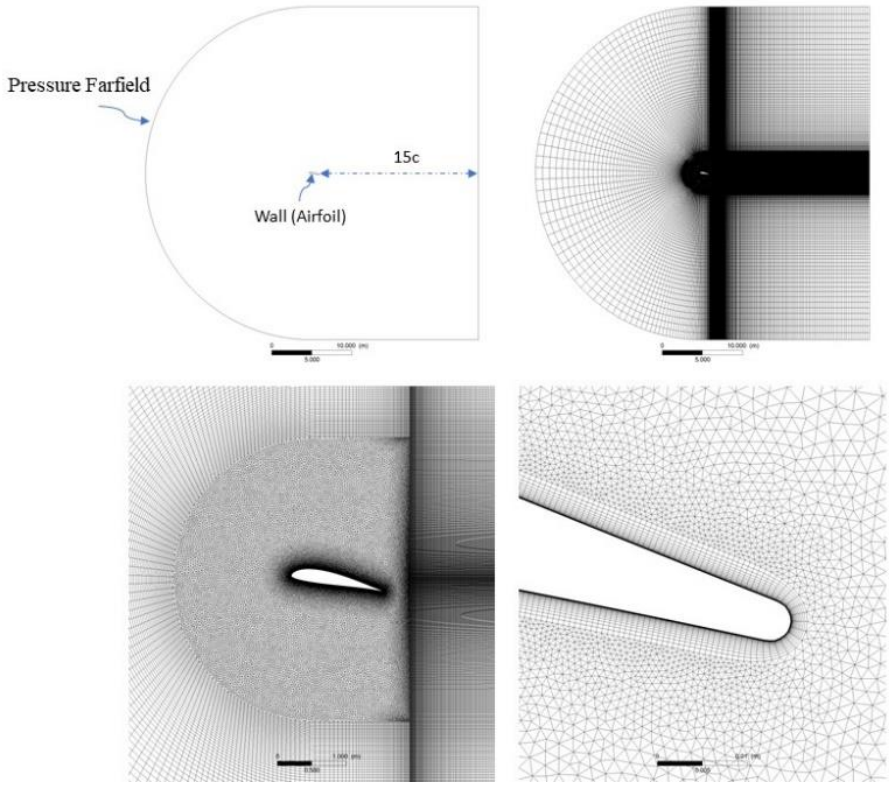


Figure 2.1: Computational Domain for SD7062 at 10° angle of attack

Figure 2.1 shows the computational domain that is used in numerical analyses. This computational domain is composed of an inner and an outer domain. The outer domain's mesh has a structured grid having a C-type shape with 15c distance from the axis of rotation of the airfoil where quarter chord location.

The airfoil is rotated with respect to the quarter chord point for the given angle of attack by keeping the domain of the wake region fixed. This procedure also helps to better visualize the vorticity region at the downstream of the airfoil where the mesh is denser. The inner domain is 1.5c away from the c/4 point of the airfoil. It is composed of structured boundary layer cells in the vicinity of the airfoil and unstructured cells to facilitate the grid generation for each angle of attack. The details of the computational domain and grid selection will be discussed in Sec. 2.2.

Both steady and unsteady RANS simulations are carried out, and the results are compared for different angles of attack. The unsteady results are averaged in the time interval of [20s 40s]. A commercial software (ANSYS Fluent v.17.2), a finite volume solver, is used to obtain current results. The SIMPLE (Semi-Implicit Method for Pressure-Linked Equations) algorithm (Ferziger et al., 2020) is used. All the spatial solutions are selected to be fully implicit second-order accurate. For turbulence modeling, k-ω Shear Stress Transport (SST) model is used. Turbulence model selection will be discussed in Sec. 2.1. in more detail. The ideal-gas assumption is applied with Sutherland law to calculate airflow properties.

Operating pressure and temperature for cruise condition is taken to be 101325 Pa and 288.15 K under standard atmospheric conditions at sea level. The cruise Mach number is taken to be M=0.156, corresponding to 53.07 m/s at sea level. There are two boundary conditions: the wall on the airfoil surface and the pressure far-field at the far boundary of the outer domain (Figure 2.1).

The aerodynamic characteristics of SD7062 airfoil are also obtained by XFLR5 tool, and the results are compared with CFD analysis. XFLR5 program uses the same algorithms as Drela (1989)'s original XFOIL code for two-dimensional

airfoil analysis. Numerical simulations are performed using panel method code for the potential flow theory. It also solves the viscous effect problem with an integral boundary-method. Song (2012) made a validation study of XFOIL code against experimental data. He has found that XFOIL code can reasonably predict the measured lift and drag coefficient of SD7062 airfoil at Re=100,000-400,000 considering its extremely low computational power usage.

2.1.1 Turbulence Model

The two-equation turbulence models, such as k-ε and the k-ω models, are widely used in literature. The k-ε model is best suited for flow away from the wall where free shear flow region with negligible small pressure gradients, whereas the k-ω model is best suited for near the wall flow region, where pressure gradients are very high (Bardina et al., 1997; Menter, 1994; Wilcow, 2006). The k-ω SST model developed by Menter (1994) combines the advantages of k-ε and k-ω models in predicting aerodynamic flows in the wake of the boundary layer and predicting boundary layer especially under strong adverse pressure gradients, respectively. Bardina et al. (1997) carried out validation cases by comparing numerical solutions of four commonly used turbulence models (Spalart Allmaras, k-ω, k-ε, and k-ω SST) with extensively used experimental data for five different near-wall (boundary layer) and free shear flows according to spreading rates and velocity profiles. The k-ω SST model gives preferable good performance for free shear flows and the best performance for complex, separated flows compared with other turbulence models. Hence, in the current study k-ω SST turbulence model was selected as a turbulence model.

The k-ω SST model requires wall y^+ which is a non-dimensional distance perpendicular to the airfoil surface equal to or less than 1. The equations of y^+ given in Eqns. (5)-(8) are used to estimate the required spacing of the first cell (y_p) in order to reach desired y^+ value.

$$y^+ = \frac{u_\tau . y_p . \rho_\infty}{\mu_\infty} \qquad 5$$

$$u_\tau = \sqrt{\frac{\tau_w}{\rho_\infty}} \qquad 6$$

$$\tau_w = \frac{1}{2} . \rho_\infty . C_f . U_\infty^2 \qquad 7$$

$$C_f = \frac{0.0592}{Re^{0.2}} \qquad 8$$

where u_τ refers to friction velocity, τ_w is the wall shear stress, C_f is the skin friction coefficient calculated from Schlichting (1979) with 1/7 power-law approximation.

Figure 2.2 shows the wall y^+distribution around SD7062 airfoil with three different heights of the first cell (y_p) which are 0.01mm (7.41×10^{-6}c) (aiming y^+ of 1.5), 0.005mm (3.71×10^{-6}c) (aiming y^+ of 0.75), and 0.003mm (2.22×10^{-6}c) (aiming $y^+$of 0.5) at α=20°. It can be clearly seen that y^+ values reach their peak value at the leading edge, and a second peak occurs at the trailing edge of the airfoil. When the height of the first cell is equal to 0.005mm, y^+ values are always less than 1 except just the leading edge of the airfoil. For angles of attack greater than 20°, y^+ value at the leading edge can have y^+ values considerably greater than 1, and this may cause a reduction in the accuracy of the analyses. Hence, the first cell spacing of the boundary layer is selected to be 0.003mm (2.22×10^{-6}c) for the rest of the study.

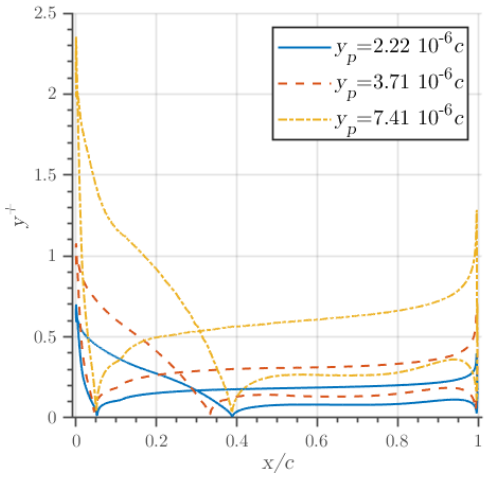


Figure 2.2: Wall y^+ distribution around SD7062 airfoil with three different heights of the first cell at α=20°

2.1.2 Grid Refinement Study

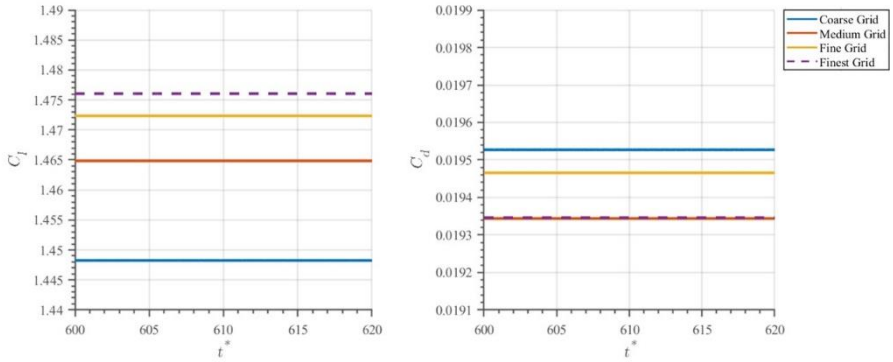
Detailed grid refinement study is carried out for two different angles of attack, which are α=10°-20° with a time increment of Δt=0.001s. Four different grid domains are compared to perform the grid refinement study, namely, the coarse grid, the medium grid, the fine grid, and the finest grid. Detailed information about these four grids is given in Table 2.2. For each angle of attack, the airfoil is rotated around c/4 point of the airfoil. The number of nodes of the coarse grid, medium grid, fine grid, and finest grid around an airfoil are 1000 nodes, 2000 nodes, 3000 nodes, and 4000 nodes, respectively. The far-field is selected as pressure far-field boundary condition with 15c radius away from the airfoil. The numerical simulations are simulated until $t = 40s$ (t^*≡tU_∞/c =1538). The mean results are obtained after 20s of the computations (769<t^*<1538) to not take into account the initial impulsive start effects where the steady or quasi-periodic solutions are reached.

Figure 2.3 and Figure 2.4 show the aerodynamic coefficients versus non-dimensional time graph for different grids investigated at α=10° and 20°. It can be seen that the lift coefficient (C_l) and the drag coefficient (C_d) of the fine and the

finest grids are relatively close for both 10° and 20° angles of attack. The percentage errors between the finest grid and the fine grid for the lift and the drag coefficients are equal to 0.25% and 0.62% for α=10°, respectively. Moreover, the percentage errors between the fine and the finest grid for the lift and the drag coefficients are 0.09% and 1.47% for α=20°, respectively. Consequently, for the rest of the study, the fine grid is used in the analyses.

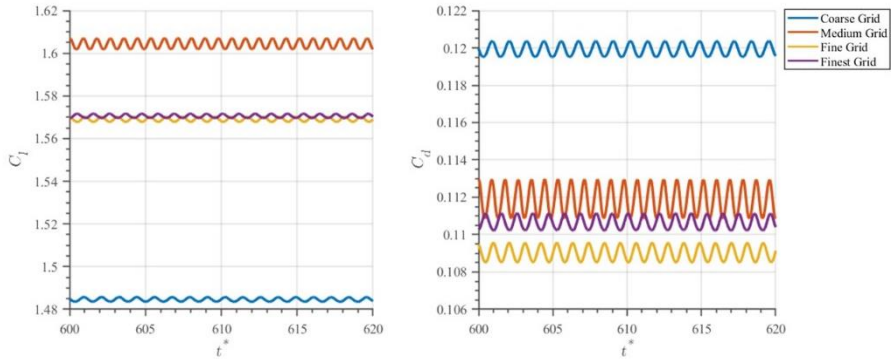
Table 2.2: Parameters of the computational domains studied during the grid refinement study for SD7062 airfoil

	Coarse Grid	**Medium Grid**	**Fine Grid**	**Finest Grid**
Total number of elements	271284	358542	424224	508010
Total number of nodes around the airfoil	1000	2000	3000	4000
Average spacing around the airfoil	$0.020c$	$0.010c$	$0.007c$	$0.005c$
Leading edge first spacing	$0.017c$	$0.009c$	$0.007c$	$0.004c$
Trailing edge first spacing	$0.013c$	$0.007c$	$0.004c$	$0.003c$
First spacing of the boundary layer	$3.71\times10^{-6}c$	$2.22\times10^{-6}c$	$2.22\times10^{-6}c$	$2.22\times10^{-6}c$



a) C_l vs α b) C_d vs α

Figure 2.3: Aerodynamic coefficients in 600<t^*<620 interval at α=10° for different grids



a) C_l vs α b) C_d vs α

Figure 2.4: Aerodynamic coefficients in 600<t^*<620 interval at α=20° for different grids

2.1.3 Time Refinement Study

The time refinement study is conducted with the selected fine grid for several angles of attack to find out the time dependency of the analyses to select the appropriate time step size, which will reveal the onset of the transition for the vortex patterns, and also to save the computational time. The studied time increments are Δt=0.001s, Δt=0.0005s, and Δt=0.00025s at α=10°, 19.5°-23°, and 27°-30°. Table 2.3 shows the results of the time refinement study compared with the mean lift and drag coefficients for different angles of attack. In Table 2.3, the percentage errors are given with respect to the results of Δt=0.00025s. Moreover, the results of Δt=0.0005s and Δt=0.00025s in Table 2.3 are depicted in Figure 2.5 with error bars indicating the maximum and the minimum amplitude values of the aerodynamic coefficients.

It can be clearly seen that below 19.5° angle of attack, the analyses with all the time increments converged to the same aerodynamic coefficients. Therefore, Δt=0.001s will be used in 0°≤α≤19° interval in order to decrease the computational effort. For intervals of 19.5°≤α≤23° and 27°≤α≤30°, Δt=0.00025s time increment is also compared with Δt=0.0005s since the flow is highly unsteady and wake transition can occur (Figure 2.5).

It is found that 19.5°, 20°, and 21° angles of attack are critical angles where the wake-mode transition from steady mode (Mode I "*continuous vortex sheet mode*") to unsteady mode (Mode II "*alternating vortex shedding mode*") (these wake modes are described by Kurtulus (2016)) is observed. Details of wake modes will be discussed in Sec. 3.1.3. The difference in the mean lift coefficient at these angles of attack is very high, even if it is acceptable small for the mean drag coefficient (see Table 2.3 and Table 2.6).

It is observed from Figure 2.5 that analyses with Δt=0.0005s predict a sudden jump in lift coefficient while analyses with Δt=0.00025s provide a smooth increase in lift coefficient from α=20° to α=21°. Figure 2.6 shows the mean pressure distribution around the airfoil for Δt=0.0005s and Δt=0.00025s at α=21°, and 22°. For both angles of attack at two different time step sizes, the mean pressure coefficient (C_p) distribution along the pressure side (lower side) in the vicinity of the trailing edge is very close to each other. At α=21°, C_p on the suction side (upper side) from leading edge to about x=0.4c for Δt=0.0005s is always less than C_p for Δt=0.00025s. This difference becomes more noticeable at the leading edge and leads to a significant discrepancy in lift coefficient (ΔC_l=0.0757, 4.44%) (Figure 2.5a).

At α=22°, the mean pressure distribution, lift, and drag coefficients for both time step sizes are in good agreement (see Table 2.3, Figure 2.5, and Figure 2.6). Therefore, the results of α=19.5°, 20° and 21° are obtained with a time increment of 0.00025s. At 30° angle of attack, another wake pattern mode transition from Mode II "*alternating vortex shedding mode*" to Mode III "*alternating vortex pairs shedding mode*" is identified (see Figure 3.18). The difference between Δt=0.0005s and Δt=0.00025s time intervals in terms of the mean aerodynamic coefficients is high and 0.0005s time increment is not enough to catch the transition wake behavior. Hence, the simulation at α=30° is performed with Δt=0.00025s. Between α=22° and α=29.5°, the results of Δt=0.0005s and Δt=0.00025s considering the mean aerodynamic coefficients are very close.

Consequently, the presented results at these angles of attack are obtained by using the time step size of Δt=0.0005s.

The selected time increments after the time refinement study for each angle of attack are also presented with bold letters in Table 2.3.

Table 2.3: Mean lift and drag coefficients for different time increments at various angles of attack

	Δt=0.001s				Δt=0.0005s				Δt=0.00025s	
α	C_l	% error in C_l	C_d	% error in C_d	C_l	% error in C_l	C_d	% error in C_d	C_l	C_d
10°	**1.4724**	0	**0.0195**	0	1.4724	0	0.0195	0	1.4724	0.0195
19°	**1.6499**	0	**0.0856**	0	1.6499	0	0.0856	0	1.6499	0.0856
19.5°	1.5973	1.53	0.0970	0.21	1.5968	1.37	0.0977	0.53	**1.6221**	**0.0972**
20°	1.5690	5.65	0.109	1.48	1.6257	2.24	0.1101	0.46	**1.6630**	**0.1106**
21°	1.6664	2.16	0.1432	0.71	1.7788	4.44	0.1469	1.84	**1.7031**	**0.1442**
22°	1.6824	5.04	0.1834	2.76	**1.7856**	0.79	**0.1899**	0.71	1.7717	0.1886
23°	1.7915	0.36	0.2424	0.77	**1.8031**	0.28	**0.2410**	0.21	1.7981	0.2405
27°	1.6724	2.13	0.4791	6.15	**1.7283**	1.14	**0.5111**	0.12	1.7087	0.5105
28°	1.7110	1.13	0.5636	2.04	**1.7032**	0.67	**0.5716**	0.64	1.6919	0.5753
29°	1.7649	5.56	0.6613	4.31	**1.6659**	0.36	**0.6249**	1.44	1.6718	0.6340
29.5°	1.7732	6.52	0.7039	5.6	**1.6498**	0.9	**0.6568**	1.47	1.6647	0.6666
30°	1.7803	6.18	0.7485	4.96	1.637	2.37	0.6799	4.66	**1.6768**	**0.7131**

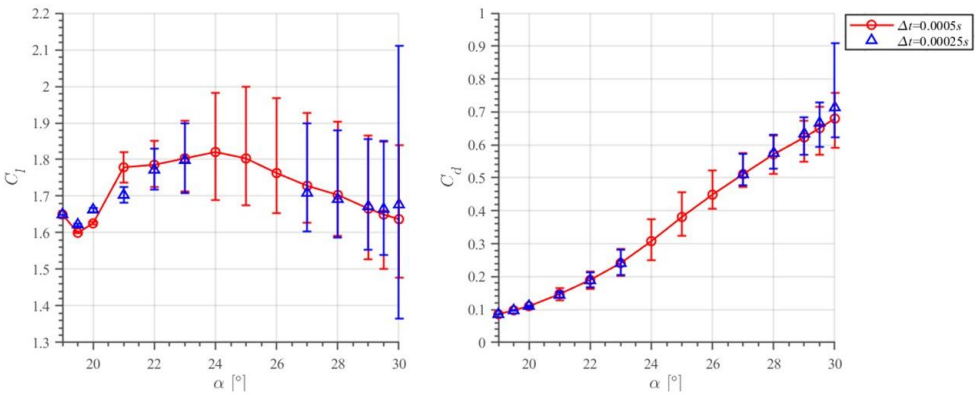
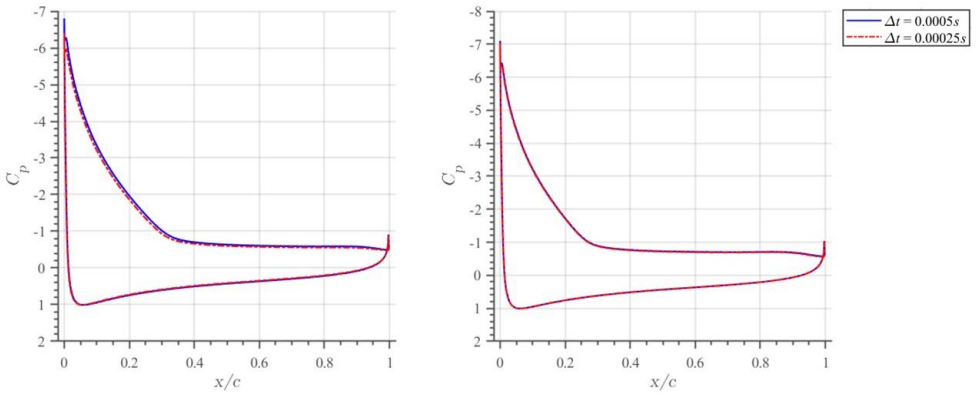


Figure 2.5: The lift and drag coefficients obtained at different angles of attack using time increments of Δt=0.0005s and Δt=0.00025s



a) α=21° b) α=22°

Figure 2.6: The mean pressure coefficient distribution around SD7062 airfoil using time increments of Δt=0.0005s and Δt=0.00025s at α=21° and α=22°

2.2 Methodology for 2D SD7062 with Single-Slotted Flap

In this part, the numerical investigation of SD7062 airfoil with a highly cambered 30-percent-chord single-slotted flap was conducted to find out the aerodynamic performance of the designed flap at different flight regimes and flap deflections. Figure 2.7 shows the geometry of the main airfoil and the slotted flap deployed with different deflection angles varying from δ_f=0° to δ_f=40°. In addition, the hinge point that the slotted flap rotates around at x=0.78c and y=-0.19c is presented. The chord length of the airfoil is c=1.35m which is equal to the mean aerodynamic chord length of the VLA wing designed. The chord length of the flap is equal to c_{flap}=0.376m. The flap's trailing edge is rounded like the clean airfoil configuration. Figure 2.8 shows the computational domain used in computational fluid dynamic simulations. This computational domain is composed of an inner and an outer domain. The inner domain is obtained with structured cells consisting of quadrilateral elements in the boundary layer region of the airfoil. The rest of the domain, also called outer domain, consists of unstructured cells that gradually decrease dense to far-field. The far-field has a distance of 15c to diminish the impact of flow at far-field on a body-close solution.

Table 2.4 presents analyses parameters for cruise, takeoff, and landing conditions. The atmospheric condition for both three conditions is accepted as standard atmosphere so that corresponding operating pressure and temperature for cruise conditions is 101325 Pa and 288.15 K at sea level, and for takeoff and landing conditions 90811.7 Pa and 282.21 K at 3000 ft. Mach number (M) for cruise, takeoff and landing configurations are M=0.156 as 53.07 m/s, M=0.08 as 26.93 m/s and M=0.073 as 24.58 m/s, respectively. Moreover, chord based Reynolds numbers for cruise, takeoff and landing conditions are around 5×10^6, 2.3×10^6 and 2.1×10^6, respectively. The symbols of mean lift, drag, moment, and pressure coefficients and lift-to-drag ratio are $\overline{C_l}$, $\overline{C_d}$, $\overline{C_m}$, $\overline{C_p}$ and $\overline{C_l}/\overline{C_d}$, respectively.

Table 2.4: Analyses parameters for various flight conditions

Configuration	Flow Feature	Mach Number/ Velocity	Reynolds Number
Cruise	Sea-level standard atmosphere	0.156/ 53.07 m/s	~5.000.000
Takeoff	3000 ft standard atmosphere	0.08/ 26.93 m/s	~2.300.000
Landing	3000 ft standard atmosphere	0.073/ 24.58 m/s	~2.100.000

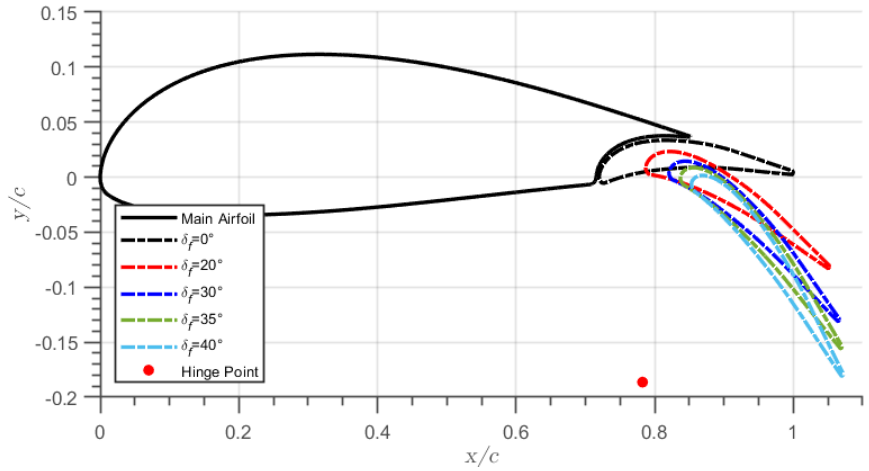


Figure 2.7: Profile of the airfoil - flap configuration

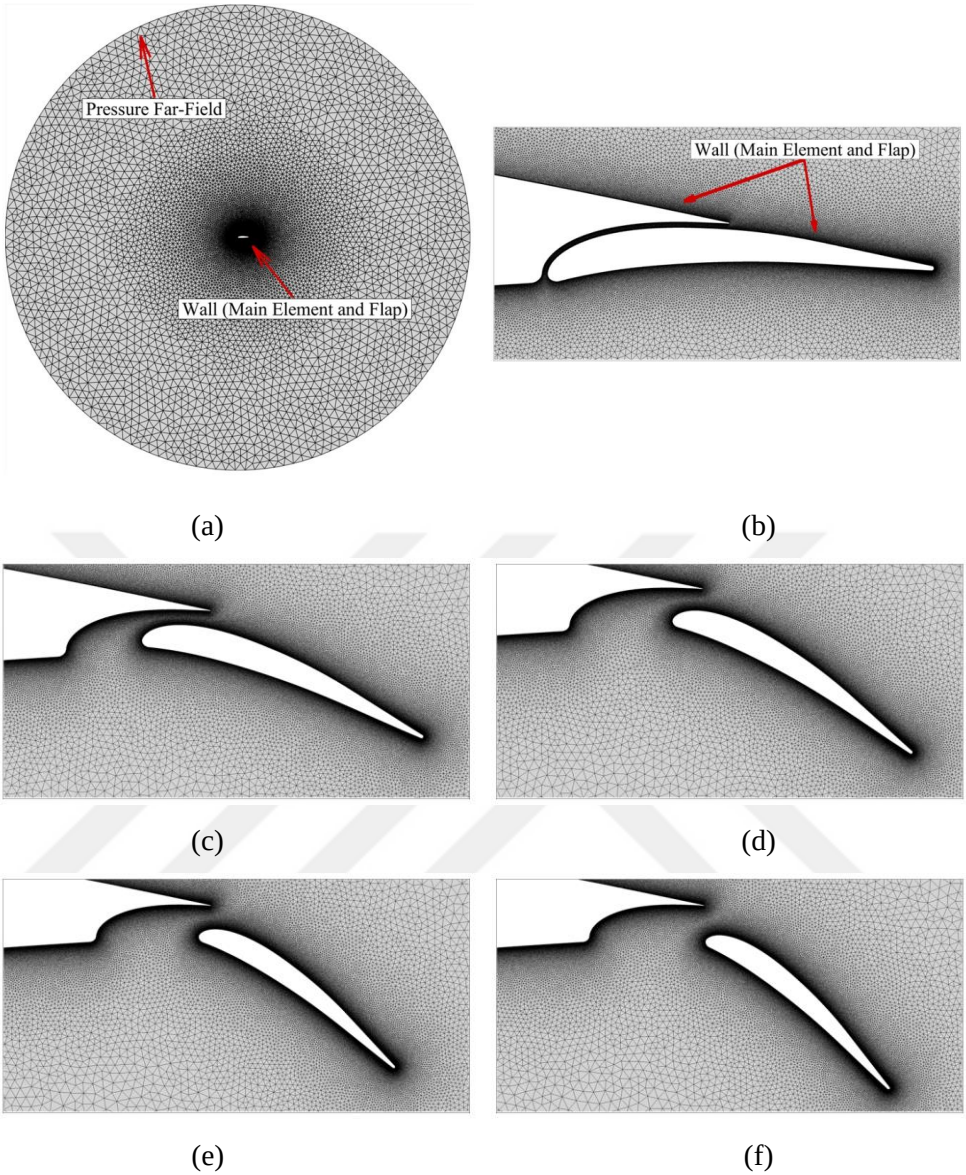


Figure 2.8: Computational domains (*a*) general view and closed views for configurations (*b*) C1 (δ_f=0°), (*c*) T1 (δ_f=20°), (*d*) L1 (δ_f=30°), (*e*) L2 (δ_f=35°), and (*f*) L3 (δ_f=40°)

2.2.1 Parameters of the flap

The important parameters for the aerodynamic performance of the flap are the gap, one the overlap, and the flap deflection are defined in this part of the paper. Figure

2.9 presents the definition of kinematic parameters of the flap, in addition; main airfoil, flap cove, and slot-lip. The flap deflection angle is defined as the angle between the chord line of the retracted and the deployed flap. The overlap refers to the horizontal distance between the slot-lip and the flap's leading edge. When the flap nose is in front of the slot-lip, it is signed as positive. The gap is defined as the minimum distance between the slot-lip and the flap. Table 2.5 summarizes the parameters of flap deflection for different configurations.

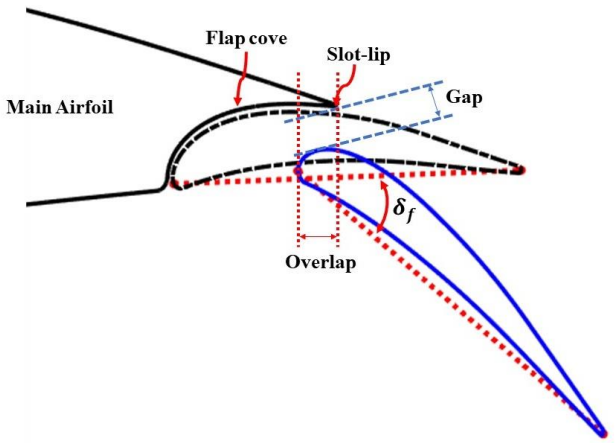


Figure 2.9: Definitions of kinematic parameters of the flap

Table 2.5: Position of slotted flap according to flap deflection, gap, and overlap parameters

Configuration	Short Name	Flap Deflection	Gap	Overlap
Clean	C-0	-	-	-
Cruise	C-1	δ_f=0°	0.004c	0.134c
Takeoff	T-1	δ_f=20°	0.016c	0.061c
Landing I	L-1	δ_f=30°	0.022c	0.029c
Landing II	L-2	δ_f=35°	0.028c	0.012c
Landing III	L-3	δ_f=40°	0.037c	-0.004c

2.2.2 Grid and time refinement

Grid refinement study is carried out for four different angles of attack, α=0°, 4°, 10°, and 16°, and four different grid domains, which are the coarse grid, the medium grid, the fine grid, and the finest grid for clean airfoil configuration. These four grid domains consist of 1003, 2024, 3006, and 4009 nodes on the airfoil surface. The total number of elements are 60448, 110484, 210171, 366607, respectively. The height of the first cell for each grid domain is selected as $0.01mm$ ($7.41\times10^{-6}c$) to have y^+ distribution always less than 1. Figure 2.8 shows the computational domain of the fine grid in the form of O-grid composed of an inner domain and an outer domain. The inner domain is generated with the structured cells in the vicinity of the boundary layer region of the main airfoil and the flap surface. The outer domain has unstructured cells to $15c$ radius with high dense region close to the airfoil, and then, the size of cells gradually increases to far-field. The main airfoil and the flap surface are selected as the wall boundary condition, whereas the far-field is imposed to the pressure far-field boundary condition. Table 2.6 shows percentage differences considering the lift and drag coefficients between the finest grid and the other three grids. The percentage differences between the finest and fine grid do not exceed 1% for any lift and drag results at different angles of attack except at α=16° with almost 1.1% error, which is all in an acceptable range.

To ensure the performance of the fine grid for deflected flaps, the analysis with the finest grid on L-2 configuration at α=14°, which is the stall angle of attack for this configuration, is performed and compared with the fine grid (see Figure 2.10). The lift and drag coefficients of the fine and the finest grid for L-2 configuration at stall angle of attack are 3.302, 3.296, and 0.092, 0.093, respectively. The mean pressure coefficient distribution for the fine and finest grids at α=14° is depicted in Figure 2.10. These two grids show good agreement considering mean lift, drag, and pressure coefficient distributions. Consequently, the rest of the study is performed with the fine grid computational domain.

The time refinement study is carried out for L1, L2 and L3 configurations at α=10° with different time step sizes. The lift and drag coefficient results of the study are shown in Table 2.7. It is observed that the results for L1 with Δt=0.001s and Δt=0.0005s are very close to each other. For L2, the lift and drag coefficients for Δt=0.0005s and Δt=0.00025s are almost identical. For L3, the results for Δt=0.0001s and Δt=0.00005s are satisfactorily close. Hence, the rest of the study for L1, L2 and L3 is performed with Δt=0.001s, Δt=0.0005s and Δt=0.0001s, respectively. Time-averaged data is obtained by taking the mean of at least 10 complete oscillations after periodic conditions are reached or the final steady-state value if the results converge without oscillations in time (see Figure 2.11).

Table 2.6: The percentage difference in lift and drag coefficients for coarse, medium, and fine grids compared to finest grid results

α	**Coarse Grid**		**Medium Grid**		**Fine Grid**	
	$\Delta\overline{C_l}$,%	$\Delta\overline{C_d}$,%	$\Delta\overline{C_l}$,%	$\Delta\overline{C_d}$,%	$\Delta\overline{C_l}$,%	$\Delta\overline{C_d}$,%
0°	2.50	7.33	2.50	7.34	0.01	0.23
4°	2.19	6.49	2.18	6.49	0.50	0.11
10°	2.13	3.84	1.07	0.79	0.39	0.27
16°	4.15	6.68	2.54	2.10	1.12	1.16

Table 2.7: Time refinement study for L1, L2 and L3 at α = 10°

Configuration	Δt=0.002s		Δt=0.001s		Δt=0.0005s	
	$\overline{C_l}$	$\overline{C_d}$	$\overline{C_l}$	$\overline{C_d}$	$\overline{C_l}$	$\overline{C_d}$
L1	3.03	0.05	3.04	0.05	3.04	0.05

Configuration	Δt=0.001s		Δt=0.0005s		Δt=0.00025s	
	$\overline{C_l}$	$\overline{C_d}$	$\overline{C_l}$	$\overline{C_d}$	$\overline{C_l}$	$\overline{C_d}$
L2	3.10	0.07	3.08	0.07	3.07	0.07

Configuration	Δt=0.00025s		Δt=0.0001s		Δt=0.00005s	
	$\overline{C_l}$	$\overline{C_d}$	$\overline{C_l}$	$\overline{C_d}$	$\overline{C_l}$	$\overline{C_d}$
L3	2.48	0.15	2.65	0.16	2.65	0.15

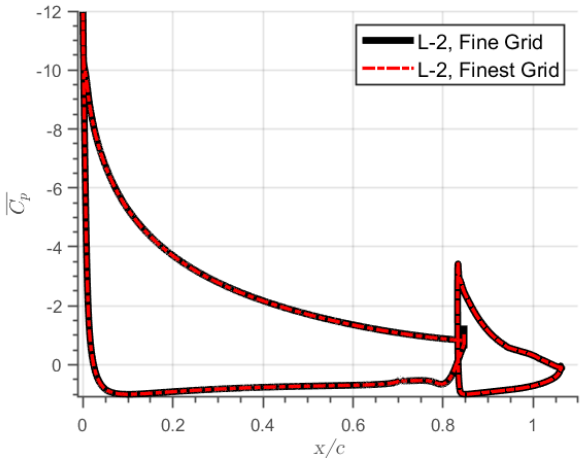


Figure 2.10: The mean pressure coefficient around the main airfoil and the flap for L-2 configuration with the fine and finest grids at α = 14°

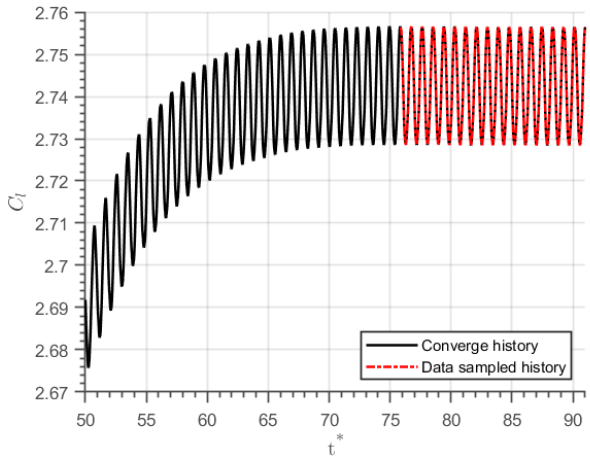


Figure 2.11: Illustration of data sampling process

2.3 Methodology for 3D Very Light Aircraft's Wing

The main objective of the present study is to determine the aerodynamic performance of baseline VLA wing configuration in comparison with a no dihedral wing and a rectangular wing having the same aspect ratio and reference area. These wings are compared in terms of aerodynamic characteristics and flow structures formed on the wing surface as well as at the wake at the pre- and post-stall conditions. The results are also compared with 2D URANS simulations of SD7062.

The abbreviations of VLA wing with Γ=5°, VLA wing with Γ=0° and rectangular wing with Γ=0° are denoted as VW1 (baseline configuration), VW2, and RW1, respectively. The details of these wings are prescribed in Table 2.8 and shown in Figure 2.12. The half-wing model by prescribing the symmetry boundary condition at the root is simulated. Therefore, b denotes semi-span, S refers to semi-reference area and sAR=b^2/S corresponds to a semi-aspect ratio. Taper ratio (λ) is defined as the ratio of tip airfoil chord (c_{tip}) over root airfoil chord (c_{root}), λ=c_{tip}/c_{root}. Mean aerodynamic chord (c) is defined as c=$2/3\, c_{root}(1+\lambda+\lambda^2)(1+\lambda)$ (Raymer, 2018). The wingtip shape of the VLA wing is a smooth rounded tip, whereas the rectangular wing's wingtip is shaped as a cut-off tip. All wings have a

rounded trailing edge with a constant radius of 2.235 mm (0.0017c) at any spanwise section.

The three-dimensional compressible flow over the finite wing is simulated numerically with unsteady Reynolds-averaged Navier-Stokes (URANS) equations using commercial finite volume solver package ANSYS Fluent v17.2 (ANSYS Userguide). The mean aerodynamic chord based Reynolds number defined as $Re_c=\rho_\infty U_\infty c/\mu_\infty$ is set to around 5×10^6 since it is the cruise condition Reynolds number of the VLA. Menter (1994)'s k-ω SST (Shear-Stress Transport) turbulence model is used to comprise the turbulence effect on the numerical simulations.

The definitions of the three-dimensional lift (C_L) and drag coefficients (C_D) are shown in Eqs. (9-10), respectively. The sectional lift and drag forces (F_l and F_d) are obtained by taking integral of pressure and skin friction over the 600 sampled slices on the wing surface (the sectional lift and drag coefficients are denoted as C_l and C_d, respectively). These forces are non-dimensionalized with dynamic pressure times local chord length (c) as shown in Eq. 11 and Eq. 12.

$$C_L = \frac{F_L}{\frac{1}{2}\rho_\infty U_\infty^2 S} \qquad 9$$

$$C_D = \frac{F_D}{\frac{1}{2}\rho_\infty U_\infty^2 S} \qquad 10$$

$$C_l = \frac{F_l}{\frac{1}{2}\rho_\infty U_\infty^2 c} \qquad 11$$

$$C_d = \frac{F_d}{\frac{1}{2}\rho_\infty U_\infty^2 c} \qquad 12$$

where ρ_∞ is the freestream density, U_∞ is freestream velocity, and μ_∞ refers to the dynamic viscosity of the air, F_L is the total lift force, F_D is the total drag force, p is the static pressure and p_∞ is the static pressure of the freestream.

Table 2.8: Wing properties and dimensions

Model	sAR	λ	b [m]	c [m]	S [m^2]	Γ [deg]	Wingtip
VW1	3.63	0.50	4.75	1.35	6.21	5°	Rounded
VW2	3.63	0.50	4.75	1.35	6.21	0°	Rounded
RW1	3.63	1.0	4.75	1.31	6.21	0°	Cut-off

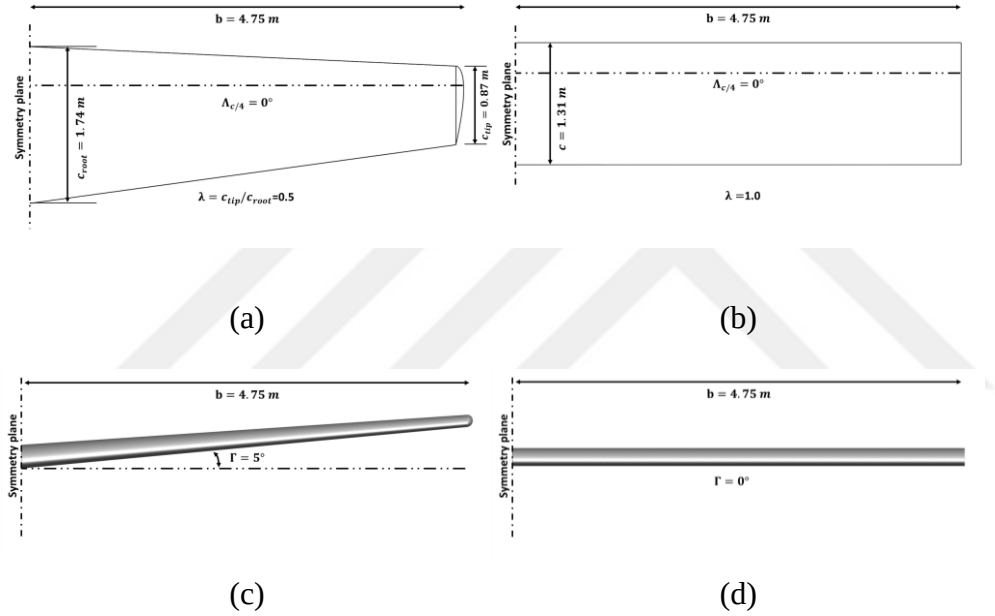


Figure 2.12: Top view of (a) the baseline configuration and (b) the rectangular wing, and front view of (c) the baseline configuration and (d) the rectangular wing

2.3.1 Grid and time refinement studies

Detailed grid refinement study is carried out on the VLA wing for α=10° where the lift-curve slope is not straight anymore and α=16° where the stall angle of attack was obtained for 2D airfoil analysis of SD7062 (Anilir and Kurtulus, 2023a) using a time increment of Δt=0.001s. Three grids, named as coarse, medium, and fine grids, are employed with a refinement ratio of almost 1.5 (see Table 2.9). The grid

refinement study is basically based on the lift and drag coefficients of the VLA wing as a function of the computational cell.

The first grid spacing in the normal-wall direction (y_p) is specified as y_p=0.003 mm (2.22×10^{-6}c). Figure 2.13 shows the time-averaged wall y^+ contours on the suction surface of the VLA wing at α=16°. It is well known that a y^+ value less than 1 is required to fully resolve the boundary layer for high angles of attack; just in case of us, it can be said this goal is reached (maximum y^+ value is 0.71).

The grids are generated in the Pointwise V18.5R1 program. The mesh is composed of different parts. T-Rex (3D anisotropic tetrahedral extrusion) method is used to resolve the boundary layer. It extends unstructured hexahedra cell with a growth rate of 1.15 until it reaches an isotropic height of 1 of the wing surface mesh. The total number of cells at the boundary layer is approximately 14×10^6 for the medium grid, which corresponds to half of the whole computational domain. The space between the boundary layer and the farfield is filled up with axis-aligned regular hexahedra (called Voxel) cells, while the transition between different sized hexahedra cells is achieved using combinations of tetrahedra and pyramid cells. The wake region of the wing is refined to capture flow properties there for each analyzed angle of attack case. The origin is specified at the leading edge of the root airfoil (at y=0 plane). The computational domain covers the largest domain being ($\frac{x}{c}$, $\frac{y}{c}$, $\frac{z}{c}$) ∈ [-25, 25] × [-16, 0] × [-25, 25], where x, y, and z are the streamwise, spanwise and vertical coordinates, respectively. The slice of the domain at y=0.5c can be seen in Figure 2.14. The no-slip boundary condition (wall) is applied to the wing surface, and the outer domain is assigned as the pressure farfield.

Table 2 shows the grid refinement study results on the VLA wing in terms of the mean aerodynamic coefficients for two different angles of attack. It can be observed that the discrepancy for both the lift and drag coefficients are very small. The relative error between the fine grid, and coarse and medium grids are less than 1.5% percent. The current study also aims to capture the wake dynamics precisely by having a refined grid at the wake of the airfoil. So that, the remaining results are

obtained with the medium grid where the wake is also finer compared to coarse grid.

The time refinement study is carried out with the medium grid for time step sizes of Δt=0.002s, Δt=0.001s and Δt=0.0005s at α=16°, and α=20°. The aerodynamic force results of the study are shown in Table 2.10. It is observed that the results for Δt=0.001s and Δt=0.0005s are very close to each other. Hence, the rest of the study is performed with a time step size of Δt=0.001s. Time-averaged data is obtained by taking the mean of 5 complete oscillations after periodic conditions are reached or the final steady-state value if the results converge without oscillations in time.

Table 2.9: Grid refinement studies for α=10° and α=16°

Grid	**Cells**	**α=10°**		**α=16°**	
		C_L	C_D	C_L	C_D
Coarse	19,391,050	1.264	0.088	1.647	0.152
Medium	29,916,806	1.268	0.089	1.643	0.153
Fine	42,358,900	1.268	0.089	1.648	0.155

Table 2.10: Time refinement study for α=16° and α=20°

Time Step Size (s)	**α=16°**		**α=20°**	
	C_L	C_D	C_L	C_D
Δt=0.002	1.644	0.152	1.315	0.239
Δt=0.001	1.646	0.153	1.314	0.238
Δt=0.0005	1.647	0.155	1.314	0.236

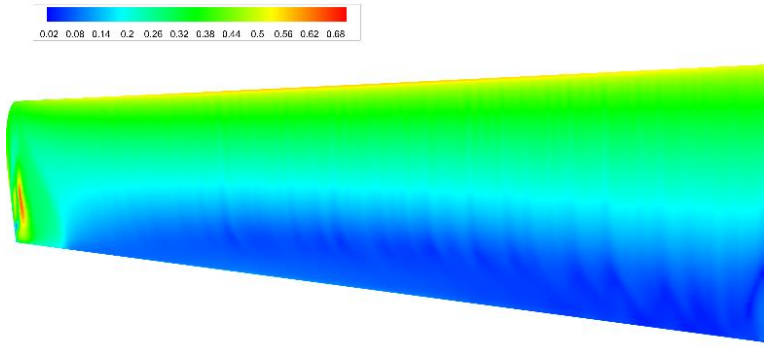
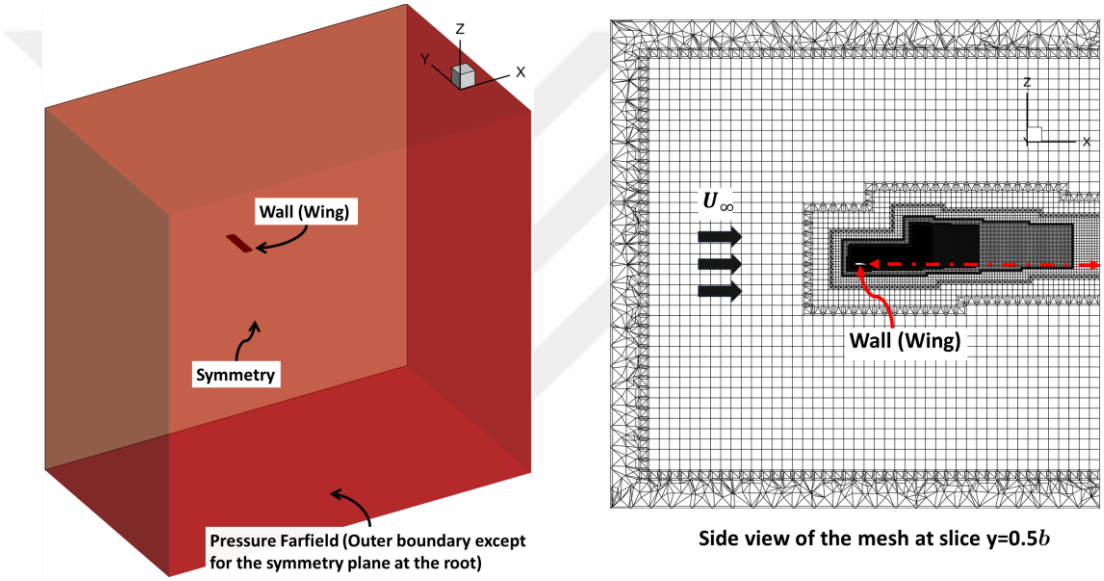


Figure 2.13: Time-averaged wall y^+ distribution around the suction surface of the VLA wing for y_p=0.003 mm (2.22×10^{-6}c) at α=16°



(a) (b)

Figure 2.14: Computational domain and boundary conditions (*a*) Isometric view and (*b*) side view

CHAPTER 3

RESULTS

In this chapter, the numerical simulations for the flow over SD7062 airfoil at cruise condition, SD7062 airfoil with a single-slotted flap at different flight regimes and flap deflections, and Very Light Aircraft's wing by changing the taper ratio, dihedral angle and wing tip shape at cruise condition are presented and discussed.

3.1 SD7062 Airfoil

Numerical results are obtained from α=0° to α=10° with 2° increments and α=11° to α=30° with 1° increments. In 0°≤α≤19°, 22°≤α≤29.5°, and [α=19.5°, 20°, 21°, 30°] intervals, the results are presented for time step sizes of Δt=0.001s, Δt=0.0005s, and Δt=0.00025s, respectively. The results are simulated until t=40s which correspond to a non-dimensional time of t^*=1538. The time-averaged contours and the aerodynamic force coefficients are obtained by averaging the parameters in the interval of 769<t^*<1538 which corresponds to 20s<t<40s. Two-dimensional mean lift coefficient, mean drag coefficient, and the mean pitching moment coefficient at the quarter chord point are denoted as C_l, C_d, and $C_{m_{\frac{c}{4}}}$, respectively. The pitching moment coefficient is non-dimensionalized with $\frac{1}{2}\rho_\infty U_\infty^2 c$ term.

3.1.1 Mean Aerodynamic Coefficients

Figure 3.1 presents the mean aerodynamic coefficients from the steady and unsteady RANS simulations along with XFLR5 tool and a published data of drag coefficient at $Re = 1 \times 10^6$ calculated by Mamouri et al. (2019). The error bars indicate the maximum and minimum amplitude values during the periodic

oscillations. XFLR5 results follow the thin airfoil theory lift curve slope prediction up to α=13°. Also, XFLR5 tool satisfactorily predicts the lift coefficient at 0° angle of attack as 0.4178 where the lift coefficient obtained with CFD is equal to 0.4245. From α=0° to α=7°, the lift coefficient predicted by XFLR5 agrees well with CFD simulations. The XFLR5 results are persistently overestimated after α=7° for lift and drag coefficients. As seen from Figure 3.1, the difference between these two solutions on drag coefficient is always greater than 50%. The lift curve slope of unsteady CFD solution is $C_{l\alpha}$=6.1688 1/rad (1.9646π) in the interval of α=0° and α=6°. Until α=20°, the steady analyses show good agreement with the unsteady analyses. Even at α=20°, the steady analyses predict well the drag (error 0.83%) and the moment coefficients (ΔC_m=0.005) compared to the unsteady simulations. However, a significant discrepancy is observed in the lift coefficient with an error of 4.09%. From α=20° to α=24°, the steady analyses give the drag coefficient and the lift-to-drag ratio close to the unsteady analyses, whereas it fails to predict the lift coefficient and the pitching moment coefficient. As a result, it is found that the solutions are highly time-dependent after α=20°, so the steady-state analyses diverge from the unsteady results.

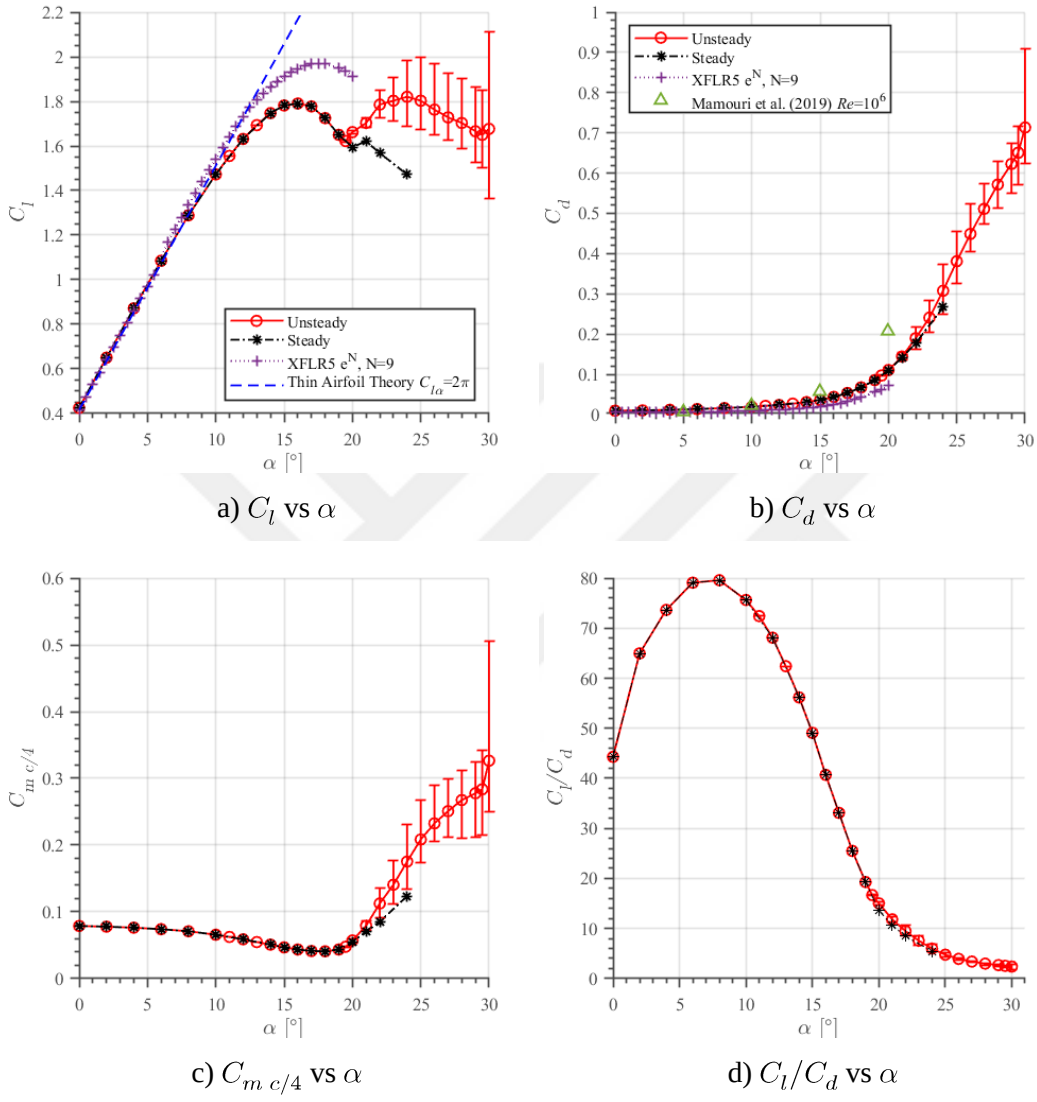
In Figure 3.1(a), the results of unsteady and steady numerical analyses for lift coefficient are depicted. In general, the stall of the airfoil is defined as the sudden and significant reduction in the lift coefficient just after exceeding the stall angle of attack. For SD7062 airfoil, the mean lift coefficient is found to decrease gradually, not suddenly, at high Reynolds number of 5,000,000 at post-stall conditions. This demonstrates the soft stall characteristics of SD7062 at high Reynolds numbers even if it is designed for low Reynolds number flows (Selig et al., 1989). The stall angle of attack of SD7062 airfoil is observed to be at α=16° corresponding to a maximum lift coefficient of C_{lmax}=1.7516. Also, the mean lift coefficient in post-stall for α=17°, and 18° are 1.7773, and 1.7248, respectively. Beyond the stall angle of attack, the mean lift coefficient reduces until α=20°. The angle of attack that the periodic oscillations in the aerodynamic coefficients start is called the

critical angle of attack, which is equal to α=19.5° for SD7062 at $Re \approx 5 \times 10^6$. Above the critical angle of attack, the mean lift coefficient gradually increases up to α=24°. The mean lift coefficient reaches its second peak with a value of 1.8206 at α=24°, and then it starts to decrease with a slope of -1.7178 1/rad (-0.5471π) until α=30°. At α=30°, the mean lift coefficient slightly increases, while a considerable increase in the maximum and minimum amplitude of the lift coefficient is observed. Besides, the maximum and minimum peaks of the instantaneous lift coefficient are found to be 2.1119 and 1.365, respectively.

The mean drag coefficient at various angles of attack is depicted in Figure 3.1(b). It is always in increasing trend for all cases. At low angles of attack, C_d has low values. While close to the stall angle of attack, C_d increases significantly. Above around α=14°, the increase in C_d becomes noticeable. The mean drag coefficient at stall angle of attack is equal to 0.044. When the wake mode shifts from Mode II to Mode III, the maximum instantaneous and mean drag coefficients of 0.9096 and 0.7134 are observed at α=30°, respectively. Figure 3.1(c) shows the pitching moment coefficient with respect to the quarter chord of the airfoil. In aviation, the moment sign is positive if the aircraft makes a nose-up movement. However, it is positive when it tends to decrease the angle of attack in the current study for 2-D analysis. In other words, the nose-down movement of an airfoil is indicated as a positive moment. SD7062 airfoil is unstable at 0° angle of attack as expected. The mean moment coefficient values slightly decrease until α=18°. It reaches its minimum value corresponding to 0.0399 at α=18°. Afterwards, C_m is increased, but the slope of the mean moment coefficient changes while the angle of attack increases.

While the angle of attack increases, the lift-to-drag ratio increases until reaching its maximum value, and then reduces for the remaining cases. The mean lift-to-drag ratio (C_l/C_d) at α=6° and 8° equal to 79.09 and 79.59, respectively (see Figure 3.1(d)). The maximum lift-to-drag ratio is observed at these two angles of attack. SD7062 airfoil provides its most efficient flight while flying at 8° angle of attack.

At stall angle of attack, $\frac{C_l}{C_d}$ is equivalent to 40.69, which is almost half of the maximum lift-to-drag ratio $C_l/C_{d\ max}$.



a) C_l vs α

b) C_d vs α

c) $C_{m\ c/4}$ vs α

d) C_l/C_d vs α

Figure 3.1: Mean aerodynamic force and moment coefficients of the unsteady simulations in comparison with the steady-state simulations for SD7062 airfoil at Re=5×10^6

3.1.2 Mean Velocity Field and Laminar Separation Bubble

The streamlines of the mean velocity field are visualised in Figure 3.3-Figure 3.7 around an SD7062 airfoil for various angles of attack. The airfoil is observed to have a separation bubble on the suction side of the airfoil close to the trailing edge, and this separation bubble grows towards the leading edge as the angle of attack increases. Figure 3.3-Figure 3.5 present the mean pressure and skin friction coefficients and the mean velocity streamlines around the airfoil at different angles of attack (α=12°, 16°, 19°, 20°, 24°, 29°, and 30°) for SD7062 airfoil at $Re \approx 5 \times 10^6$. The mean skin friction values around the SD7062 surface are used to explore the separation and reattachment points of the laminar separation (LSB) bubble. In Figure 3.3-Figure 3.5 and Table 3.1, S and R refer to the position of the separation (S) and reattachment (R) of the laminar separation bubble on the suction side of the airfoil. In addition, l_b and H_b in Table 3.1 denote the surface arc length and height of the laminar separation bubble, respectively. The tiny separation bubble with clockwise rotating vortex around SD7062 trailing edge is observed at α=12° as shown in Figure 3.3 (first row). The angle of attack of 16° is the stall angle (see Figure 3.3, second row), and α=24° is the angle where the second peak of mean lift coefficient is observed [see Figure 3.1(a) and Figure 3.5, first row]. α=19° shown in Figure 3.4 (first row) and α=29° shown in Figure 3.6 (second row) are the transition angles of attack in terms of the wake vortex pattern formations. α=20° and α=30° are the integer angles of attack where mode II and mode III are observed initially, respectively (see Figure 3.11 and Figure 3.18). The mean pressure distribution at the pressure side of the airfoil is almost the same for both six inspected angles of attack from leading edge to about 0.8c. From about 0.8c to the trailing edge of the pressure side of the airfoil, the mean pressure distribution increases in magnitude with an increment of the angle of attack. The effect of the laminar separation bubble on the suction side of the airfoil on the mean pressure distribution can be clearly observed. While the clockwise rotating vortex covers a significant portion of the suction side of the airfoil with increasing angle of attack,

there is a flattening in mean pressure distribution, which is the natural result of a separation bubble (see Figure 3.3-Figure 3.5). Figure 3.3 and Figure 3.4 present the mean pressure distribution in comparison between CFD and XFLR5 results at $Re \approx 5 \times 10^6$ for α=12°, 16°, 19°, and 20°. On the pressure side of the airfoil, the predicted pressure distribution by XFLR5 is found in good agreement with the CFD results for inspected angles of attack. On the suction side of the airfoil, these two results intersect where very close to the separation point of the laminar separation bubble. From this intersection point to the leading edge, XFLR5 consistently overestimates the mean pressure coefficient. These differences clarify the reason for the significant gap in lift coefficient [see Figure 3.1(a)].

O'Meara and Mueller (1987) performed wind tunnel experiments for NACA 663-018 airfoil at low Reynolds numbers and different angles of attack to investigate the laminar separation bubble behaviour at these conditions. The definition of laminar separation bubble parameters provided in their article is also used in our paper, and the results are listed in Table 3.1. Also, length and height definitions of the laminar separation are visualised in Figure 3.2. Boutilier and Yarusevych (2012) focused on separation and transition characteristics of the laminar bubble by performing time-averaged pressure measurement around NACA 0018 airfoil for low Reynolds number and wide range of angle of attack. Below α=12°, the flow is fully attached on the entire airfoil surface. The initial clockwise rotating vortex is observed at α=12°, as shown in Figure 3.3 and Figure 3.6. The length and height of this vortex are quite small and equal to 0.038c and 0.001c, respectively. The clockwise bubble grows in both length and height, but the reattachment point of the bubble remains attached to the trailing edge until α=22°. The reattachment points for $12° \leq \alpha \leq 22°$ interval almost remain constant as R = 0.997c. After α=22°, the clock-wise vortex starts to move towards the leading edge on the basis of both separation and reattachment points, and the reattachment point leaves the trailing edge first at α=23° (see Figure 3.6 and Figure 3.7). The minimum separation and reattachment points are observed for α=30° as S = 0.056c and R = 0.816c. The trend of mean separation locations with the variation of the angle of attack shows a

similar trend with Boutilier and Yarusevych's (2012) study. The laminar bubble's length increases as angle of attack increases until α=29° and reaches its maximum value l_{bmax}=0.804c at this angle. Afterwards, it decreases to value of l_b=0.772c at α=30°. The height of the bubble is highly dependent on the angle of attack. The maximum height (H_{bmax}=0.438c) of it is observed at α=30°. The second vortex formation that is counter-clockwise is also generated just behind the main bubble, which is clearly visible starting from α=13°. The counter-clockwise vortex substitutes the clockwise vortex detached but never touches the suction surface of the airfoil. The clockwise and counter-clockwise vortices gradually grow, and these cause fluctuations in aerodynamic coefficients (see Figure 3.1).

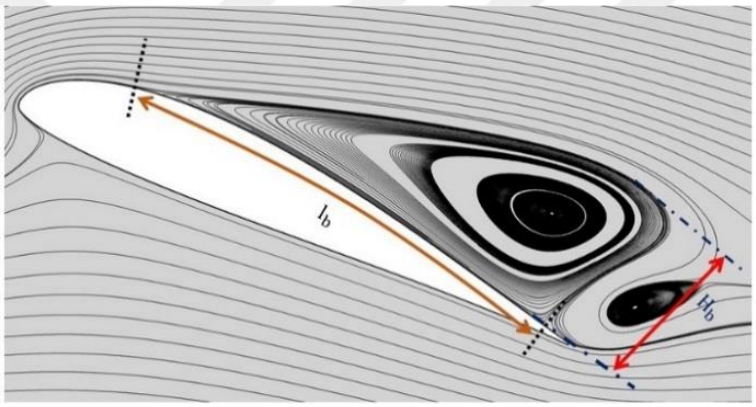
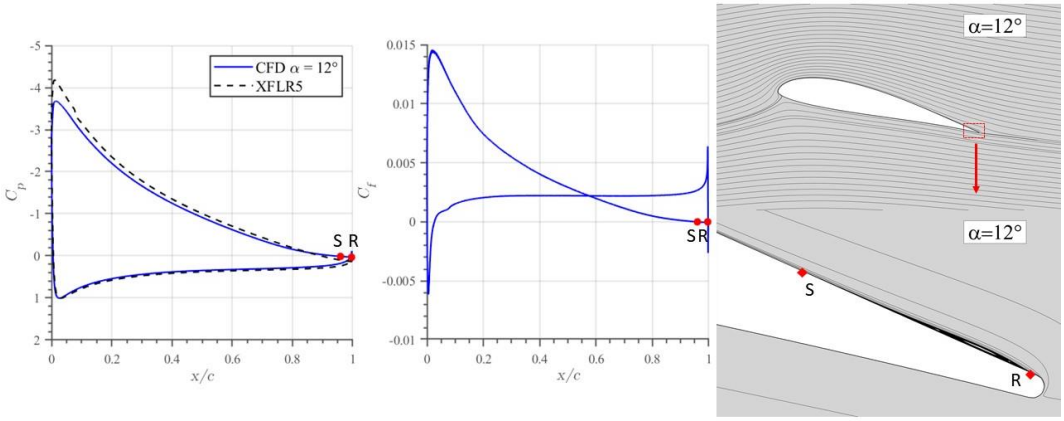


Figure 3.2: Length (l_b) and height (H_b) definitions of the laminar separation bubble



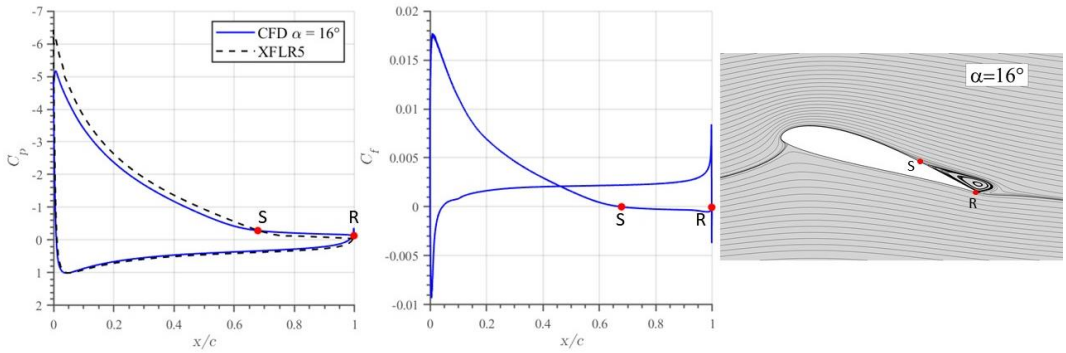


Figure 3.3: Mean pressure and skin friction coefficients and mean velocity streamlines around SD7062 airfoil for α=12° and α=16°

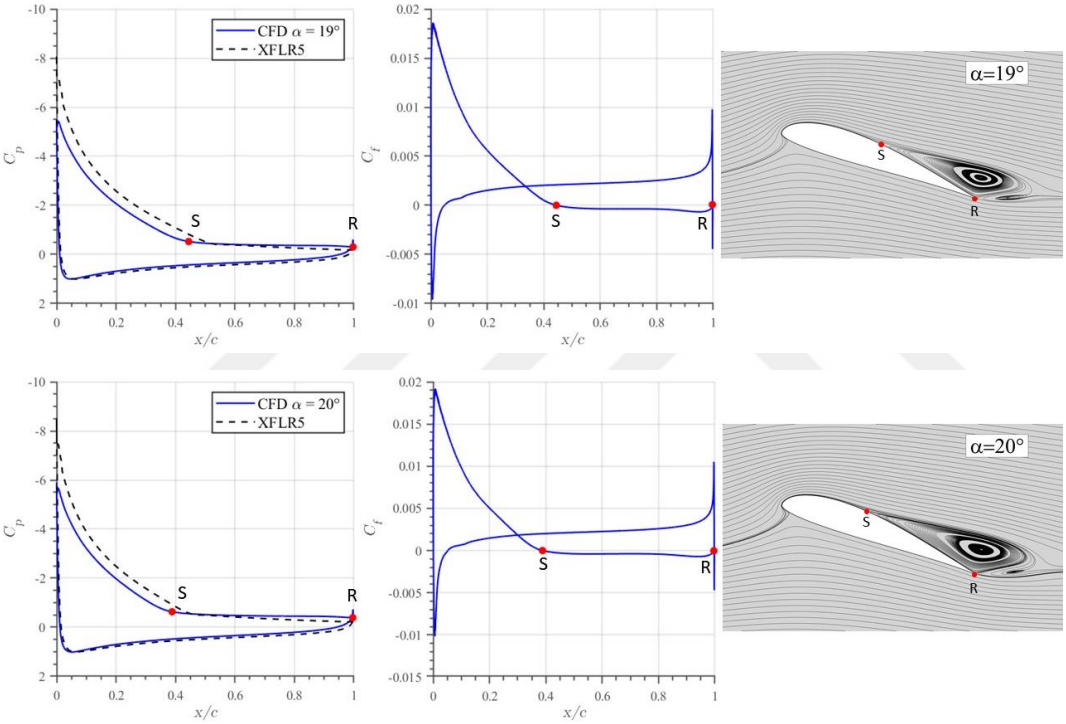
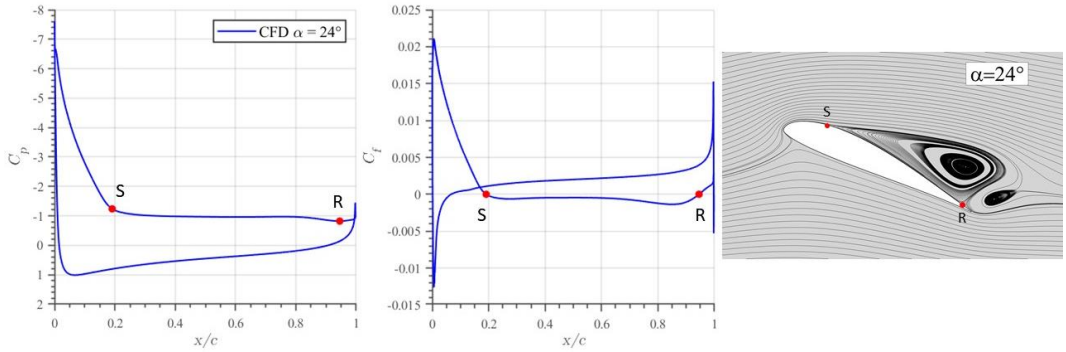


Figure 3.4: Mean pressure and skin friction coefficients and mean velocity streamlines around SD7062 airfoil for α=19° and α=20°



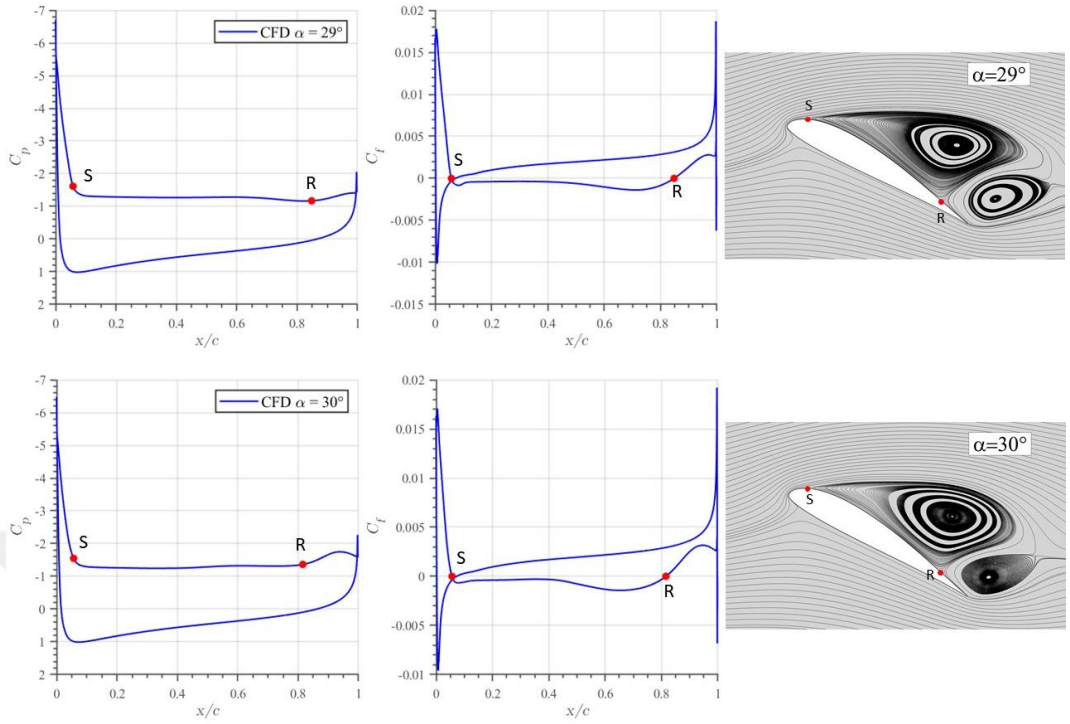


Figure 3.5: Mean pressure and skin friction coefficients and mean velocity streamlines around SD7062 airfoil for α=24°, 29°, and 30°

Table 3.1: Physical dimensions of laminar separation bubble in terms of the chord length of the airfoil for different angles of attack

α	S	R	l_b	H_b
12°	0.960c	0.997c	0.038c	0.001c
16°	0.679c	0.998c	0.326c	0.066c
19°	0.445c	0.997c	0.562c	0.179c
20°	0.389c	0.997c	0.617c	0.186c
22°	0.288c	0.995c	0.715c	0.238c
23°	0.240c	0.981c	0.751c	0.256c
24°	0.163c	0.951c	0.764c	0.282c
28°	0.073c	0.855c	0.794c	0.414c
29°	0.058c	0.849c	0.804c	0.437c
30°	0.056c	0.816c	0.772c	0.439c

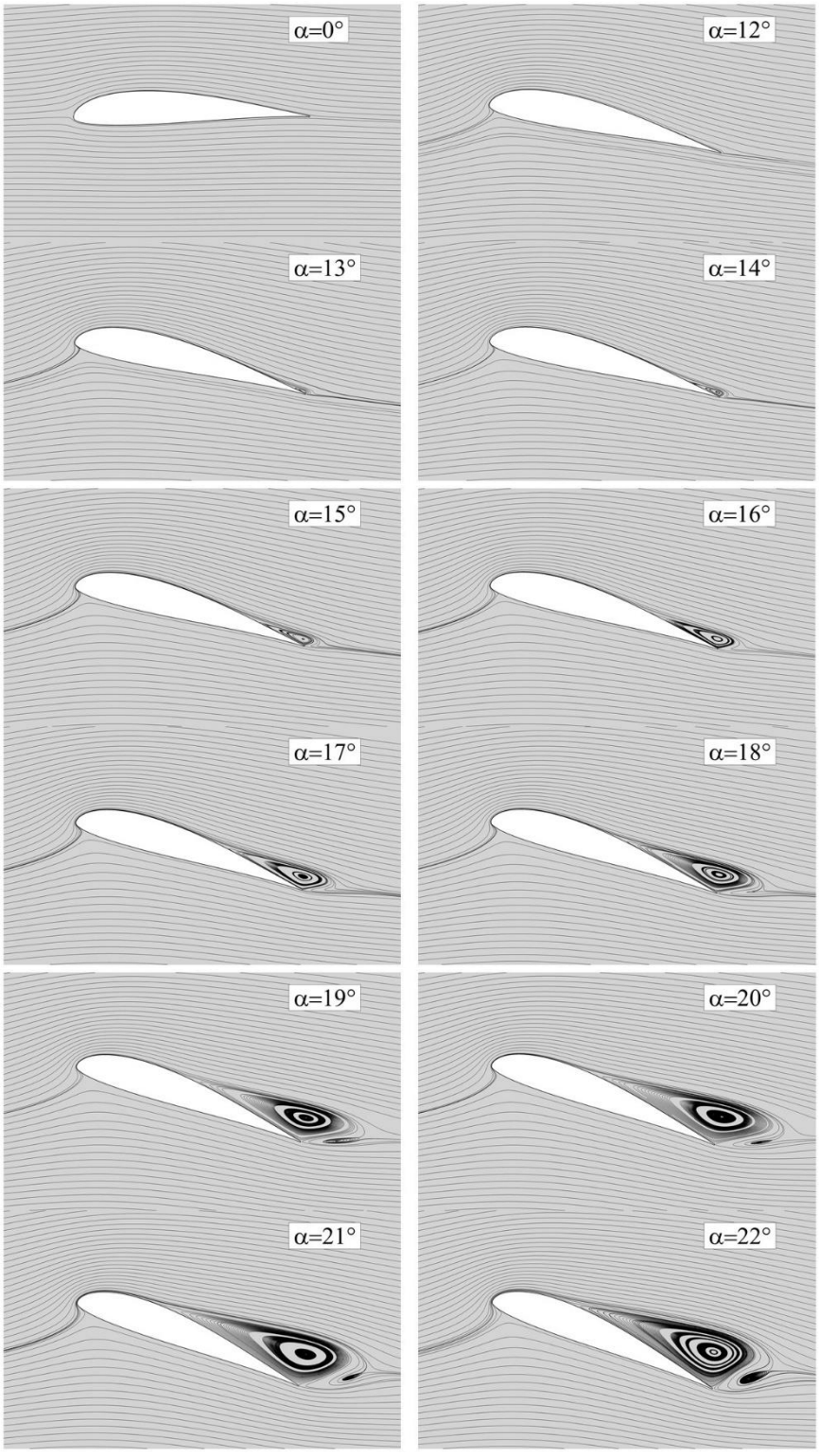


Figure 3.6: Streamlines of the mean velocity field from α=0° to α=22°

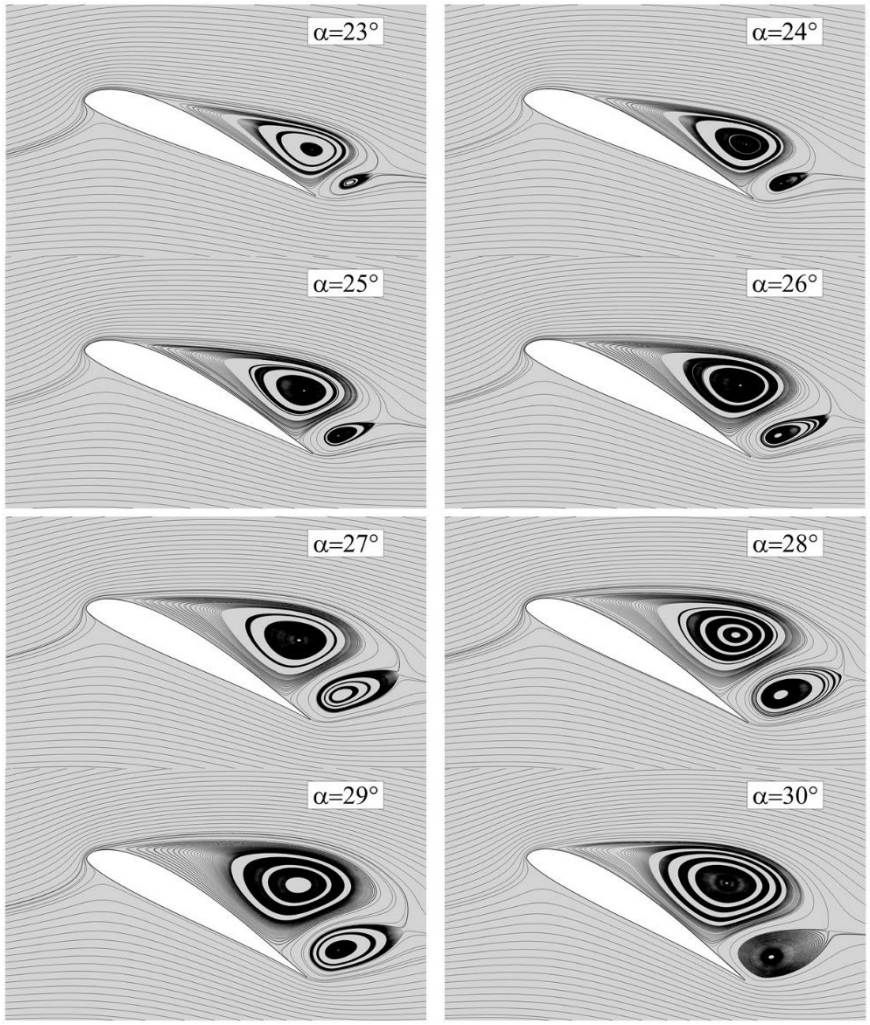


Figure 3.7: Streamlines of the mean velocity field from α=22° to α=30°

3.1.3 Unsteady Vortex Patterns and Strouhal Number

The numerical simulations reveal that, below 19.5° angle of attack, no periodic vortex shedding is formed for SD7062 at $Re \approx 5 \times 10^6$. The first Karman vortex structure is observed at the wake of the airfoil at about α=19.5° for SD7062 airfoil with very low lift coefficient amplitude and high vortex shedding frequency (see Figure 3.10). Kurtulus (2016) performed numerical simulations on NACA 0012 and NACA 0002 airfoils at 1000 Reynolds number in order to investigate the wake pattern of these two airfoils for various angles of attack. Kurtulus (2016) identified vortex pattern into five different modes which are Mode I "*continuous vortex sheet*

mode", Mode II "*alternating vortex shedding mode*", Mode III "*alternating vortex pair shedding mode*", Mode IV "*alternating single vortex with vortex pair shedding mode*", and Mode V "*bluff body vortex shedding mode*" considering the vortex pattern, amplitude spectrum of lift coefficient that was used to obtain Strouhal number, and longitudinal and lateral spacing of the vortices. Williamson and Roshko (1988) grouped the vortex shedding modes as three major modes of the oscillating cylinder in low Reynolds number ranges. These are 2S, 2P, and P+S modes. They also classified different vortex patterns with a combination of these three major modes. The 2S (two single vortices) mode is similar to von Karman vortex shedding. The 2P (two vortex pairs) mode is two unconnected vortex pairs observed above and below the centreline of the wake region, and the final major mode P+S (one vortex pair, and one single vortex) mode is characterised by deviated one vortex pair and one single vortex. Meena et al. (2017) used wake mode classification (steady, 2S, P and 2P) of Williamson and Roshko (1988) for NACA 0000 (flat plate), NACA 0006, NACA 0012, and NACA 0018 airfoil with and without Gurney flap at Re = 1,000. Schnipper et al. (2009) present an experimental study of flapping symmetrical airfoil on the soap film tunnel. They used the classification Williamson and Roshko (1988) by adding some additional vortex shedding modes, such as 2P+2S wake, 4P wake, 8P wake, based on this study. Rossi et al. (2018) performed numerical simulations for NACA 0010 and ellipse with 10% thickness where Reynolds number ranging from 100 to 3000. They used the same classification as Kurtulus (2016) while categorising the vorticity vortex patterns.

In the current study, the vortex pattern classification of Kurtulus (2016) will be used on the basis of instantaneous and mean vorticity wake patterns, Strouhal number based on the lift coefficient amplitude spectrum. A brief summary of these five modes are as follows:

• ***Mode I***: 'continuous vortex sheet mode'. The vortices at the wake are continuous, and the shedding in vortices does not occur. There is no characteristic peak in the frequency spectra of the instantaneous lift coefficient. The aerodynamic

coefficients converge to a steady-state value after a while. Meena et al. (2017) referred to the same mode as a steady regime.

• ***Mode II***: 'alternating vortex shedding mode'. This mode describes periodic von Karman vortex shedding of alternating counter-clockwise rotating vortices and clockwise rotation vortices at the wake. This mode is similar to 2S mode in Williamson and Roshko (1988).

• ***Mode III***: 'alternating vortex pairs shedding mode'. Two discrete vortex pairs where one of them goes up, and above of wake centre-line, the other vortex pair moves in the direction of freestream, which is horizontal direction and parallel to wake centreline. This mode is similar to 2P mode in Williamson and Roshko (1988).

• ***Mode IV***: 'alternating single vortex with vortex pair shedding mode'. This mode is the vortex shedding mode with reverse-rotating vortex pair at the lower and a single counter-clockwise rotating vortex at the upper. This mode is similar to P+S mode in Williamson and Roshko (1988).

• ***Mode V***: 'bluff body vortex shedding mode'. Kurtulus (2016) states that the vortex shedding at very high angle of attack acts like a bluff body.

Mode I "*continuous vortex sheet mode*" is observed in $0° \leq \alpha \leq 19°$ interval (Figure 3.8 and Figure 3.9), Mode II "*alternating vortex shedding mode*" in $19.5° \leq \alpha \leq 29.5°$ interval (Figure 3.10-Figure 3.14 and Figure 3.16-Figure 3.17), and Mode III "*alternating vortex pair shedding mode*" is observed at $\alpha = 30°$ (Figure 3.18 and Figure 3.19) for SD7062 airfoil at around 5,000,000 Reynolds number. An additional run is performed at $\alpha = 19.5°$ to better visualise the critical angle of attack for SD 7062 at this Reynolds number, and the vortex shedding is also depicted at 19.5° as shown in Figure 3.10. Interestingly, similar wake patterns at low and high Reynolds numbers flows are observed. However, mode I is found to last more at higher angles of attack of 19°.

In literature, Strouhal number (St) refers to the dimensionless vortex shedding frequency and describes oscillation flow mechanisms. It is a function of Reynolds number and defined by equation (13) as:

$$St = \frac{f_v c}{U_\infty} \qquad 13$$

where f_v is vortex shedding frequency in Hz, c is the chord length of the airfoil.

Kurtulus (2015, 2016), Meena et al. (2017), Rossi et al. (2018), and Faure et al. (2017) were acquired the vortex shedding frequency based on instantaneous lift coefficient. Clark (2018) and Shi et al. (2011) were acquired the vortex shedding frequency based on the downstream flow velocity. During this study, the vortex shedding frequency is derived from the lift coefficient signal and equals the corresponding frequency of peak amplitude of the amplitude spectrum of lift coefficient calculated using Fast Fourier Transform (FFT) in $769<t^*<1538$ interval. Figure 3.20 presents the variation of Strouhal number with changing the angle of attack.

The unsteady aerodynamic coefficients versus non-dimensional time curves in $1100<t^*<1120$ interval, and instantaneous and mean vorticity distribution of SD7062 airfoil at high Reynolds number around 5,000,000 are presented for different angles of attack in Figure 3.8-Figure 3.14 and Figure 3.16-Figure 3.19. The analyses show that the periodic oscillation in the aerodynamic coefficients is not observed for angles of attack below 19.5°. The two separated trailing edge vortices are generated on the suction side of the airfoil. The upper one indicates a negative vorticity region as a blue-colored contour, and the lower one indicates a positive vorticity region as a red-colored contour which are not shed into the wake of the airfoil for $0°\leq\alpha\leq19°$. At the same angle of attack interval, the lateral distance between these two straight vortices increases with increasing angle of attack. The aerodynamic coefficients converge to steady-state value after a transitory regime is over (see Figure 3.9). The mean and instantaneous vorticity distribution coincide with each other for these steady cases. Also, there is no characteristic frequency in

the amplitude spectrum of the lift coefficient (see Figure 3.20). Hence, the vortex pattern is steady (no variance with time), and Mode I "*continuous vortex sheet mode*" is obtained for $\alpha \leq 19°$ for SD7062 at $Re \approx 5{,}000{,}000$.

The first vortex shedding pattern is found to occur at 19.5° angle of attack for SD7062. This angle of attack is a pretty high angle to observe the first vortex pattern wake behind the airfoil compared to low Reynolds number cases previously investigated by Kurtulus (2016), which are α=8° and α=9° for NACA 0012 and NACA 0002 at Re=1000.

The vortex pattern examined at α=19.5° can be accepted as the flow transition from Mode I to Mode II (Figure 3.10). The instantaneous vortices close to airfoil show feature of Mode I "*continuous vortex sheet mode*", and they are not shed until approximately $1c$ for α=20° and $0.5c$ at the downstream of the airfoil for α=21°. Afterwards the vortices turn out to a natural periodic von Karman vortex shedding Mode II "*alternating vortex shedding mode*" (Figure 3.11).

Figure 3.11-Figure 3.14 and Figure 3.16-Figure 3.17 display the instantaneous and mean vortices, and variation of instantaneous lift and drag coefficients with respect to non-dimensional time for Mode II. Mode II, "*alternating vortex shedding mode*", includes wake pattern at the angle of attack from α=20° to α=29° is characterized by alternating negative clockwise (blue-colored) and positive counter-clockwise (red-colored) vortices in the wake of the airfoil. The shape of clockwise vortices is formed of slug or obovate leaf shapes close to airfoil in the upstream of the wake. In the same region, the shape of counter-clockwise vortices resembles to circular or droplet shape. At the downstream of the wake, both the clockwise and counter-clockwise vortices start to elongate their shape and turn out to be the triangular and elongated circular shapes, respectively. After a while, both vortices fade and converge to Mode I, steady vortex regime. When the mean vorticity contours are examined, Mode II shows a similar wake vortex as Mode I, with the wake's height getting larger as the angle of attack increases. This also causes an abrupt rise in the drag coefficient (see Figure 3.1).

In order to find out the transition angle between Mode I and Mode II, the flowfield at α=19.5° is also analyzed. This transition leads to the oscillation in aerodynamic coefficients. Figure 3.10 shows the amplitude spectrum of lift coefficient and vortex pattern in the wake. The transition between modes can be clearly seen in Figure 3.10 (second column) by inspecting the instantaneous vortex pattern. The steady vorticity regime close to the airfoil surface for α=19.5° is longer and more dominant compared to the case of α=20°. The first and maximum characterized Strouhal number is observed at α=19.5° then at α=20° as 1.289 and 1.283, respectively (see Figure 3.20). It can be generalized that the maximum Strouhal number, so the critical angle for the transition for SD7062 at Re≈5,000,000 should occur in the interval of 19°<α<19.5°. The sudden drop in Strouhal number at α=30° is characterized by mode alteration between Mode II "*alternating vortex shedding mode*" and Mode III "*alternating vortex pairs shedding mode*".

Figure 3.18 and Figure 3.19 show instantaneous and time-averaged vorticity contours, and lift and drag coefficients varying with non-dimensional time for α=30°. The 30° angle of attack is the first angle that Mode III "*alternating vortex pairs shedding mode*" is observed. An additional run is accomplished to find the transition between Mode II and Mode III at α=29.5° if occurs. Nevertheless, Mode II without any transition is observed at the wake of the airfoil. Mode III is a mode distinguished by two vortex pairs located above and below of centerline of the wake behind the airfoil. The upper vortex pair convects upwards while the lower one convects downwards, but it is more aligned to the centerline of the wake than the upper one. The vortex pairs that are observed in this study are a couple of counter-rotating opposite-sign vortices. A dramatic increase in the height of the wake is observed with an increment of the angles of attack from 29° to 30° (Figure 3.16-Figure 3.18). As a result, a significant rise in mean and maximum amplitude of drag and moment coefficients occurs. Below α=30°, the mean, maximum, and minimum amplitude of the lift coefficient spectrum are in decreasing trend.

However, they experience remarkable enhancement because of wake-mode transition at α=30°.

Figure 3.15 gives the comparison of the mean pressure distribution around SD7062 for α=29° and 30°. The gap of the mean pressure coefficient between 0.6c and the trailing edge on the suction side is clearly visible. Moreover, this gap leads to have greater mean lift coefficient for α=30° than α=29°. Also, the sudden drop in Strouhal number (from 0.3714 to 0.2086) with a breaking smooth decreasing trend is observed. Meena et al. (2017) followed a sharp drop in dominant vortex shedding frequency at transition mode between P and 2P for NACA 0000, NACA 0006, NACA 0012, and NACA 0018 with Gurney flap at Re=1000. Kurtulus (2015, 2016) observed a sudden decline in Strouhal number for NACA 0012 for Re=1000 at α=23° which is the first angle of attack that Mode III is investigated. Even if these two studies were performed at low Reynolds number and with Gurney flap in Meena et al. (2017), the effect of transition between Mode II and Mode in Kurtulus (2016), and between P and 2P in Meena et al. (2017) is the same sudden drop in Strouhal number as indicated our study.

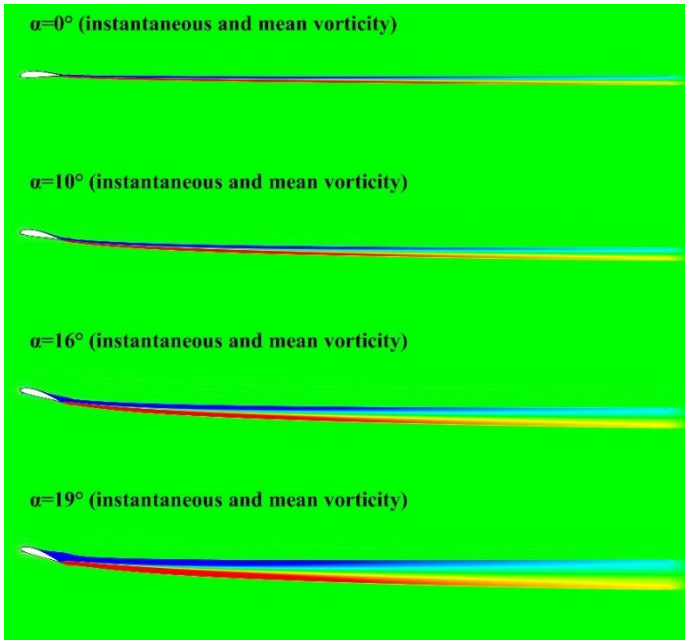
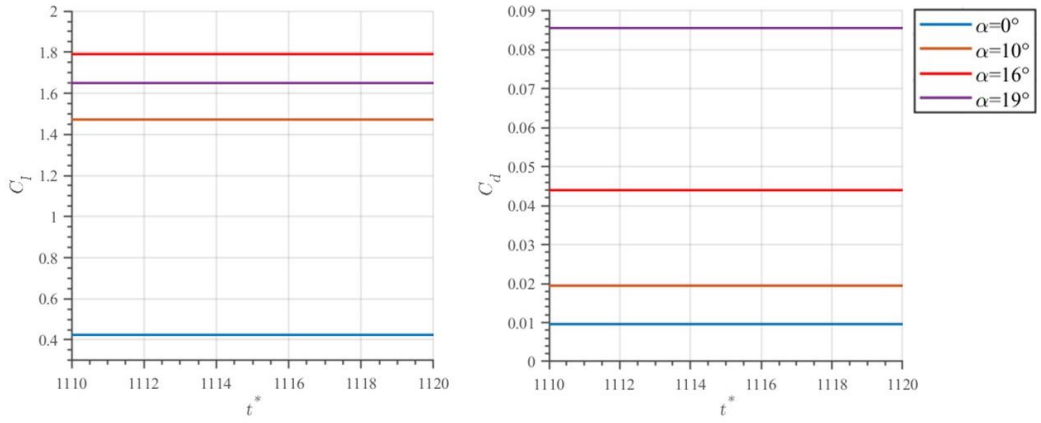
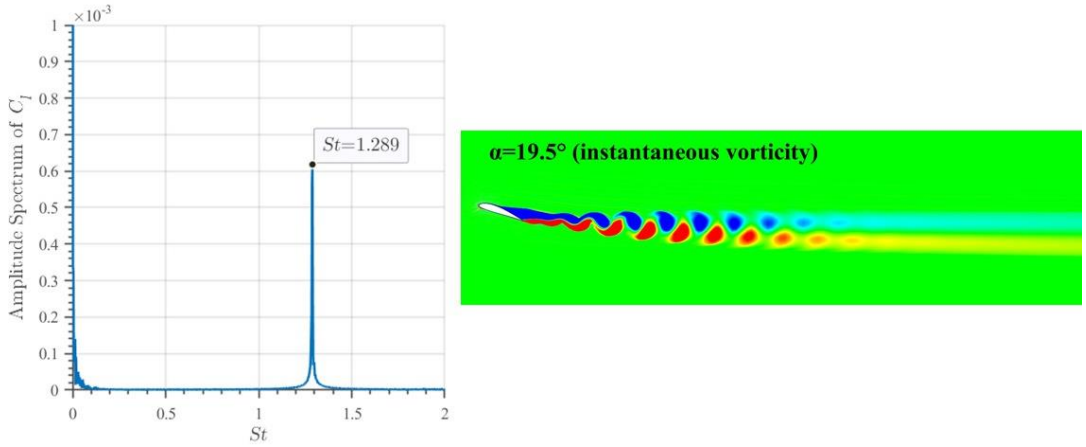


Figure 3.8: Instantaneous and mean vorticity contours for SD7062 at α=0°, 10°, 16°, and 20°



a) C_l vs α b) C_d vs α

Figure 3.9: Instantaneous aerodynamic force coefficients for SD7062 at α=0°, 10°, 16°, and 20°



a) Strouhal number b) Instantaneous Vorticity

Figure 3.10: Amplitude spectrum of lift coefficient and instantaneous vorticity at α=19.5°

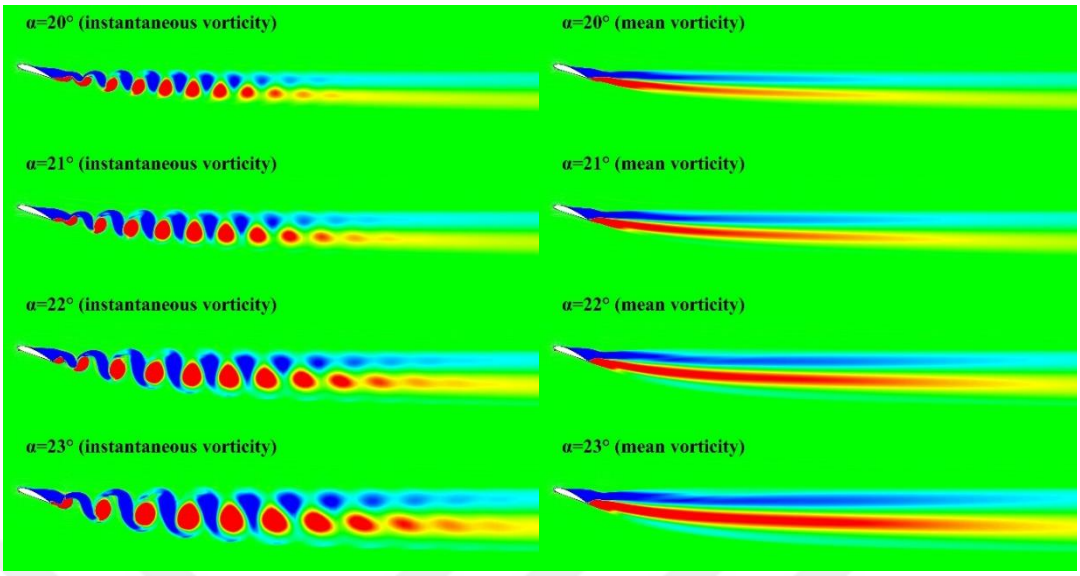
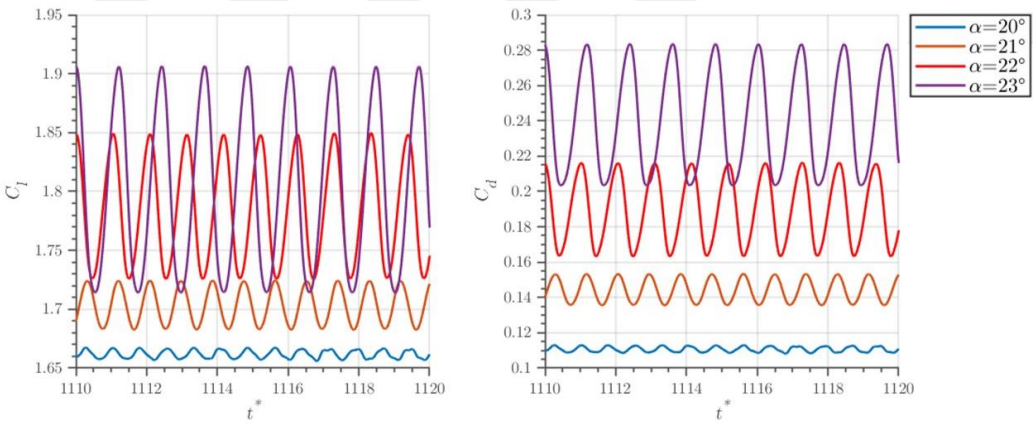


Figure 3.11: Instantaneous aerodynamic force coefficients for SD7062 at α=20°-23°



a) C_l vs α b) C_d vs α

Figure 3.12: Instantaneous aerodynamic force coefficients for SD7062 at α=20°-23°

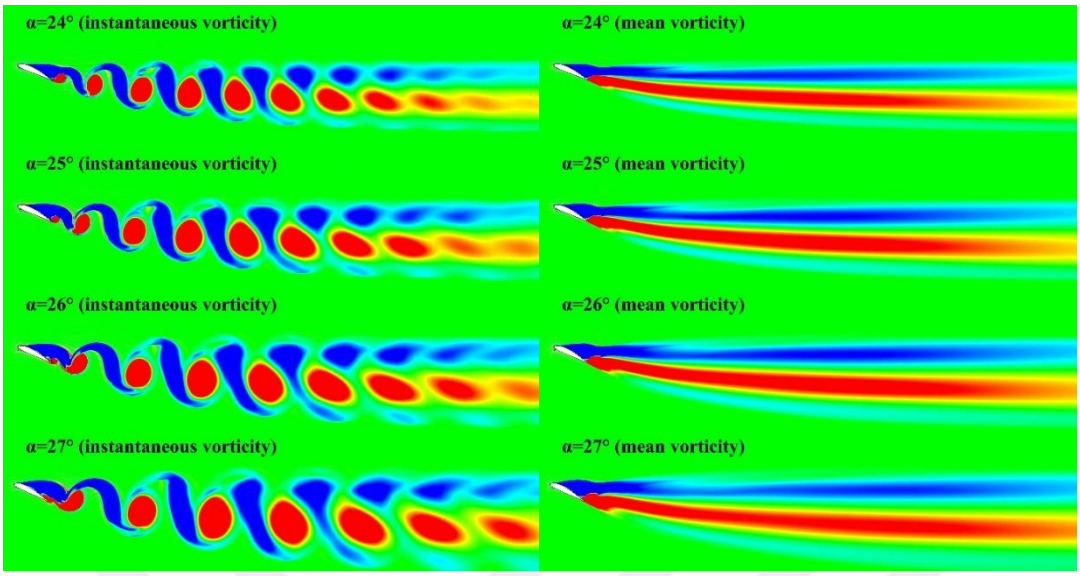
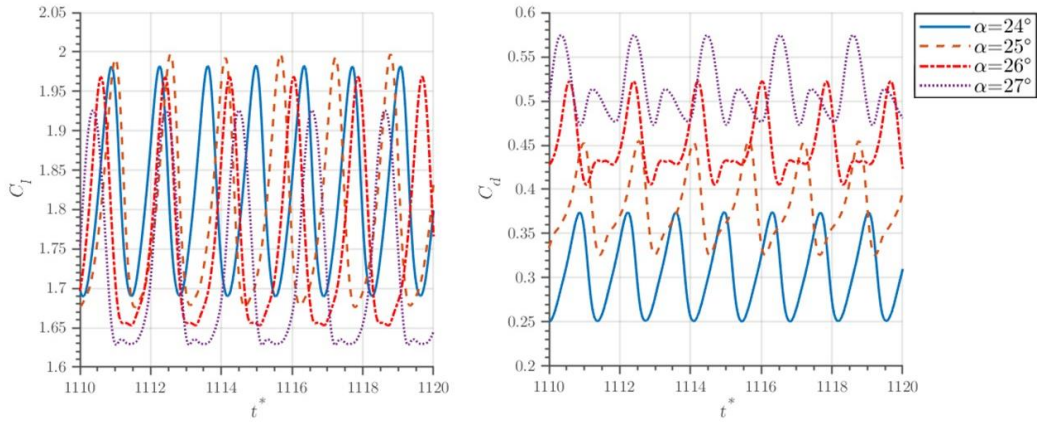


Figure 3.13: Instantaneous and mean vorticity contours for SD7062 at α=24°-27°



a) C_l vs α b) C_d vs α

Figure 3.14: Instantaneous aerodynamic force coefficients for SD7062 at α=24°-27°

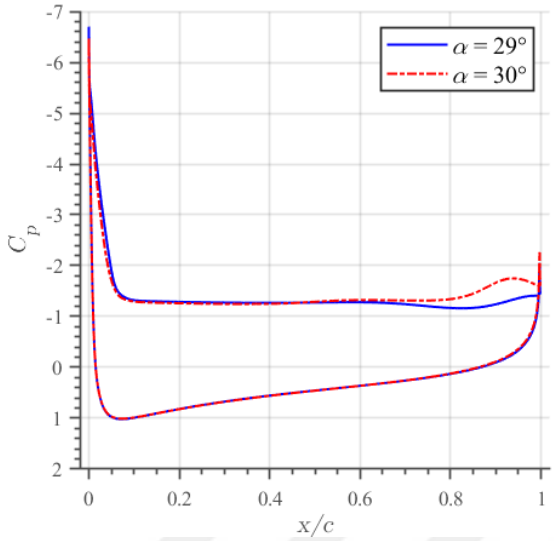


Figure 3.15: The comparison of mean pressure coefficient distributions around SD7062 airfoil between α=29° and 30°

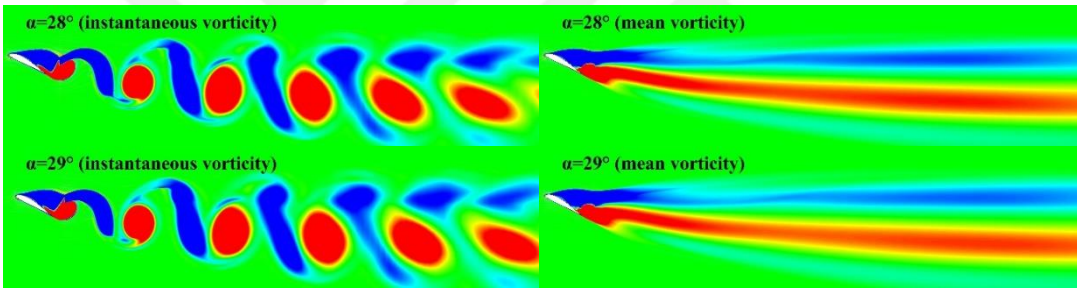
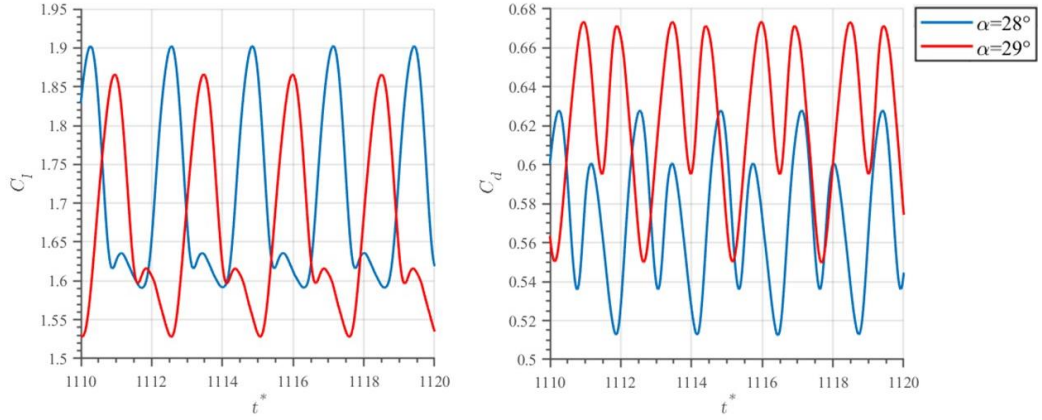


Figure 3.16: Instantaneous and mean vorticity contours for SD7062 at α=28° and 29°



a) C_l vs α b) C_d vs α

Figure 3.17: Instantaneous aerodynamic force coefficients for SD7062 α=28° and 29°

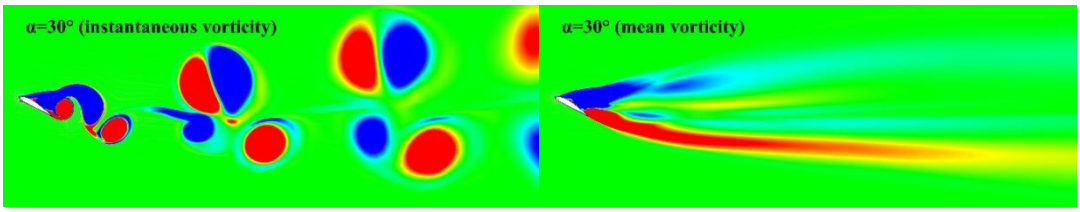
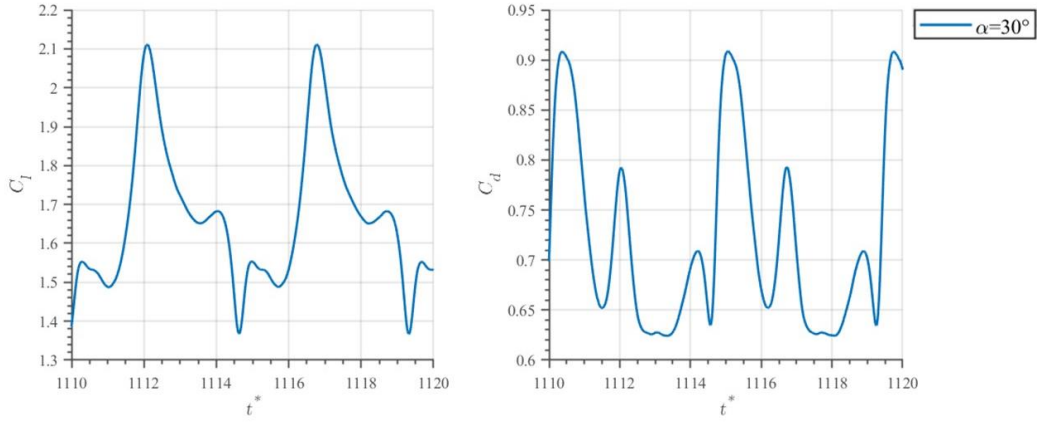


Figure 3.18: Instantaneous and mean vorticity contours for SD7062 at α=30°



a) C_l vs α b) C_d vs α

Figure 3.19: Instantaneous aerodynamic force coefficients for SD7062 α=30°

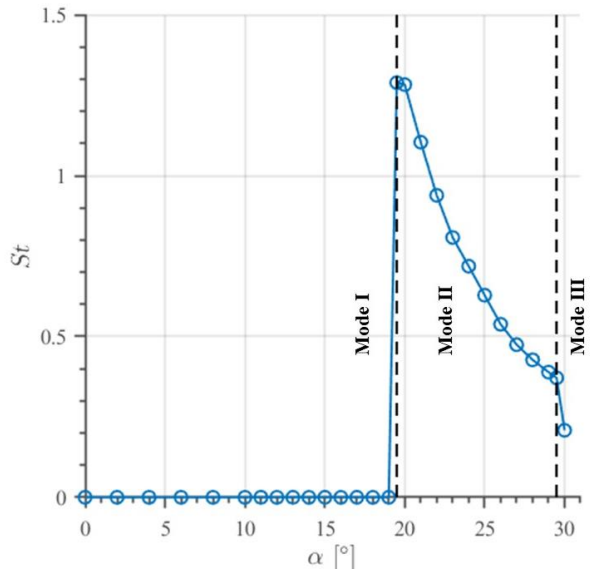


Figure 3.20: Strouhal number based on amplitude spectrum of the lift coefficient

3.1.4 Analysis of Three-Dimensional Flows

Three-dimensional (3-D) spanwise-periodic analyses are conducted with URANS on the selected cases where pre- and post-stall to acquire an understanding of the spanwise effects on the wakes. The angles of attack analyses performed are pre-stall α=10°, stall α=16°, the angle of attack where vortex shedding is observed (α=20°), the second peak in the mean lift coefficient versus angle of attack curve (α=24°), and α=30° that yields Mode III "*alternating vortex pairs shedding mode*" wake regime for two-dimensional flow. Moreover, same time step sizes are specified in three-dimensional analysis with two-dimensional (2-D) analysis. The grid used in the two-dimensional analysis is extruded in a spanwise direction with 0.1c and 50 points. Total number of elements in the computational domain is 20,761,692. Three-dimensional mean lift and drag coefficients are denoted with C_L and C_D, respectively and they are non-dimensionalized with respect to the reference area S=0.1c^2.

Figure 3.21 presents the instantaneous vorticity isosurface of three-dimensional analyses to visualize three-dimensional airfoil wake at five different angles of attack. Table 3.2 shows lift and drag coefficients, and Strouhal number of two- and three-dimensional analysis at five different angles of attack. It is noted that at pre-stall angles of attack, lift and drag coefficients of the 3-D analysis completely match the 2-D data; moreover, vortex pattern of Mode I "*continuous vortex sheet mode*" without any characteristic vortex shedding frequency is observed. The separation and reattachment points of the laminar separation bubble along any spanwise location are consistent and match the 2-D solutions at α=16°. At α=20° and 24°, the vortex patterns are classified as the wake mode of Mode II "*alternating vortex shedding mode*" for both 2-D and 3-D flows. The discrepancy between 2-D and 3-D simulation in lift coefficient and Strouhal number for α=20° are 1.22% and 4.92%, respectively; whereas, 2-D simulation nicely reproduces drag coefficient of 3-D simulation. These two simulations' separation and reattachment points are very close (2-D S=0.389c and 3-D S=0.384c, 2-D

R=0.997c and 3-D R=0.996c). For the case of α=24°, the characteristic vortex shedding frequency, lift and drag coefficients experienced by SD7062 airfoil at $Re \approx 5 \times 10^6$ for 3-D simulations are very similar to the case of 2-D simulations. For the final 3-D simulation at α=30°, its lift and drag coefficients are very similar to 2-D result with an error of 4% and 6.6%, respectively. The mean pressure coefficient distribution of these two simulations perfectly matches on the pressure side and the leading edge of the suction side, while 3-D simulation predicts slightly lower C_p on the suction side from 0.05c to the trailing edge. This case could be classified under the P+S (vortex pair and single vortex) wake regime described by Williamson and Roshko (1988), while Mode III (2P, two vortex pairs) observed for a 2-D flow as aforementioned. Further analyses with a greater downstream length of the computational domain have to be performed to verify this wake regime classification. Hence, three-dimensional analyses demonstrate that two-dimensional analyses can still reproduce many of the flow characteristics even for post-stall and high Reynolds number regimes if appropriately defined. Counsil and Boulama (2013) also state that properly defined two-dimensional simulations are capable of holding lots of three-dimensional flow properties.

Table 3.2: Comparison of aerodynamic force characteristics obtained in the two- and three-dimensional analysis

	2-D			3-D		
α	C_l	C_d	St	C_L	C_D	St
10°	1.47	0.02	–	1.47	0.02	–
16°	1.79	0.04	_	1.79	0.04	–
20°	1.66	0.11	1.28	1.64	0.11	1.22
24°	1.82	0.31	0.72	1.83	0.30	0.74
30°	1.68	0.71	0.21	1.75	0.76	0.21

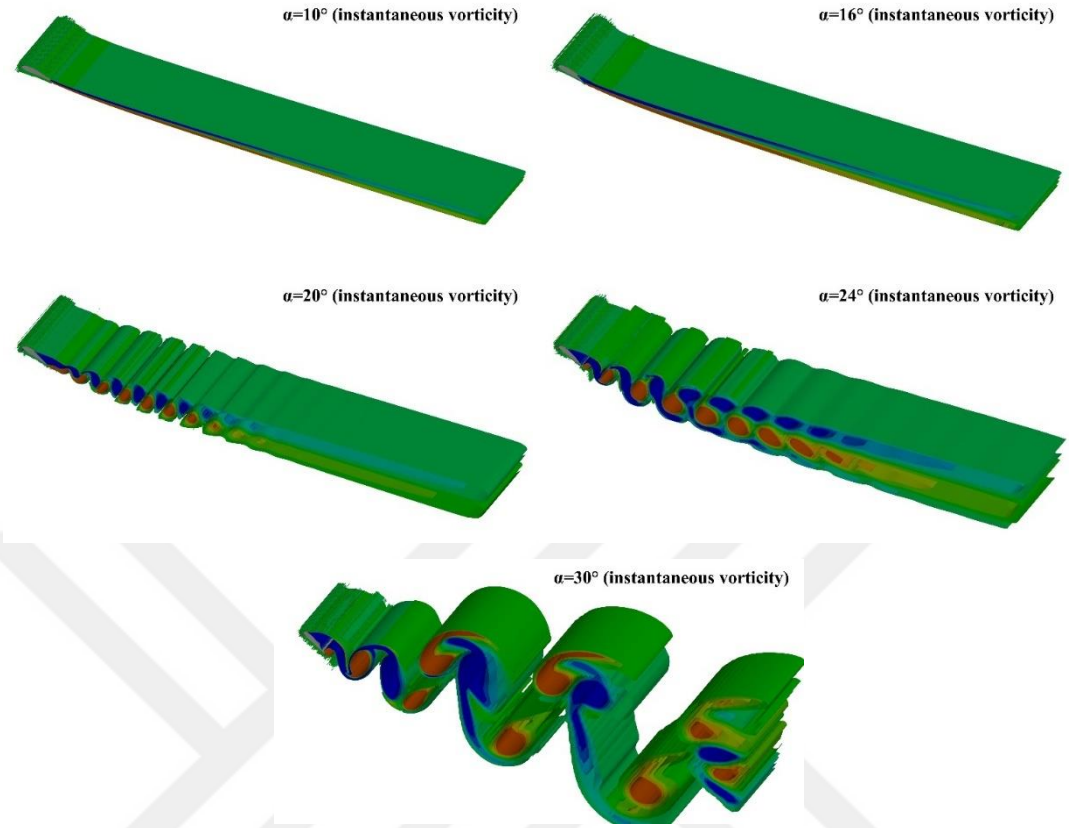


Figure 3.21: Isometric view of the instantaneous vorticity isosurface of three-dimensional URANS solutions of SD7062 at α=10°, 16°, 20°, 24° and 30°

3.2 SD7062 Airfoil with Single-Slotted Flap

The results of two-dimensional numerical simulations for the flow over the SD7062 airfoil with a single-slotted flap implemented to the aft portion of the main airfoil are discussed in this part of the paper. Lift, drag, and moment coefficients were collected from α=-4° to α=20° interval with 2° increment for all configurations (Anilir and Kurtulus, 2023b).

Table 3.3: Aerodynamic parameters for different configurations

Configuration	δ_f	$C_{l\alpha}$	α_{stall}	C_{lmax}	$\left(\overline{C_l/C_d}\right)_{max}$	$\alpha_{\left(\overline{C_l/C_d}\right)_{max}}$
C-0	-	1.99π	16°	1.791	79.592	8°
C-1	0°	2π	16°	1.992	76.956	8°
T-1	20°	1.99π	14°	2.777	74.778	2°
L-1	30°	1.89π	12°	3.147	66.228	2°
L-2	35°	1.84π	14°	3.302	53.442	4°
L-3	40°	1.59π	16°	2.868	18.599	2°

3.2.1 Mean aerodynamic coefficients

Aerodynamic coefficients for C-1, T-1, L-1, L-2, and L-3 configurations are depicted in Figure 3.22 with clean SD7062 airfoil and C-0 configuration, from Anilir and Kurtulus (2023a) and Sec. 3.1 for comparison purposes. The lift curve slope, the stall angle of attack, the maximum lift coefficient, the maximum lift-to-drag ratio, and the angle of attack of maximum lift-to-drag ratio for each configuration are shown in Table 3.3. For C-0, C-1, and T-1 configurations, they exhibit the same curve slope similar to the linearized lift curve slope of 2π as 1.99π, 2π, and 1.99π, respectively. Increment of flap deflection from δ_f=20° to δ_f=40°, the curve slope decreases linearly, while flap deflection increases 1°, the lift curve slope decreases an amount of 0.01π. This linearity is broken for L-3 configuration, and a sudden drop in the lift curve slope from 1.84π to 1.59π is observed for only 5° raise in flap deflection. Lift coefficients of the clean airfoil and no-flap-deflection configurations show good agreement until α=12°. After α=12°, these two results start to deviate from each other. Both of them experience their stall at α=16°, but the maximum lift coefficient of C-0, and C-1 configurations are 1.791 and 1.922, respectively (see Table 3.3, Figure 3.22(a) and Figure 3.22(b)). The mean pressure coefficients at stall angle of attack for C-0 and C-1 configurations are depicted in Figure 3.23. Even if the stagnation points for both configurations are same, the pressure difference on the suction side of the

main airfoil leading to a greater lift coefficient for C-1 configuration is noticeable due to the circulation effect of the flap (Smith, 1975). Above the stall angle, C-0 and C-1 configurations experience a gradual decrease in the lift coefficient. This demonstrates the soft stall characteristic of the SD7062 airfoil mentioned by Worasinchai et al. (2011) and Anilir and Kurtulus (2023a), even with deployed flap case. Reynolds number at takeoff and landing conditions are just lower than the half of the Reynolds number at cruise condition. The lift coefficient of T-1, L-1, L-2, and L-3 configurations at all angles of attack are significantly greater than C-0 and C-1 configurations because of the retracted flap deflection, and an effective camber of the airfoil increases, attributing to lift enhancement (see Figure 3.22(a) and Figure 3.22(b)). The maximum lift coefficient for T-1 configuration is observed at α=14° as 2.777. T-1 configuration provides the highest aerodynamic efficiency compared to the other five configurations up to α=4°, and it reaches maximum lift-to-drag ratio at α=2° as $(\overline{C_l/C_d})_{\max T-1}$=74.778 (Table 3.3 and see Figure 3.22(e)). Between α=4° and α=10°, C-0 configuration provides the highest lift-to-drag ratio among other configurations, and its maximum value is observed $(\overline{C_l/C_d})_{\max C-O}$=79.592 at α=8°. After α=10°, the lift-to-drag ratio of C-0 and C-1 configurations are close, but C-1 has greater $\frac{C_l}{C_d}$ than C-0 configuration.

The higher flap deflection during landing is demanded because of leading to greater lift that permits lower landing velocity, which provides higher drag (see Figure 3.22(c)) and a steep descent angle without increasing airspeed. In L-1 configuration, the parameters of the flap are 30° deflection with 0.022c gap and 0.029c overlap. From L-1 to L-2 configuration, the gap distance and the flap deflection increase from 0.022c to 0.028c and from δ_f=30° to δ_f=35°, whereas the overlap distance reduces from 0.029c to 0.012c, respectively (see Table 2.2). The lift coefficient follows an almost constant slope line for both configurations without noticeable breakdown until about α=12°. Afterwards, the plateau is observed between α=12° and α=14°. The main airfoil flap combination experiences the

highest maximum lift coefficient of 3.147 at the beginning of plateau (α=12°) for L-1 configuration, whereas it is observed at the end of the plateau (α=14°) with 3.302 for L-2 configuration. The sudden drop in the lift coefficient for both configurations after α=14° is observed (see Figure 3.22(b)). The mean pressure coefficient around the main airfoil and the flap for L-1 and L-2 configurations at stall angles of attack of these two configurations are depicted in Figure 3.24. These configurations provide almost the same pressure distribution on the main airfoil, except at the leading edge of L-1 configuration has a noticeably greater pressure coefficient in magnitude. The main difference in the lift coefficient is observed due to the pressure coefficient distribution on the suction side of the flap. The magnitude of the peak pressure at the leading edge for L-2 is 1.5 times of L-1, whereas stagnation point, and pressure side pressure distribution are coincident. The flow separation leads to a plateau in pressure distribution, where the region is covered by separation over the airfoil surface (Wentz and Ostowari, 1983). Thus, there is no boundary layer separation for the configurations at the stall, which is demonstrated by the mean velocity streamlines in Figure 3.27. It can be concluded that the reason of the difference between the lift coefficient of L-1 and L-2 configurations at their stall angle of attack is the pressure distribution at the leading edge and its vicinity.

The negative effect of the flap deflection on drag force is clearly observed in Figure 3.22(c). From C-1 to L-3 configurations, the drag coefficient progressively increases. Moreover, the drag coefficient gradually increases for all deployed flap configurations until α=14°. The percentage differences on drag coefficient between L-2 and L-1 configurations are always greater than 10%; in addition, these differences become greater than 20% below α=12°. L-1 configuration provides a greater lift-to-drag ratio than L-2 configuration, even for post-stall angles of attack. While L-1 reaches its maximum lift-to-drag ratio $\left(\overline{C_l/C_d}\right)_{\max L-1}$=66.228 at α=2°, L-2 reaches its maximum lift-to-drag ratio $\left(\overline{C_l/C_d}\right)_{\max L-2}$=53.442 at α=4°. On the other hand, $\frac{\overline{C_l}}{\overline{C_d}}$ values of T-1 configuration for each angle of attack are greater than

L-1, L-2, and L-3 configurations. This demonstrates that higher flap deflection causes a greater drag penalty than the lift force increment.

Figure 3.22(d) presents the time-averaged pitching moment coefficient with respect to the quarter chord location. The sign of the moment coefficient is positive if the airfoil makes a nose-up motion. The moment coefficients for all configurations are negative in the range of angles of attack considered in this paper. Also, they show an unstable characteristic at 0° angle of attack due to a negative pitching moment. The magnitude of the mean moment coefficient increases with increasing flap deflection except for L-3 configuration, similar to other aerodynamic coefficient results. The aerodynamic coefficients of L-3 configuration are closely examined due to its exceptional outcomes, among other configurations. When the flap deflection is increased to δ_f=40° at landing condition with a gap of $0.036c$, which refers to L-3, detrimental effects on aerodynamic performance are observed, including a significant rise in drag, decrease in lift curve slope and lift coefficient for each angle of attack compared to δ_f=35° flap deflection with $0.027c$ gap configuration of L-2. Huge separation bubble in the wake of flap and vortex shedding formation for each angle of attack that causes wild vibration and loss of control of the flap during the flight are observed in Figure 3.27, third column.

The lift coefficient of L-3 configuration at α=-4° is close to L-1 and L-2 configurations as 1.882. Due to its low lift curve slope, L-3 provides a smaller lift coefficient than other landing configurations, even with greater flap deflection. Its stall angle of attack is observed at α=16°, similar to a clean airfoil and retracted flap in cruise conditions (see Figure 3.22(a)). Also, its maximum lift coefficient value is equal to 2.868, which is 8.87% and 13.15% lower than the maximum lift coefficients of L-1 and L-2 configurations, respectively. The mean pressure distribution comparison of L-2 and L-3 configurations at their stall angles of attack are depicted in Figure 3.25. Even L-3 configuration experiences a greater angle of attack, the magnitude of the pressure coefficient of L-2 configuration on the upper surface of the main element is noticeably greater than L-3 configuration. The

flattening in mean pressure distribution on the flap's surface, which is the natural result of a separation bubble for L-3 configuration, is observed. The location of the separation and reattachment points are around $0.01c$ and $0.81c$, respectively. The huge clockwise laminar separation bubble and counter-clockwise vortex formation behind this bubble are depicted in Figure 3.27. Also, this vortex formation is observed for each angle of attack as low as -4°. As aforementioned, flow separation does not occur on the flap surface for L-2 configuration at α=14°. Due to the existence of counter-clockwise vortex, the peak mean pressure coefficient at the trailing edge of the flap for L-3 configuration is observed as -1, while it is equal to almost 0 for L-2 configuration (see Figure 3.25).

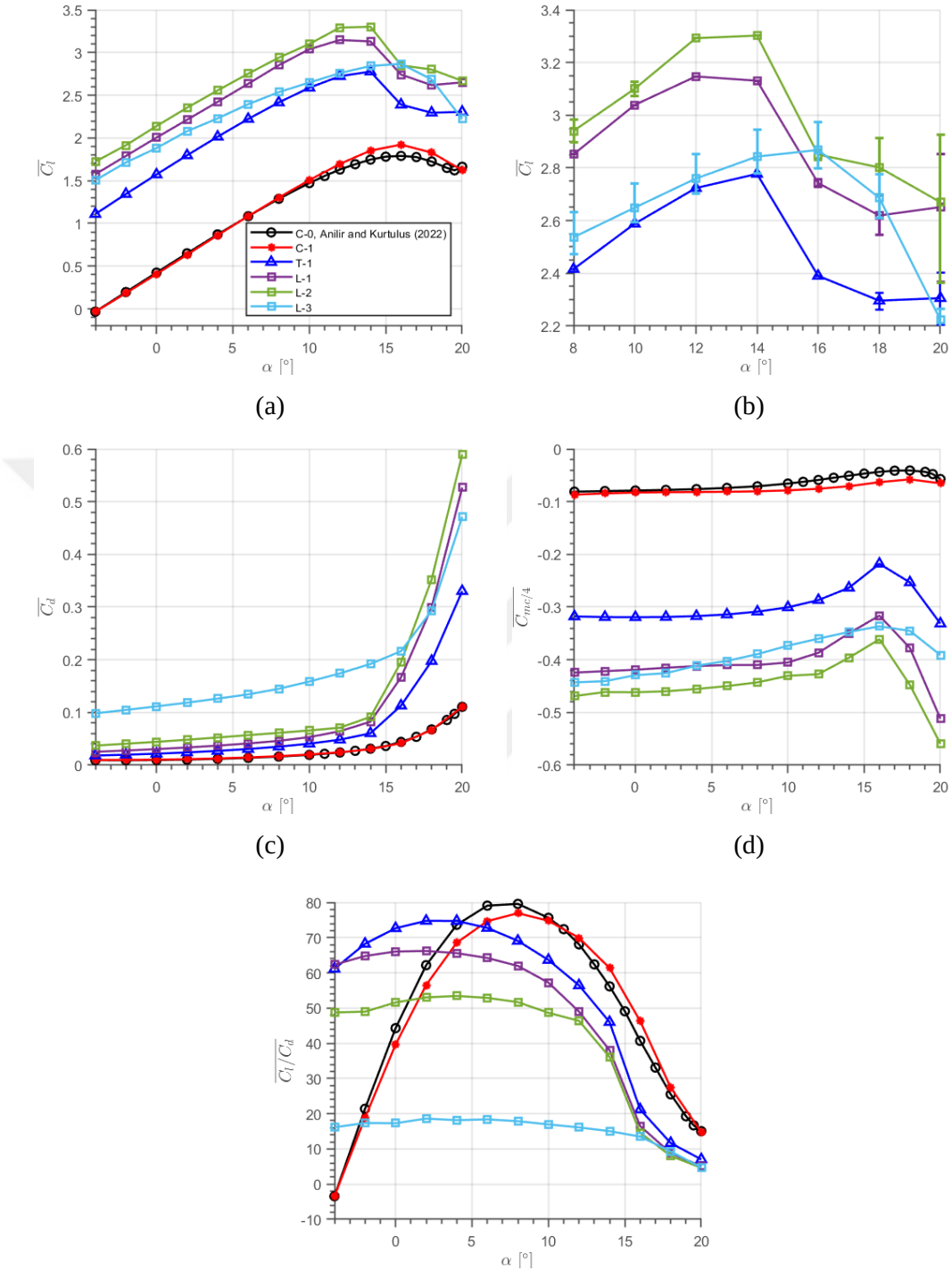
Figure 3.26 and Figure 3.27 show the time-averaged velocity streamlines for several configurations and angles of attack. The counter-clockwise vortex in the flap cove for all deployed flap configurations is observed. The flow starts to separate at the entrance of the flap cove and reattaches at a certain location close to the slot-lip. The horizontal length of the vortex almost remains constant while increasing the angle of attack for a certain configuration. Moreover, the horizontal length increases with increasing flap deflection. From T-1 to L-3 configurations, these lengths are obtained as $0.45x_{cove}$, $0.60x_{cove}$, $0.65x_{cove}$, $0.72x_{cove}$, respectively. Wentz and Fiscko (1978) made an assumption on separation and reattachment locations of the cove vortex and modified cove shape to effective shape that helped them obtain better theoretical pressure coefficient results than true cove shape while comparing experimental results.

The initial flow separation is observed at α=12° on the trailing edge of SD7062 airfoil for C-0 configuration presented in Sec. 3.1. Afterwards, the length and the height of the separation bubble gradually increase. For another cruise condition configuration (C-1), there is no flow separation observed below the stall angle of attack of 16°. Even at α=16°, the clockwise vortex forms at the aft portion of the main airfoil with a separation point of $0.73c$ and a reattachment point of $0.85c$, whereas the flow stays completely attached to the flap surface. The length of the

vortex is equal to $0.12c$ which is one-third of the vortex in C-0 configuration. This demonstrates around 6% difference in the drag coefficient between C-0 and C-1 configurations. Above α=16°, the new counter-clockwise vortex is formed at the wake of the main airfoil, and the clockwise vortex bursts. For T-1 configuration, the flap deflection angle and the gap size are relatively small, and the flap is close to the cove of the main airfoil. As stated by Woodward et al. (1988) and Bruce and McMasters (1990), the strong interactions between the wake of the main airfoil and the flap lead to the reduction in suction peak and hence to fully attached flow over flap's surface for a small gap size on or before stall. Moreover, the small gaps produce a lift curve rounded on the top, also called a conventional lift curve. Woodward et al. (1988) clearly indicated that the thickness of the main airfoil wake increases as the attack angle increases, which is enlarged in the flow over the flap. The displacement effect of this thick wake causes great lift losses. Figure 3.27 presents mean velocity streamlines of L-1 and L-2 configurations at pre- and post-stall conditions. L-1 and L-2 configurations show the feature of intermediate gap size described by Woodward et al. (1988) and Bruce and McMasters (1990). Due to inadequate interference between the main airfoil and the flap, the flap's suction peak increases, which leads to flow separation over the flap at low angle of attack (see Figure 3.26 and Figure 3.27). As the angle of attack increases, the wake of the main airfoil increases resulting in a lower suction peak of the flap. Hence, the resulting interference becomes enough to keep the flow attached. The flat top on the lift curve of these two configurations is observed as expected from the references. The size of the separation bubble for L-1 is always smaller than L-2 below α=14°. Moreover, the flow turns out to attached flow over the flap surface at α=10° until post-stall condition. While both the gap size and the flap deflection enhance from L-1 to L-2, the interference between the wake and the flap is not sufficient to keep flow attached, and the length of the separation bubble (l_b) almost remains constant around l_b=0.16c until α=12° for L-2 configuration. At α=14°, there is no boundary layer separation in the surface. Although the flow is attached to the flap surface, the flow phenomenon called off-surface flow separation

(Guseva, 2018; Ross, 1997; Ying et al., 1999) is observed (see Figure 3.27, first and second column). This off-surface flow separation is more efficient than boundary layer flow separation. Also, the rate of the lift gain is depressed by the off-surface separation that limits to maximum lift for surface-attached flow conditions (Ying et al., 1999). For L-3 configuration, the gap size is 32%, 68%, and 132% greater than L-1, L-2, and T-1, respectively. Also, it shows the feature of the largest gap. The wake and the flap interactions are insufficient to keep the flow attached to the flap surface. A huge separation bubble is observed for each angle of attack. Demel et al. (2016) experimentally investigated completely separated flow over the fowler flap at δ_f=40° for all gap and overlap configurations at a Reynolds number of about 1×10^6, similarly to our L-3 configuration.

For each configuration except L-3, the flow is fully attached over the surface of the flap at their stall angle of attack. According to Ying et al. (1999), if the gap and overlap are well-optimized, there is no separation in the boundary layer on the flap formed at the stall angle of attack. This demonstrates the aforementioned observations that show huge separation bubble for the case of L-3 with $0.037c$ gap size larger than the optimum gap size. Ying et al. (1999) also state that the main airfoil carries higher loading than the flap. As angle of attack enhances, lift force on the main airfoil increases, while the flap continuously unloads. Smith (1975) described these phenomena as a circulation effect and damping effect. In our cases, a gradually decreasing trend in flap suction peak of pressure is observed as the angle of attack increases. Figure 3.28 inspects the mean pressure coefficient distribution around the main airfoil and the flap at α=0°, 6°, 10°, 14°, and 20° for L-2 configuration. This figure demonstrates that the suction peak and the loading on the main airfoil noticeably increase as the angle of attack increases below the stall angle. Also, the suction peak of the flap below α=14° is significantly greater than α=14° that leads to the flow separation at the trailing edge. The thickening wake results reduction in the suction peak of the flap that permits an attached flow at α=14°. In the post-stall case of α=20°, the flap is highly loaded, but a larger unload in the main airfoil leads to a loss in lift.



(a) (b) (c) (d) (e)

Figure 3.22: Mean aerodynamic coefficients of clean airfoil, retracted, and deployed flap conditions for angles of attack from α=-4° to α=20°, (a) $\overline{C_l}$ - α, (b) $\overline{C_l}$ - α at around stall region with bars representing the minimum and maximum peaks in the oscillations, (c) C_d - α, (d) $C_{m_{\frac{c}{4}}}$ - α, (e) $\frac{\overline{C_l}}{C_d} - \alpha$ curves

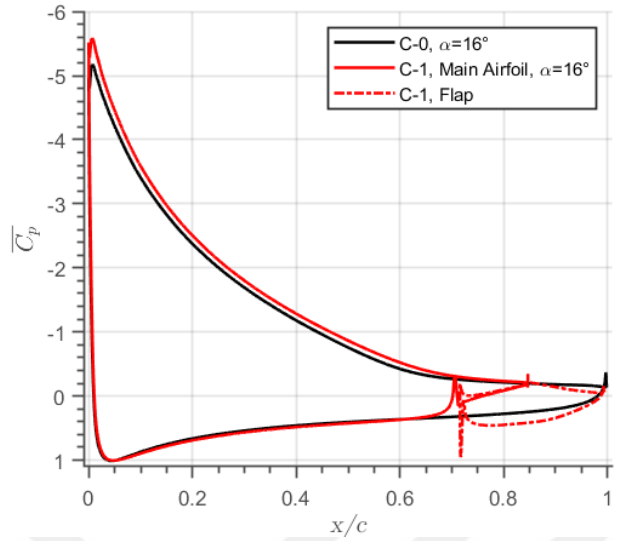


Figure 3.23: Mean pressure coefficient distributions for C-0 and C-1 configurations at α=16°

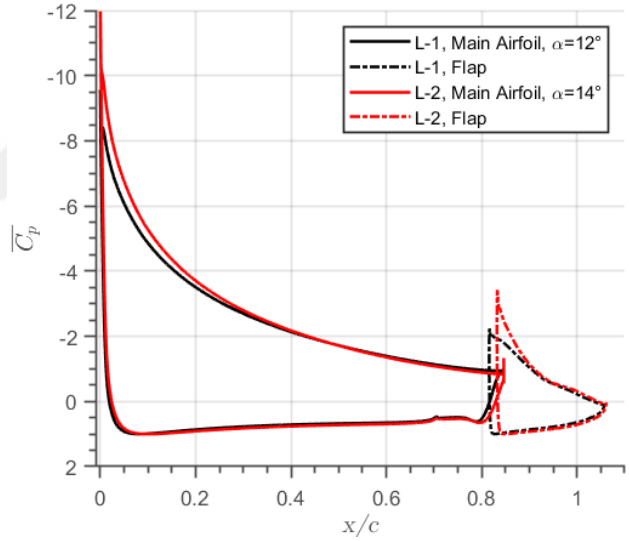


Figure 3.24: Mean pressure coefficient distribution for L-1 configuration at α=12° and L-2 configuration at α=14°

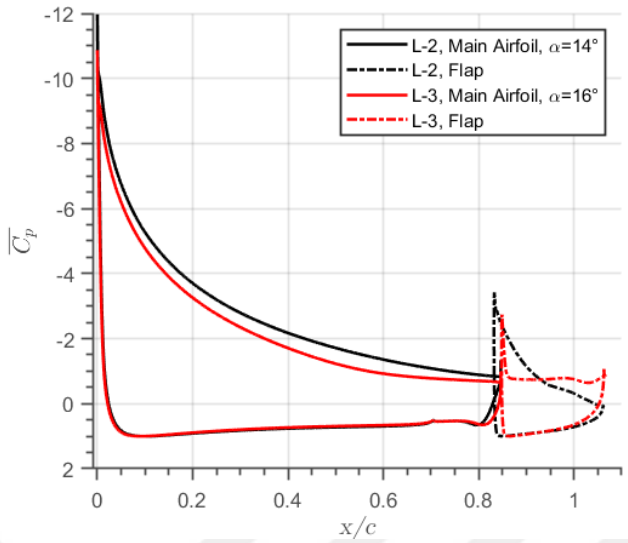


Figure 3.25: Mean pressure coefficient distribution on the main airfoil and the flap for L-2 configuration at α=14° and L-3 configuration at α=16°

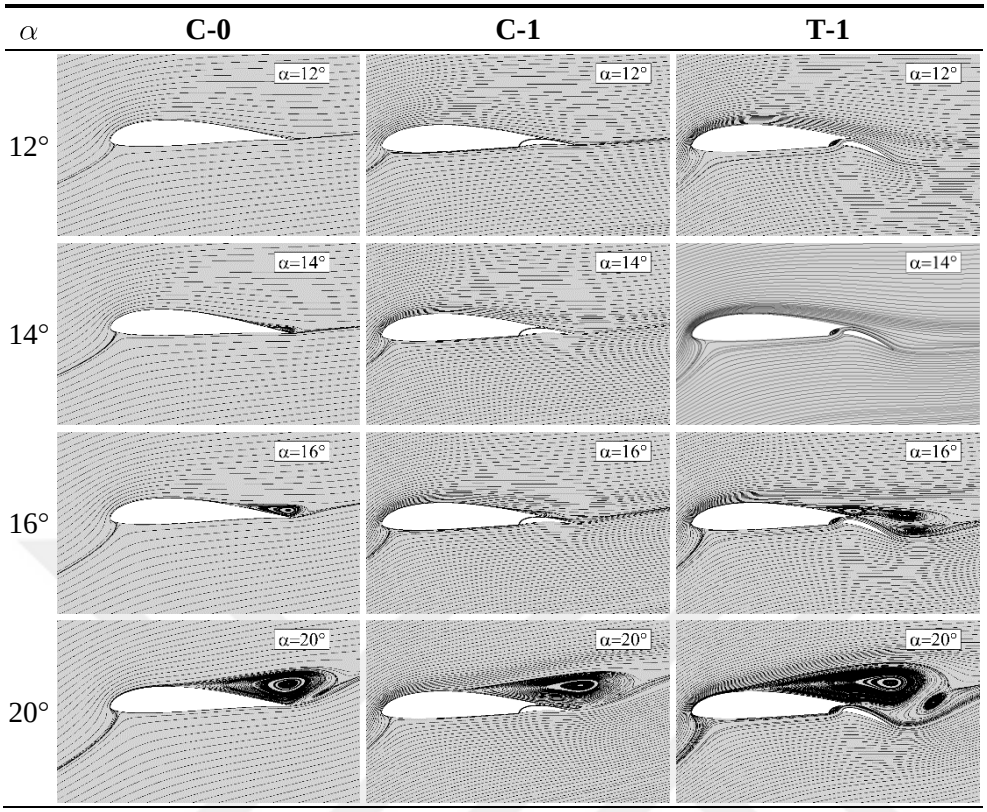


Figure 3.26: Mean velocity streamlines for C-0, C-1, and T-1 configurations at α=12°, 14°, 16°, and 20°

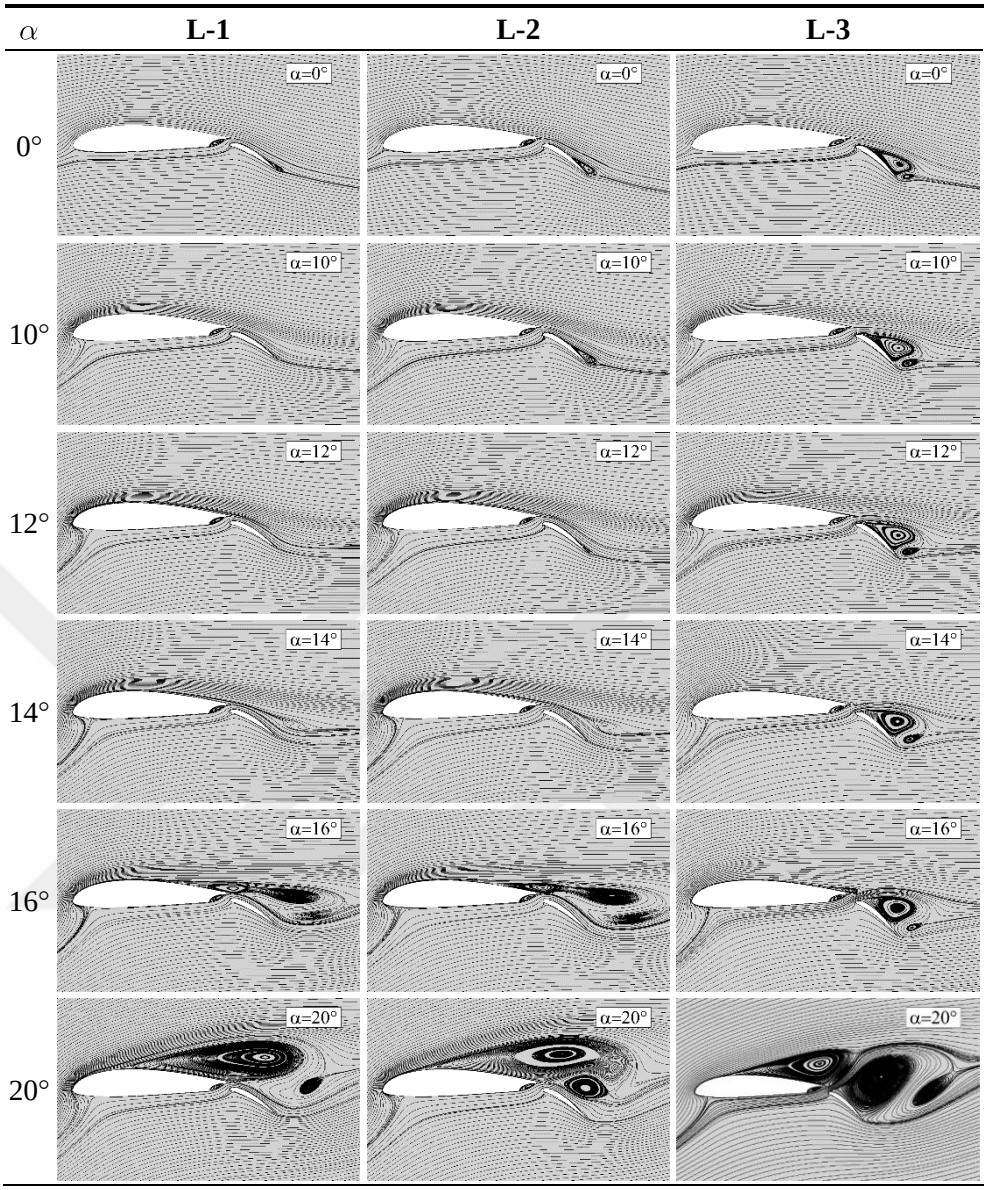
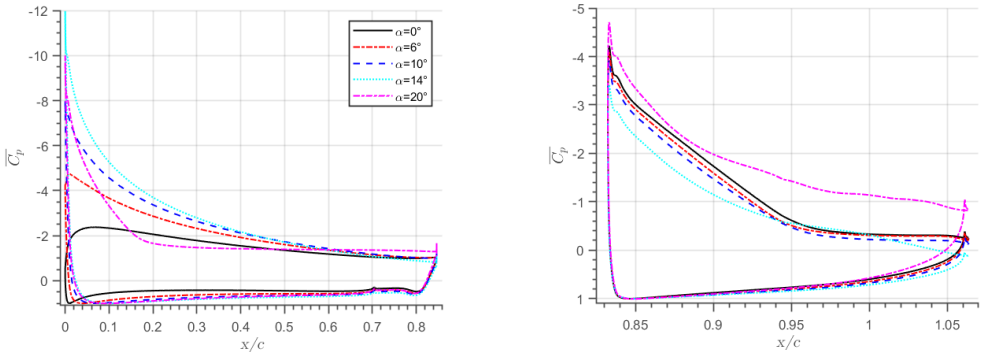


Figure 3.27: Mean velocity streamlines for L-1, L-2, and L-3 configurations at α=0°, 10°, 12°, 14°, 16°, and 20°



(a) (b)

Figure 3.28: Mean pressure coefficient distribution around the main airfoil and the flap at pre- and post-stall angles of attack for L-2 configuration, (a) Main airfoil, (b) Flap

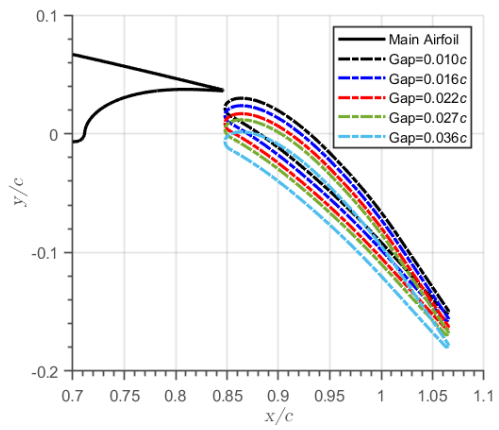
3.2.2 Effect of Gap Size on the Aerodynamic Performance

In this section, the effect of gap size on aerodynamic performance for landing analysis with 40° deployed flap is investigated at two different angles of attack, which are α=0° and α=12°. In the literature, the optimum flap position study for different designs was performed (Ashby, 1996; Foster, 1970; Wentz and Ostowari, 1983; Wentz and Seetharam, 1974). The optimum position of the flap considering the maximum lift coefficient is usually different than the optimum position for the maximum lift-to-drag ratio. Moreover, the optimal position of the flap is small, and even a slight change in position would cause a reduction in the maximum lift coefficient. For all analyses, the overlap size is kept constant as -0.004c because the gap size is more critical than the overlap size for the optimum lift (Foster et al., 1970; van Dam, 2002). Figure 3.29 shows mean lift and drag coefficients and lift-to-drag ratio curves for five different gap sizes ranging from 0.010c to 0.0037c. The numerical results show a strong sensitivity of the lift coefficient to the gap size. The variation in lift coefficient with respect to the gap size for α=0° is less than α=12°. As clearly seen in Figure 3.29, the mean lift coefficient reaches its optimum value where gap size is equal to 0.016c for both α=0° and α=12°. The mean lift coefficient increases with increasing the gap size from 0.010c to 0.016c. Afterwards, it decreases with a further increase in the gap size. At α=0°, even the

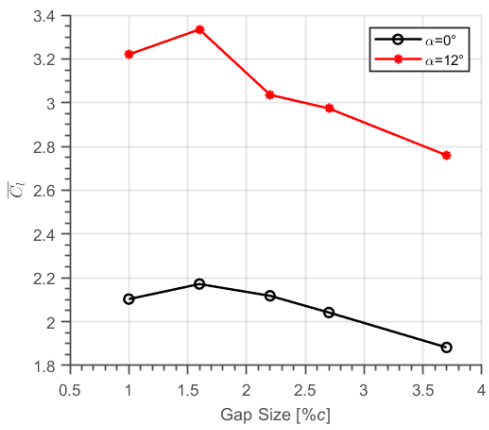
mean lift coefficient gradually decreases with increase in the gap size higher than 0.016c. The gap size of 0.022c produces a greater lift coefficient of 2.118 than the gap size of 0.010c, which provides the lift coefficient of 2.102. At α=12°, the dramatic fall in the lift coefficient is followed by a little raise of the gap size between 0.016c and 0.022c. The mean lift coefficient at α=0° and α=12° for the gap size of 0.016c are equal to 2.171 and 3.335, respectively. Moreover, these two results are 1.44% and 1.27% greater than the results of L-2 configuration, which provides the highest lift coefficients at these two angles of attack. The drag coefficient varies in a monotonic manner with respect to the flap gap for 0° angle of attack. The drag coefficient is observed to increase as gap size increases. At α=12°, the gap size of 0.016c provides the smallest drag and the highest lift coefficient that lead to the highest lift-to-drag ratio in the gap optimization study. The huge separation bubble that covers more than half of the flap suction surface is observed for each case at α=0°, similarly to the study of Demel et al. (2016). Also, the size of the cove vortex increases with increasing gap size. Off-surface flow separation is formed for 0.010c and 0.016c gap sizes at α=12°. This separation is greater for 0.010c case that leads to larger lift loss than 0.016c case. The flap boundary layer separation due to weak interaction between the main airfoil wake and the flap is observed at the larger gap sizes.

Wentz and Seetharam (1974) presented constant maximum lift coefficient contours considering flap gap and overlap sizes for GA(W)-1 airfoil with 0.30c fowler flap for 35° and 40° flap deflection at Re=2.2×10^6. The authors obtained optimum flap gap and overlap sizes for 40° flap deflection according to the maximum lift coefficient (C_{lmax}=3.8) as 0.027c and -0.007c, respectively. The maximum lift coefficient on their study with our optimized gap and overlap sizes (gap=0.016c and overlap=-0.004c) equals C_{lmax}=3.6, which is quite high. Wentz and Ostowari (1983) studied the effect of the flap gap on the aerodynamic forces at 35° deflected fowler flap for narrow (0.02c), optimum (0.03c), and wide (0.05c) gap sizes with a constant overlap of 0.012c. Below the stall angle, the lift coefficients of narrow and optimum gaps are close, but the wide gap deviates. The maximum lift coefficient

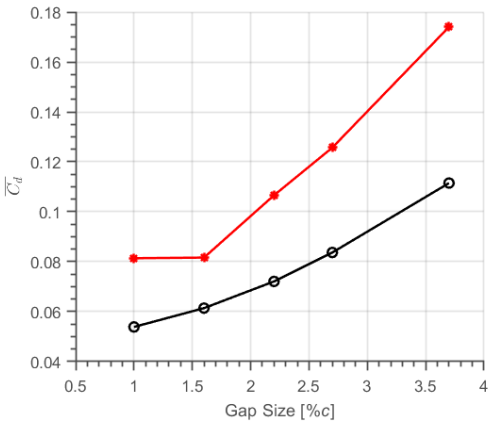
for their optimum gap is equal to 3.71. Foster et al. (1970) observed lift loss due to the confluent boundary layer for the cases below the optimum gap size. Also, the optimum gap size is observed approximately as $0.020c$, which can be accepted as an intermediate gap. Ashby (1996) performed a wind tunnel experiment at Re=5×10^6 on NACA 63$_2$-215 ModB two-element airfoil for four different flap gaps varying from $0.02c$ to $0.05c$. Even if the $0.02c$ gap provides a significantly greater lift coefficient than $0.03c$ gap below its stall angle of attack, the stall angle of attack and the maximum lift coefficient of $0.03c$ gap is greater than $0.02c$ gap. The effect of the flap position on the maximum lift coefficient of 40° single slotted is shown by Woodward et al. (1988). Our optimum gap and overlap values are in the optimized region of their study.



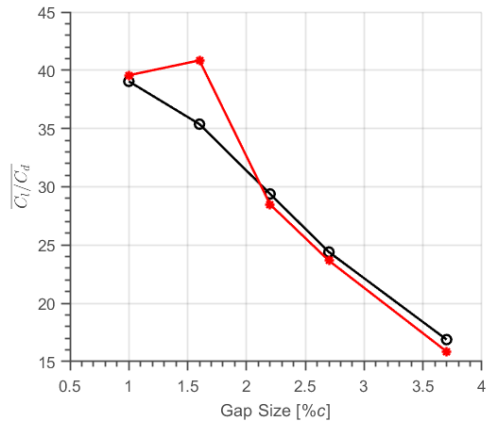
(a)



(b)



(c)



(d)

Figure 3.29: Flap positions, and mean aerodynamic coefficients at α=0° and α=12° with five different gap sizes for L-3 configuration, (a) flap positions (b) $\overline{C_l}$ - α, (c) $\overline{C_d}$ - α, (d) $\frac{\overline{C_l}}{\overline{C_d}}$ - α curves

3.3 3D Very Light Aircraft's Wing with Comparing Various Wing Parameter

In this section, the crucial characteristics of a tapered wing with Γ=5° and Γ=0°, and a rectangular wing with Γ=0° are discussed discerned from URANS results considering mean aerodynamic coefficients and flowfield over the wing at pre and post-stall regimes. The numerical simulations are performed at α=-6°, -2°, 0°, 5°, 10°, and from 12° to 20° with 1° increment for VW1 (baseline configuration) and RW1. The VW2 is only analyzed around the stall (α=16°, 17° and 18°) (Anilir and Kurtulus, 2023c).

3.3.1 Mean Aerodynamic Coefficients

Figure 3.30 presents mean aerodynamic coefficients of lift, drag and lift-to-drag ratio as a function of angle of attack. Initially, it is noticed that both the tapered (VW1) and the rectangular (RW1) wings produce very similar lift and drag forces until about α=14°. Nevertheless, RW1 has slightly less lift and greater drag than VW1. As a result, the aerodynamic efficiency, which is evaluated by the lift-to-drag ratio, of VW1 is merely higher than RW1 in the range of investigated angles of attack. Also, the tapered wings with dihedral (VW1) and no dihedral (VW2) angles exhibit almost identical lift coefficients near the stall (at α=16°, 17°). Therefore, it can be safely assumed that these wings follow the same lift curve prior to stall. The zero-lift drag coefficients are found as C_{D0}=0.0105 and C_{D0}=0.011 at α=-5.8° for VW1 and RW1 configurations, while it is equal to α=-3.7° for 2D SD7062 airfoil. The finite wings have greater lift coefficients than SD7062 below around α=2°. Beyond this angle, SD7062 airfoil always indicates a relatively higher lift force.

Since the lift curves show highly linear behavior at moderate and low angles of attack, the lift-curve slope of the RW1 is obtained ($C_{L\alpha}$=4.695 1/rad) and compared with approximations proposed in the literature. The lift-curve slope predictions introduced by Helmbold (1942) with a compressibility correction and Gutierrez-Castillo et al. (2021) are described in Eq. 14 and Eq. 15 by symbols of $C^{*}_{L\alpha}$ and $C^{**}_{L\alpha}$, respectively.

$$C^{*}_{L\alpha} = \frac{C_{l\alpha}}{\sqrt{1 - M^2 + \left(\frac{C_{l\alpha}}{\pi \mathrm{AR}}\right)^2} + \frac{C_{l\alpha}}{\pi \mathrm{AR}}} \qquad (14)$$

$$C^{**}_{L\alpha} = \left(\frac{2\pi}{1 + \frac{k_1}{\mathrm{AR}^{-1}}}\right)\left(\frac{k_2}{1 + \frac{10^6}{Re}}\right)^{1/5} \qquad (15)$$

where $C_{l\alpha}$ is the sectional lift-curve slope of the wing (lift-curve slope of its airfoil), k_1 and k_2 are the coefficients used to fit the results.

Gutierrez-Castillo et al. (2021) studied experimentally on the rectangular flat plate with various aspect ratios and Reynolds numbers. The Reynolds numbers ($40\times10^3<Re<200\times10^3$) that experiments were performed are very low compared to our case. On the other hand, Helmbold (1942)'s correlation is invariant to Reynolds number and depends on the sectional lift-curve slope and aspect ratio of the wing. In Figure 3.30, $C^{*}_{L\alpha}$, $C^{**}_{L\alpha}$ with k_1=4.5 and k_1=5.21 are provided. The semi-empirical correlations and low-order numerical simulation XLFR5-3D panel code (XFLR5 Guidelines) results are compared with CFD data in terms of relative error ($e_1 = \left|\frac{C_{L\alpha}-C^{*}_{L\alpha}}{C_{L\alpha}}\right| \times 100$), $C^{**}_{L\alpha}$ with k_1=4.5 is almost perfectly agreed with CFD results (e_1=0.94%). $C^{*}_{L\alpha}$, and $C^{**}_{L\alpha}$ with k_1=5.21 overestimates with e_1=13.25% and e_1=7.17%, respectively, whereas the 3D Panel code predicts a greater $C_{L\alpha}$ with e_1=6.45%. $C^{**}_{L\alpha}$ values with k_1=4.5 agrees well with the results of the current study. Helmbold's correlation was obtained for low aspect ratio (AR<4) straight wings, even if our wing fit its criteria, this correlation is worser than the other predictions.

Focusing on the stall regime, wing stall characteristics depend greatly on the taper ratio. The presence of taper postpones stall to a larger angle of attack and therefore favors a higher lift coefficient in this Reynolds number, as evident in Figure 3.30(a). The maximum lift coefficient and the stall angle of attack of VW1 and RW1 are indicated as C_{Lmax}=1.679 and α_{stall}=17°, and C_{Lmax}=1.580 and α_{stall}=15°, respectively. In general, it is expected to observe lower C_{Lmax} and higher α_{stall} for finite wing than 2D airfoil, as our VW1 and SD7062 airfoil. However, RW1 has both lower C_{Lmax} and α_{stall} than the airfoil. According to McVeigh and Kisielowski (1971)'s lifting line theory calculations which agree with experimental data, an increase in taper ratio is accompanied by maximum lift coefficient reduction to different extents at high Reynolds numbers. Allen (1953) found that the wing of AR=4 with a 0.5 taper ratio leads to a higher maximum lift coefficient than the untapered one at our studied Reynolds number. At low Reynolds number of 1.2×10^5, the maximum lift coefficient of a flat plate of AR=4 decreases as the taper ratio increases from 0.5 to 1, experimentally investigated by Ananda et al. (2015). As a counterexample to previous findings, having a taper ratio of 0.5 leads to a decrease in maximum lift coefficient and stall angle of attack compared to rectangular wing according to RANS simulations of Petrilli et al. (2013) on the wing of AR=12.

A dihedral angle rise does not influence the stall angle of attack and only minimally favors the maximum lift coefficient. The reduction of maximum lift coefficient is observed as about 1.251% due to the decline of dihedral (from VW1 to VW2). The main difference between the wing with dihedral and no dihedral is observed above the stall. VW2 experiences steeper drag increment, and detrimental lift loss just exceeds the stall than VW1 (see Figure 3.30(a)). The details of the stall characteristics will be discussed in Sec. 3.2.

Figure 3.30(d) indicates the lift coefficient obtained by URANS and XFLR5 3D Panel code. 3D Panel code simulations are significantly under predicts except for

the maximum lift. Since the 3D panel method is essentially linear, the accurate prediction of lift around the stall is just a coincidence.

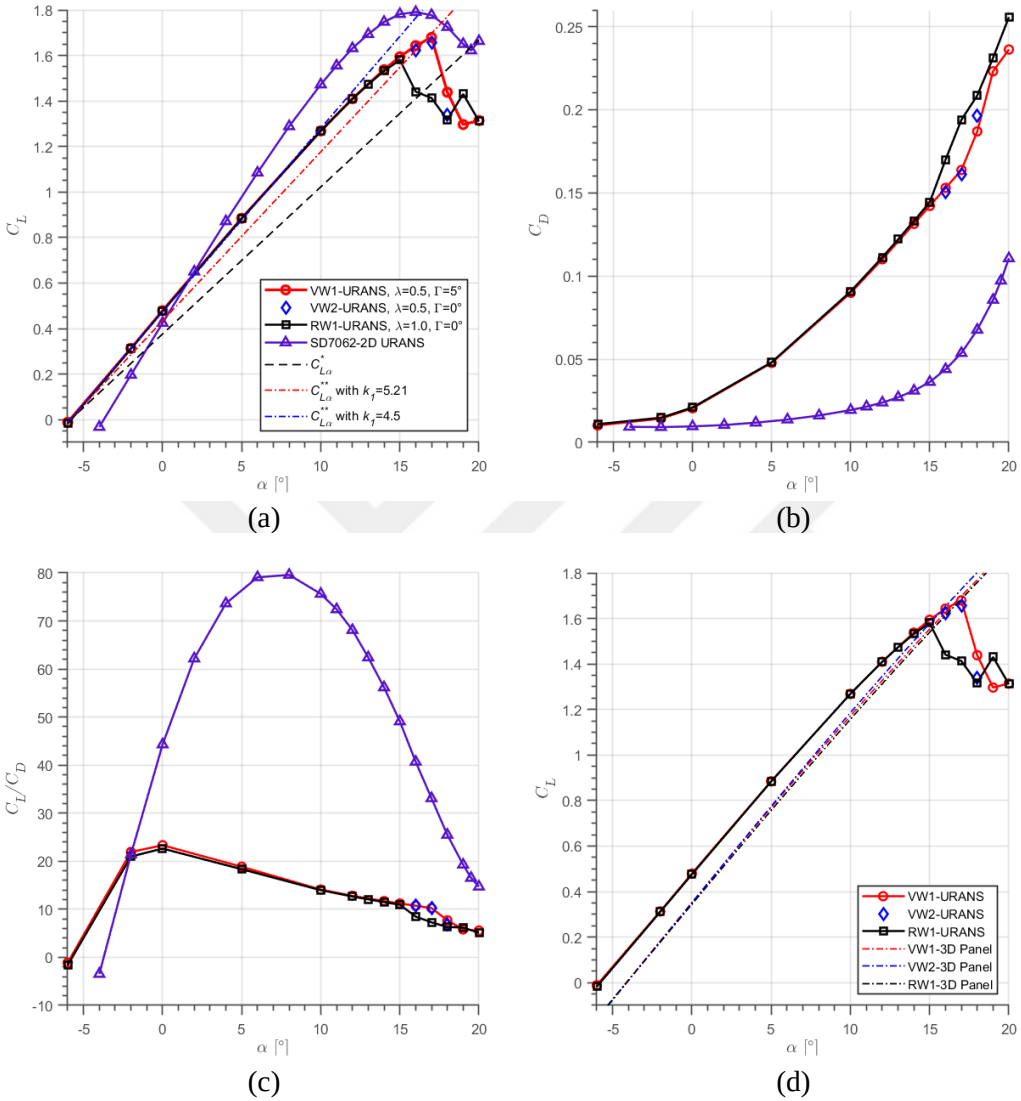


Figure 3.30: Time-averaged aerodynamic coefficients versus angle of attack for VW1, VW2, RW1 and SD7062 airfoil at $Re \approx 5 \times 10^6$, (a) C_L vs. α, (b) C_D vs. α, (c) C_L/C_D vs. α, and (d) comparison of URANS and 3D Panel code simulations' results

3.3.2 Flow Structures

The flow structures on the suction side of the wings considering the mean surface streamlines and spanwise profiles of lift distribution are examined in order to

describe the reasons behind the different stall behaviors. Figure 3.31 indicates mid-span sectional lift coefficient of the wings are compared with the SD7062 airfoil. At the mid-section, RW1 experiences a plateau-like gentle stall due to the present of stall cell close to the root region. As seen from Figure 3.33, these stall cell formation results in almost attached flow and the peak of sectional lift coefficient in the vicinity of the mid-span at α=16° and 17°. For VW1, it exhibits abrupt loss in the lift, especially at α=19° and 20°. Since the center of the stall cell moves towards to mid-span (see Figure 3.35(d)), drop in lift becomes extremely severe. Figure 3.32 and Figure 3.33 depict the variation of sectional lift coefficients along the spanwise direction (y/b=0 and y/b=1 refer to root and tip sections) along with surface streamlines over the suction surface of VW1, VW2 and RW1 at α=15°, α=16°, α=17°, and α=18°. It should be noted that VW1 and VW2 experience stall at α=17°, whereas the stall angle of attack of RW1 and 2D SD7062 airfoil are observed at 15° and 16°, respectively (see Figure 3.30). Moreover, SD7062 airfoil undergoes gentle stall; on the other hand, the severe stall (abrupt stall) is observed for VW1, VW2 and RW1 (the severity of the stall is defined as s_{stall}=$(C_{L_{\alpha_{stall}}} - C_{L_{\alpha_{stall+1°}}})/C_{L_{\alpha_{stall}}}$, it increases from SD7062 to VW2 ($s_{stall_{VW1}}$ =14.35%, $s_{stall_{VW2}}$=19.32%, $s_{stall_{RW1}}$=8.82%, $s_{stall_{SD7062}}$= 0.74%).

One of the drawbacks of the strong taper is that the tip experiences a lower Reynolds number than the root (for VW1 and VW2, sectional Reynolds number linearly varies from Re_{tip}=3.25×10^6 to Re_{root} =6.33×10^6) which may result in a sooner stall for the tip (Sadraey, 2014). This tip stall can cause a sudden unintended roll motion, which is an undesirable phenomenon, especially during the landing. The raise of sectional lift coefficient from root to around the mid-span is usually denoted as a tip stall risk of a tapered wing. On the other hand, the minimum induced drag is achieved when the spanwise lift distribution is an elliptical shape. The wing with 0.45 taper ratio produces a similar lift distribution to the elliptical one (Raymer, 2018). For λ=0.5 wing, it is expected to observe mid-span stall, and

it generally shows a favorable balance between good stall characteristics and low induced drag (Gudmundsson, 2014).

According to Sec. 3.1, SD7062 airfoil exhibits trailing edge stall behavior at Reynolds number of $5\times10^{6,}$ which is expected to observe for thick airfoils ($t/c\geq15\%$). Trailing edge separation is also observed for analyzed wings at the pre-stall regimes. The separation line occurs close to the wingtip and then dies out at the root by leading to the formation of a surface vortex for VW1 and VW2. The reversed flow region increases, and the zigzag-like separation line becomes more distinct with increasing angle of attack. The trailing edge separation of RW1 is more disordered compared to the other two wings. Several large and small vortices are formed without any periodic spanwise development. Even the small stall cell (small compared to stall cells formed just above the stall angle) can be identified close to the root in Figure 3.32. The flow is highly three-dimensional over the separation region, which exhibits spanwise variation. Both VW1 and VW2 experience mid-span lift distribution peaks around $0.53y/b$ and $0.59y/b$ at α=16° and α=17°, respectively. Moreover, VW1 is slightly more loaded than VW2 from root to mid-span peak, but this load difference is in decline trend towards to mid-span. For the rest of the wing, excluding the certain near wingtip region, the sectional lift decreases because of the induced downwash from the tip vortices that lowers the effective angle of attack. Moreover, VW1 and VW2 are in agreement except wing tip peak lift; in case it is distinguishable, but not prominent outcome. Therefore, it can be concluded that 5° dihedral leads to an imperceptibly greater lift in the vicinity of the root region and wingtip peak near the stall. Garmann and Visbal (2017) observed a sudden peak in the lift distribution close to the wingtip due to the presence of the tip vortex. They found an almost linear correlation between lift peak and vortex strength, which strengthens with an increment of the angle of attack for pre-stall conditions. In our study, lift peak of the tip increases with increasing angle of attack before the stall for all three wings. However, VW1 and VW2 experience a decline, while RW1 continues to exhibit a gradual rise beyond the stall angle.

At the onset of the stall, the highly three-dimensional flow structure stall cell (SC) is observed. One of the stall cell characteristics is that severe drops in spanwise lift distribution are observed at the center of the stall cell (minimum lift distribution excluding the wingtip region occurs due to the center of the stall cell). The effect of stall cells on the local lift distribution is very rarely studied in literature such as by Manolesos et al. (2014). Boiko et al. (1996) proposed the highly appreciated formula in literature to predict the number of stall cells formed on the rectangular wings (see Eq. 16). The stall cell with a single vortex pair is initially observed at α=16° for the rectangular wing. Also, the formula's corresponding to the number of stall cell prediction is 1, in agreement with the formula's prediction.

$$n = \frac{AR}{17.2} \times k \times \tan\alpha_v \tag{16}$$

where n is the number of stall cells, k is the distance between the earliest separation point and the vortex core non-dimensionalized with chord length, α_v is the angle of attack that stall cell is initially observed.

The geometric constraints (center distance (d_{SC}), length (l_{SC}), width (w_{SC}), and area (S_{SC})) of stall cells are introduced in Figure 3.34 by using similar definitions given by Manolesos and Voutsinas (2014). The length of the stall cell (l_{SC}) represents a chordwise distance between the most upstream point of the stall cell and the trailing edge of the wing. The stall cell center distance (d_{SC}) is the distance of the center of the stall cell from the root of the wing. The width and area of the stall cell are measured for only total quantity because the boundary of the first and second stall cells is ambiguous. Figure 3.35 shows the l_{SC}, w_{SC} and d_{SC} as a function of angle of attack. To make it clear, the first SC is described as a stall cell observed close to the root if any other stall cell occurs (see Figure 3.33(c) as an example). In this study, the second stall cell is only observed for RW1 at α=18° and α=20°.

As hereinbefore stated, it is expected to observe the stall closer to the wingtip for tapered wings compared to untapered wings. In that way, the stall initially develops

two times away from the root for VW1 and VW2 than RW1 (d_{SC}'s are doubled). On the other hand, the positive effect of having a dihedral on the root region and the whole wing's total lift loading below the stall is discussed; furthermore, this influence becomes remarkable just beyond the stall. The presence of a dihedral not only pushes the stall towards to root but also leads to notable less l_{SC}, w_{SC}, and S_{SC} (see Figure 3.35). Considering the taper ratio effect, λ=0.5 delays α_{stall} and improves C_{lmax}, thus the critical angle of attack, in which stall cell first appears, increases from α=16° to α=18° for λ=1 and λ=0.5, respectively. Since the first stall cell developed for VW2 has a much larger l_{SC}, w_{SC} and S_{SC}, and results in more than doubled stall severity than RW1, it can be said that the lower taper ratio causes more detrimental stall behavior. In order to get a larger stall angle of attack and maximum lift coefficient along with a smoother stall, it is wise to use a moderate tapered wing with dihedral, according to our findings.

There is a negative almost linear relation found between the minimum sectional lift coefficient and l_{SC}. Note from Figure 3.36(a), the slope of the minimum sectional lift coefficient versus l_{SC} curve-fit are very close for VW1 and RW1, thus it can be said that the linearity of this relation is regardless of the wing shape. The formula of curve-fit for all data is C_{lmin}=-1.743*($\frac{l_{SC}}{c_{local}}$)+2.506. Hence, a general trend of decreasing minimum spanwise lift distribution with increasing stall cell length is observed for most analyzed cases. Considering the stall cell area and the lift coefficient relation, the increase in stall cell area generally leads to less lift produced, as evident in Figure 3.36(b). The slope of VW1's curve-fit is steeper than RW1's curve because of the larger first stall cell area. However, the similar S_{SC} usually results in a closer C_L, for example, the corresponding C_L for $\frac{S_{SC}}{S}$=0.35 and 0.48 are equal to approximately 1.44 and 1.30 for both two wings, respectively. Therefore, the curve-fit for all three wings' data almost perfectly agrees with the curve-fit of RW1. The formula of curve-fit for all data is C_L=-0.537*($\frac{S_{SC}}{S}$)+1.58.

For VW1, each stall cell parameter grows as the angle of attack increases. The stall cell width covers half of the wingspan at α=18°, and this value reaches almost three-quarters of it at α=20° (Figure 3.35(c)). The rate of growth of these relatively decreases (especially for l_{SC} and S_{SC}) at α=20°, thus drag force increment is considerably declined and even lift force exhibits slight gain. For RW1, the first stall cell center remains constant as $0.12b$ until α=20°, and then decreases its half. The second stall cell is initially observed near the mid-span ($d_{2.SC}$=$0.36b$), and thereafter it disappears at α=19°. It again forms at α=20° by its center lying on $0.31b$. The w_{SC} and S_{SC} follow fluctuation trend due to the occurrence and disappearance of second SC. The abrupt decrease in the stall cell area is accompanied by a sudden lift gain at α=19° (see Figure 3.30(a)).

Figure 3.37 illustrates the flow structure in the wake of the wing and various chordwise slice planes placed at stall cell centers (y/b=0.06 and 0.31), at mid-span, at local (y/b=0.18) and at local (y/b=0.66) sectional lift coefficient peak regions for RW1 at α=20°. These are compared with 2D URANS simulations of SD7062. Manolesos et al. (2014) observed three types of vortex structures with RANS simulations. These vortex structures are called as stall cell vortex, separation line vortex (SLV), and trailing edge line vortex (TELV). The stall cell vortex starts normal to the wing surface and then continues downstream (Yon and Katz, 1998). The separation line vortex and trailing edge line vortex are defined as the vortex formed above the surface and aligned to the trailing edge but counter-rotating to TELV, respectively (see Figure 3.37(e)). In-plane streamlines maybe tend to unrealistic flowfield, especially under strong three-dimensionality, but they are highly used in the literature to understand flow better (Burtsev et al., 2021; Manolesos et al., 2014, Dell'Orso et al., 2016).

According to Dell'Orso and Amitay (2018), and Manolesos et al. (2014), the flow structure, similar to two-dimensionally separated flow, is observed at the stall cell center. Considering the flow at $\frac{y}{b}$=0.06 and $\frac{y}{b}$=0.31, the spanwise variation in the stall cell centerline is very limited, and in-plane streamlines resemble to severe

separated flow around the two-dimensional body. So, our findings are in line with their results. The minimum sectional lift coefficient at $\frac{y}{b}$=0.31 (C_{lmin}=0.92) is considerably lower than at $\frac{y}{b}$=0.06 for RW1 (C_{lmin}=0.98) due to stronger flow separation (the separation bubble grows, and the saddle point moves towards to downstream) even if the separation bubble lengths are very close (l_{SC}=0.90 and l_{SC}=0.91, respectively) (see Figure 3.36 and Figure 3.37). Although the flow looks fully attached in in-plane streamlines except for a small vortex observed close to the trailing edge for $\frac{y}{b}$=0.18, it exhibits extensive separation and spanwise variation, as evident from mean surface streamlines (see Figure 3.37(a)) and flattening in the mean pressure distribution (see 11-b). At the location of y/b=0.66 that exhibits a peak in the sectional lift coefficient favors an optimum location, in which the downwash effect of the tip vortex and the stall cell are coupledly diminished. An almost negligible small vortex node is observed at the trailing edge. The suction peak in the mean pressure coefficient in this section is greater than the other sections. Also, the relatively larger pressure difference in the upper chord is the main reason for generating a higher lift. The three-dimensional flow structures in the wake of the RW1 are visualized with vorticity magnitude contours and iso-surfaces of Q-criterion (Hunt et al., 1988) in Figure 3.37(c) and Figure 3.37(d), respectively.

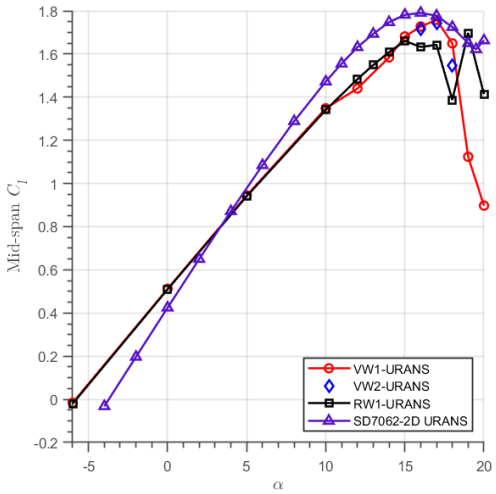
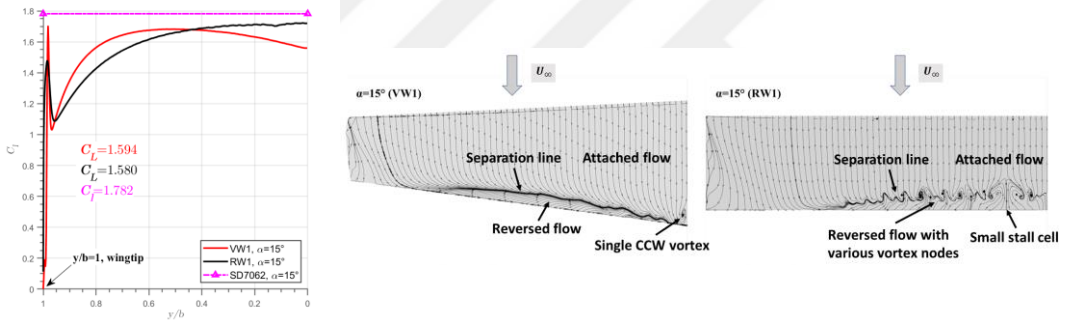
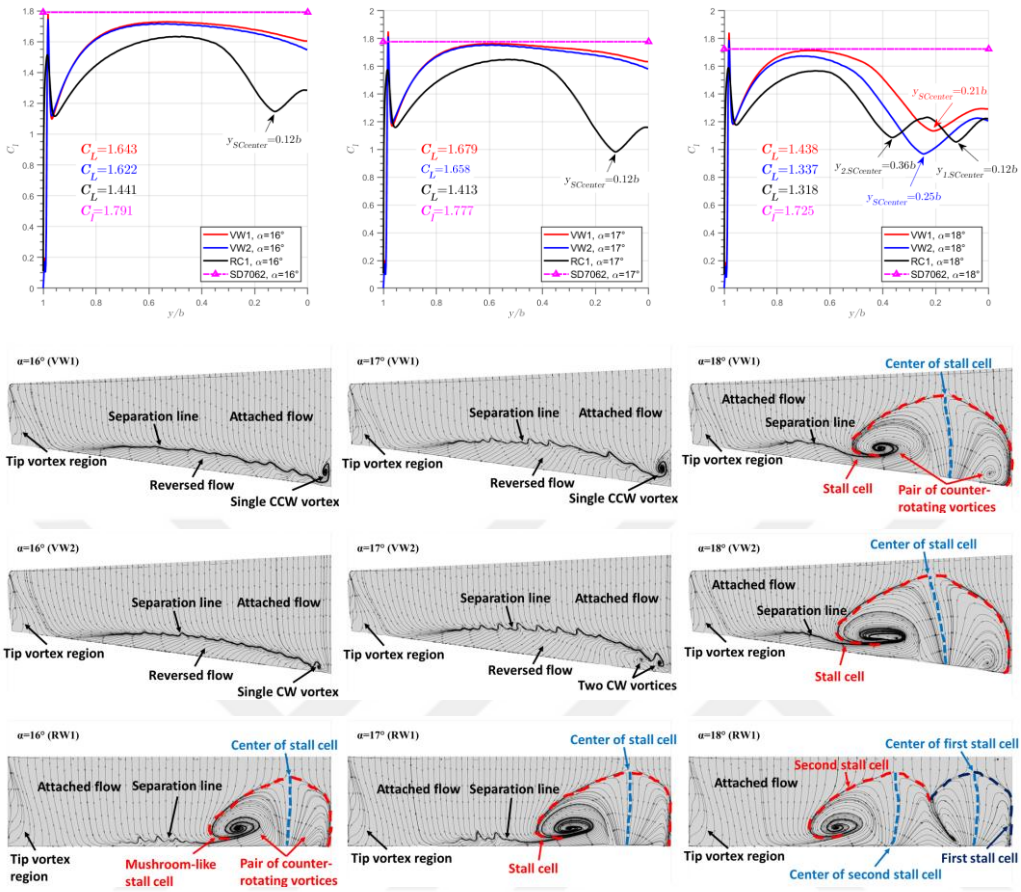


Figure 3.31: Comparison of mid-span sectional lift coefficient of VW1, VW2, RW1 and 2D SD7062 airfoil



(a) (b)

Figure 3.32: (a) Sectional lift coefficients along the spanwise direction, and (b) mean surface streamlines on the suction side of VW1 and RC1 at α=15°



(a) (b) (c)

Figure 3.33: Sectional lift coefficients, and mean surface streamlines at (a) α=16°, (b) α=17° and (c) α=18° for VW1, VW2 and RC1

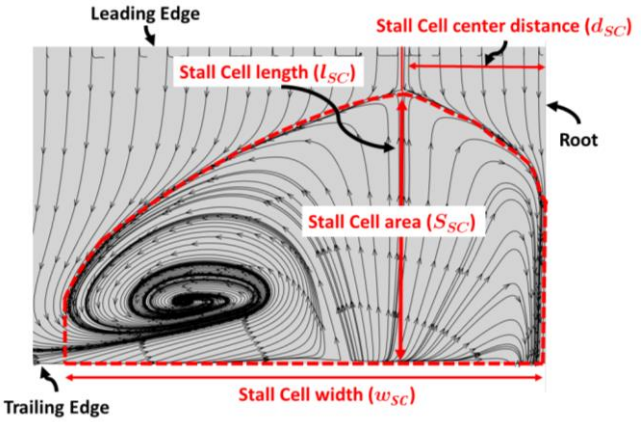
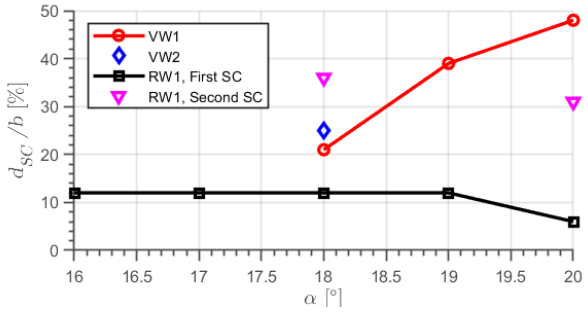
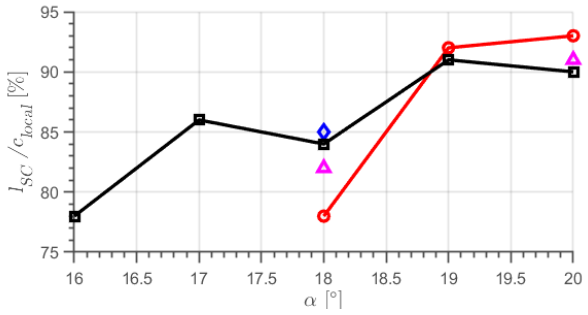


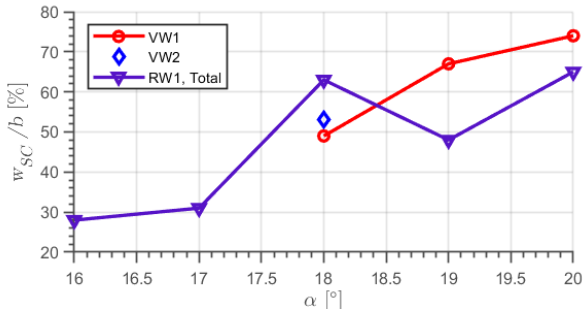
Figure 3.34: Schematic dimensions of the stall cell



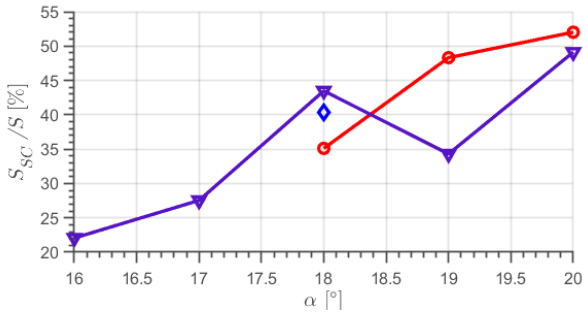
(a)



(b)

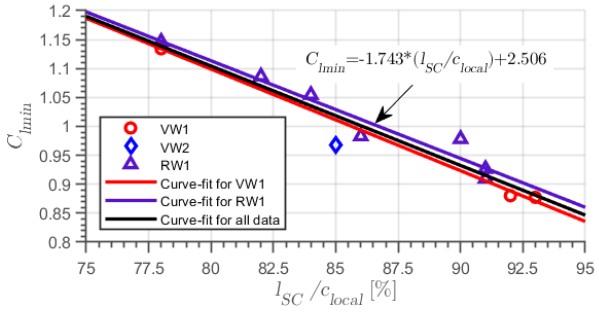


(c)

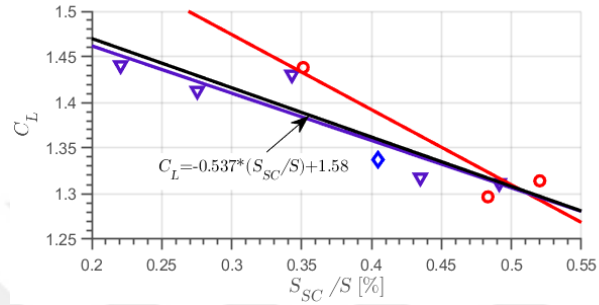


(d)

Figure 3.35: Variation of (a) d_{SC}, (b) l_{SC}, (c) w_{SC}, and (d) S_{SC} over angle of attack



(a)



(b)

Figure 3.36: Variation of (a) C_{lmin} with respect to l_{SC}, and (b) C_L as a function of S_{SC}

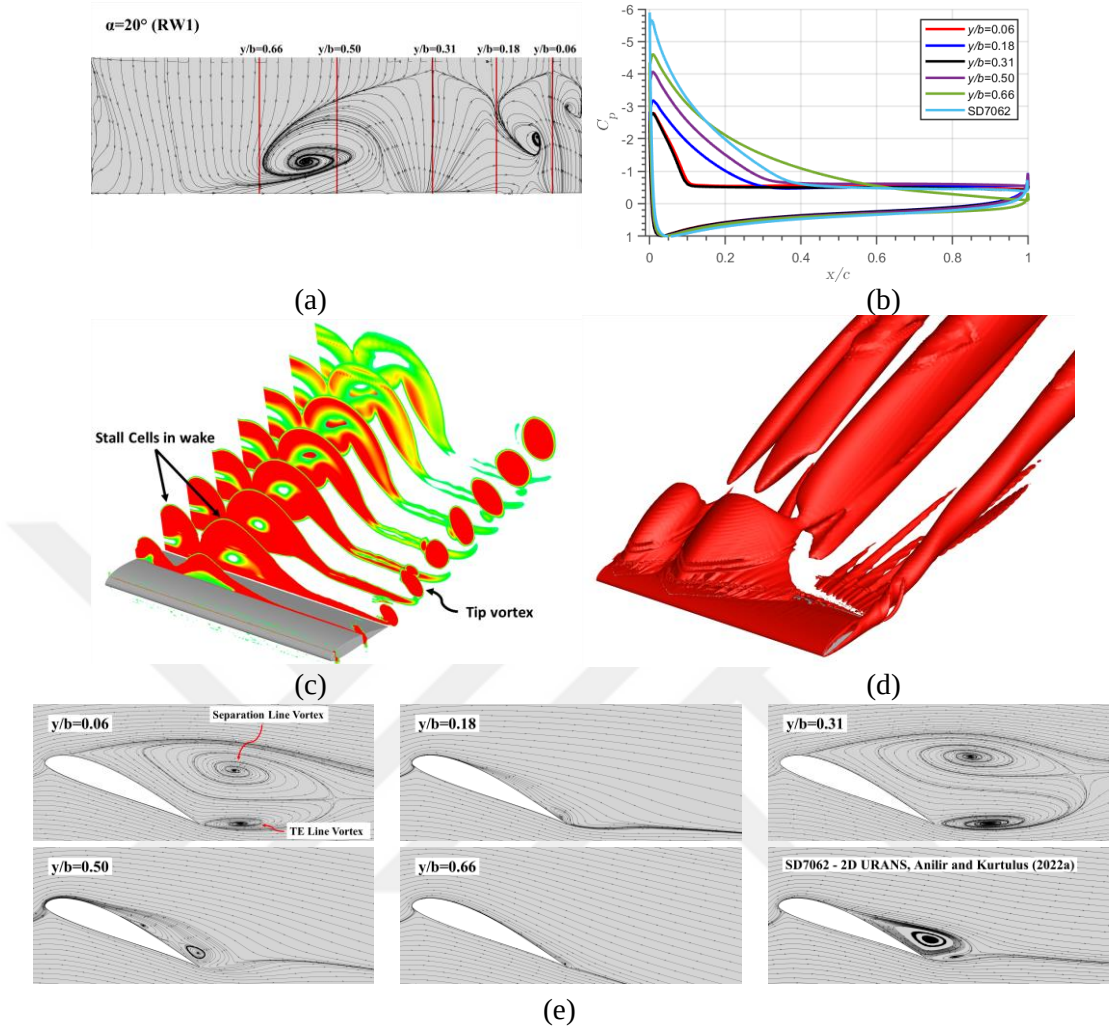


Figure 3.37: (a) Mean surface streamlines and location of the slices, (b) mean pressure coefficients, (c) vorticity magnitude contours in the wake, (d) iso-surfaces of Q-criterion ($Q = 20$), and (e) In-plane streamlines on y/b=0.06, 0.18, 0.31, 0.50 and 0.66 for RW1 and mean velocity streamlines around SD7062 airfoil at α=20°

CHAPTER 4

CONCLUSION

In this thesis, Unsteady Reynolds-averaged Navier-Stokes simulations have been performed for single SD7062 airfoil, SD7062 airfoil with the high cambered single-slotted flap and 3D Very Light Aircraft's wings.

For single SD7062 airfoil, the results are obtained from α=0° to α=30° where between α=0° to α=10° with 2° increment and between α=11° and α=30° with 1° increment. Also, the flow at α=19.5° and α=29.5° are investigated to identify the wake-mode change on the downstream wake of the airfoil. These analyses are performed at sea level standard atmospheric conditions at 0.156 Mach number. The stall angle of attack is observed at α=16° corresponding to mean lift coefficient of 1.7905. The second peak for the mean lift coefficient is observed beyond stall angle at α=24° having a value of 1.8206. The most efficient flight of SD7062 airfoil is reached at α=8° with $C_l/C_{d\ max}$=79.59.

An initial clockwise laminar separation bubble at the trailing edge on the suction side of the airfoil is revealed at α=12°. The separation point of the bubble moves on to the leading edge for every increment of angle of attack. The reattachment point of the separation bubble does not show any dependence on angle of attack until α=23°. Above this angle, the reattachment points also start to move towards the leading edge. The length and the height of the laminar separation bubble increase as the angle of attack increases except α=30° case. The length of the bubble reaches its maximum value l_{bmax}=0.804c at α=29°, and then it slightly decreases.

The first periodic oscillations in aerodynamic coefficients and vortex shedding on the wake of the airfoil are observed at α=19.5°. Three vortex patterns in the wake

are identified in the current study. These are Mode I "*continuous vortex sheet mode*", Mode II "*alternating vortex shedding mode*" and Mode III "*alternating vortex pair shedding mode*", and the angles of attack intervals correspond to $0°\leq\alpha\leq19°$, $19.5°\leq\alpha\leq29.5°$, and 30°, respectively. In Mode I, the vortices in the wake are steady, and there is no alternating vortex shedding observed. In Mode II, the first characteristic Strouhal number based on vortex shedding frequency is observed, equal to 1.289 at 19.5°. Also, the Strouhal numbers are gradually decreasing during Mode II with an increment of angle of attack. The alternating clockwise and counter-clockwise vortices (two single vortices) are observed in the wake of the airfoil. Mode III is characterized by two alternating vortex pairs that are co-rotating located above and below of centerline of the wake. The case with α=30° is the only case that shows a feature of Mode III. The sudden drop in Strouhal number is experienced at this angle of attack.

A selected number of three-dimensional URANS simulations for pre- and post-stall cases were performed to justify two-dimensional modeling at the given high Reynolds number regime. The results suggest that Mode I and II tend to remain two-dimensional without any three-dimensionality effect. Even for Mode III at a very high angle of attack, the flow does not show any spanwise instability. However, P+S wake-mode (Mode IV) is observed for three-dimensional simulations different than two-dimensional simulations of 2P mode.

For SD7062 airfoil with the high cambered single-slotted flap, the mean aerodynamic characteristics are obtained from α=-4° to α=20° with 2° increment for C-1, T-1, L-1, L-2, and L-3 configurations. The increase in the flap deflection significantly enhances the lift, but an increase in the drag penalty accompanies it. If the flap deflection is increased to a high angle with a larger gap size, a detrimental effect on the lift coefficient is observed. L-2 configuration proves superior aerodynamic performance compared to L-3 configuration considering each aerodynamic parameter despite having 5° lower flap deflection. The maximum lift coefficient of 3.302 is observed at α=14° for L-2 configuration.

The flow is fully attached to the boundary layer of the flap for T-1, L-1, and L-2 configurations at the stall angle of attack. However, the off-surface flow separation is observed in L-1, and L-2 configurations. Below the stall angle, the separation covers the aft portion of the flap for these two configurations. A huge separation bubble is observed for L-3 configuration for each angle of attack due to large gap size.

The effect of the gap size is numerically investigated on the overall performance of the two-element airfoil at landing condition with 40° flap deflection and a constant gap size of -0.004c for α=0° and α=12°. The optimum gap is found to be 0.016c. The off-surface flow separation is formed at α=12° for the optimum and the narrower gap sizes, whereas the flow is fully stalled for the wider gaps than the optimum gap.

For 3D wings simulations, the performances of the various 3D wings including a designed baseline Very Light Aircraft wing, which differs in taper ratio and dihedral angle, are compared at a Reynolds number of 5×10^6 and a wide range of pre- and post-stall angles of attack. The geometrical characterization of the stall cell, observed onset of the stall, is discussed in detail.

The effects of taper ratio and dihedral angle at small angles of attack are found to be negligible for the parameters investigated. The stall angles of 0.5 tapered wing with 0° and 5° dihedral (VW1 and VW2) are observed to be at about α=17° by considering the mean lift coefficients. On the other hand, the untapered wing with 0° dihedral (RW1) experiences the stall angle at α=15°. The two dimensional unsteady simulations of SD7062 exhibits the trailing edge stall at about α=16°. It is found that the stall angle of attack of the tapered wing is greater than 2D result, whereas the rectangular wing experiences the stall angle at a lower angle of attack compared to 2D airfoil. Although the drag forces generated by VW1 and RW1 at low to moderate angles of attack are very close to each other, RW1 generates considerably greater drag at large angles.

For all three studied wings, three-dimensional coherent structures, namely stall cells, are formed on the suction side just above the stall angle of attack. This structure significantly impacts the sectional distribution of lift forces, as the minimum sectional lift is examined at the stall cell center. The geometric constraints of the stall cell, which are center distance, length, width and area, are defined, and their variations with respect to the angle of attack are examined. The stall cells' length, width, and area mostly increase as the angle of attack increases. However, the width and area of the stall cells, formed on RW1, reduce at α=19° due to the disappearance of the second stall cell. The relation between lift forces and the stall cells' length, and area is investigated in order to observe the effect of the stall cell parameters on the lift. It is found that the lift force generally decreases as the stall cell parameter increases.

REFERENCES

Allen, E.C. (1953) *Experimental Investigation of the Effects of Plan-form Taper on the Aerodynamic Characteristics of Symmetrical Unswept Wings of Varying Aspect Ratio,* NACA RM A53C19.

Ananda, G.K., Sukumar, P.P. and Selig, M.S. (2015) 'Measured aerodynamic characteristics of wings at low Reynolds numbers', *Aerospace Science and Technology,* Vol. 42, pp.392–406.

Anılır, B. and Kurtuluş, D.F. (2023a) 'Unsteady aerodynamic performance of SD7062 airfoil at high Reynolds number', Progress in Computational Fluid Dynamics, Vol. 23, No. 2, pp.65–86.

Anilir, B. and Kurtulus, D.F. (2023b) 'Numerical investigation of SD7062 airfoil with single-slotted flap for different flight conditions', *Progress in Computational Fluid Dynamics,* in press.

Anilir, B. and Kurtulus, D.F. (2023c) 'Pre- and post-stall characteristics of a very light aircraft's wing for different design parameters', *Progress in Computational Fluid Dynamics,* in press.

ANSYS Inc. (2016) *ANSYS Fluent User's Guide, Release 17.2*.

Ashby, D.L. (1996) *Experimental and Computational Investigation of Lift-Enhancing Tabs on a Multi-Element Airfoil,* NASA TM-110432.

Bardina, J.E., Huang, P.G. and Coakley, T.J. (1997) *Turbulence Modeling Validation, Testing and Development,* NASA TM-1100446.

Boiko, A.V., Dovgal, A.V., Zanin, B.Y. and Kozlov, V.V. (1996) 'Three-dimensional structure of separated flows on wings (review)', *Thermophysics and Aeromechanics,* Vol. 3, No. 1, pp.1–13.

Boutilier, M.S.H. and Yarusevych, S. (2012) 'Parametric study of separation and transition characteristics over an airfoil at low Reynolds numbers', *Experiments in Fluids,* Vol. 52, No. 6, pp.1491–1506.

Brewer, J.D. and Fisher, L.R. (1951) *Effect of Taper Ratio on the Low-speed Rolling Stability Derivatives of Swept and Unswept Wings of Aspect Ratio 2.61,* NACA TN-2555.

Bruce, G.W. and McMasters, J.H. (1990) 'Computational aerodynamics applied to high-lift systems', *Progress in Astronautics and Aeronautics: Applied Computational Aerodynamics, AIAA,* Vol. 125, pp.389–433.

Burtsev, A., He, W., Zhang, K., Theofilis, V., Taira, K. and Amitay, M. (2022) 'Linear modal instabilities around post-stall swept finite wings at low Reynolds numbers', *Journal of Fluid Mechanics*, Vol. 944, p.A6.

Clark, C. (2018) *Measuring the Vortex-Shedding Frequency Behind Staggered Cylinders in Cross-Flow*, Mechanical Engineering MSc thesis, Santa Clara University, Santa Clara, USA.

Counsil, J.N.N and Boulama, K.G. (2013) 'Low-Reynolds-number aerodynamic performances of the NACA 0012 and Selig-Donovan 7003 airfoils', *Journal of Aircraft*, Vol. 50, No. 1, pp.204–216.

De Voogt, F. (2019) *Stall Cell Characteristics: An experimental investigation of the airfoil influence*, MSc thesis, Delft University of Technology, Delft, Netherlands.

De Voogt, F. and Ganapathisubramani, B. (2022) "Effects of a trailing-edge flap on stall cell characteristics of a NACA0012 wing," *Flow*, Cambridge University Press, Vol. 2, p.E15.

Dell'Orso, H. and Amitay, M. (2018) 'Parametric investigation of stall cell formation on a NACA 0015 airfoil', *AIAA Journal*, Vol. 56, No. 8, pp.3216–3228.

Dell'Orso, H., Tuna, B.A. and Amitay, M. (2016) 'Measurement of three-dimensional stall cells on a two-dimensional NACA0015 airfoil', *AIAA Journal*, Vol. 54, No. 12, pp.1–12.

Demel, D., Ferchichi, M., Allan, D.E.W. and Dghim, M. (2016) 'Two-dimensional experimental investigation on the effects of a fowler flap gap and overlap size on the wake flow field', *Journal of Fluids Engineering*, Vol. 139, No. 2, p.021101.

Drela, M. (1989) 'XFOIL: an analysis and de-sign system for low Reynolds number airfoils', *Low Reynolds Number Aerodynamics*, pp.1–12, Springer, Berlin, Heidelberg.

Faure, T.M., Drouet, V. and Montagnier, O. (2017) 'Discrete vortex method for a detached flow on a two-airfoil configuration at high angle of attack', *52nd 3AF International Conference on Applied Aerodynamics Progress in Flow Control*, *3AF*, Ecully, France.

Feryn, M.O. and Campbell J.F. (1965) *Effects of Wing Dihedral and Planform on Stability Characteristics of a Research Model at Mach Numbers from 1.80 to 4.63*, NACA TN D-2914.

Ferziger, J.H., Peric, M. and Street, R.L. (2020) *Computational Methods for Fluid Dynamics*, 4th ed., Springer, Switzerland.

Foster, D.N., Irwin H.P. and Willam B.R. (1970) 'The two-dimensional flow around a slotted flap' *Aeronautical Research Council Reports and Memoranda*, England, No. 3681, pp.1-69.

Garmann, D.J. and Visbal, M.R. (2017) 'Investigation of the unsteady tip vortex structure on a NACA0012 wing at fixed incidence', *55th AIAA Aerospace Sciences Meeting*, Grapevine, Texas, USA

Giguère, P. and Selig, M. (1997) 'Low Reynolds number airfoils for small horizontal axis wind turbines', *Wind Engineering*, Vol. 21, No. 6, pp.367-380.

Graham, M., Muradian, A. and Traub, L. (2017) 'Experimental study on the effect of gurney flap thickness on airfoil performance', *Journal of Aircraft*, Vol. 55, No. 2, pp.897–902.

Gudmundsson, S. (2014) *General Aviation Aircraft Design: Applied Methods and Procedures*, Butterworth-Heinemann, Oxford, UK.

Günther, B., Thiele, F., Petz, R., Nitsche, W., Sahner, J., Weinkauf, T. and Hege, H. (2007) 'Control of separation on the flap of a three-element high-lift configuration', *45th AIAA Aerospace Sciences Meeting and Exhibit*, Nevada, USA.

Guseva, E., Shur, M., Strelets, M., Travin, A., Breitenstein, W., Radespiel, P., Scholz, P., Burnazzi, M. and Knopp, T. (2018) 'Experimental/numerical study of turbulent wake in adverse pressure gradient', *7th Symposium on Hybrid RANS-LES Methods*, Berlin, Germany, pp.401–412.

Gutierrez-Castillo, P., Aguilar-Cabello, J., Alcalde-Morales, S. and Parras, L. (2021) 'On the lift curve slope for rectangular flat plate wings at moderate Reynolds number', *Journal of Wind Engineering & Industrial Aerodynamics*, Vol. 208, pp.1–8.

Helmbold, H.B. (1942) 'Der unverwundene ellipsenflugel als tragende flanche', *Jahrbuch*, pp.I111–I113.

Kurtulus, D.F. (2015) 'On the unsteady behavior of the flow around NACA 0012 airfoil with steady external conditions at Re=1000', *International Journal of Micro Air Vehicles*, Vol. 7, No. 3, pp.301–326.

Kurtulus, D.F. (2016) 'On the wake pattern of symmetric airfoils for different incidence angles at Re = 1000', *International Journal of Micro Air Vehicles*, Vol. 8, No.2, pp.109–139.

Li, W. and Liu, H. (2017) ‘Noise generation in flow over a full-span trailing-edge flap’, *AIAA Journal*, Vol. 55, No. 2, pp.561–571.

Lyon, C.A., Broeren, A.P., Giguère, P., Gopalarathnam, A. and Selig, M.S. (1997) *Summary of Low-Speed Airfoil Data, Vol. 3,* SoarTech Publications, Virginia Beach, Virginia.

Mamouri, A., Khoshnevis, B.A. and Lakzian, E. (2019) ‘Entropy generation analysis of S825, S822, and SD7062 offshore wind turbine airfoil geometries’, *Ocean Engineering*, Vol. 173, pp.700–715.

Manolesos, M. and Voutsinas, S.G. (2014) ‘Geometrical characterization of stall cells on rectangular wings’, *Wing Energy*, Vol. 17, pp.1301–1314.

McVeigh, M.A. and Kisielowski, E. (1971) *A Design Summary of Stall Characteristics of Straight Wing Aircraft,* NACA CR-1646.

Meena, M.G., Taira, K. and Asai, K. (2017) ‘Airfoil wake modification with gurney flap at low-Reynolds number’, *AIAA Journal,* Vol. 56, No. 4, pp.1348–1359.

Menter, F.R. (1994) ‘Two-equation eddy-viscosity turbulence models for engineering applications’, *AIAA Journal*, Vol. 32, No. 8, pp.1598–1605.

Moens, F. (2019) ‘Design of a generic wing model for basic stall phenomena’, *CASI 2019*, LAVAL, Canada.

O’Meara, M.M. and Mueller, T.J. (1987) ‘Laminar separation bubble characteristics on an airfoil at low Reynolds numbers’, *AIAA Journal*, Vol. 25, No. 8, pp.1033–1041.

Petrilli, J., Paul, R., Gopalarathnam, A. and Frink, N.T. (2013) ‘A CFD database for airfoils and wings at post-stall angles of attack’, *31st AIAA Applied Aerodynamics Conference*, San Diego, CA, USA.

Phillips, W.F. (2002) ‘Analytical solution for wing dihedral effect’, *Journal of Aircraft*, Vol. 39, No. 3, pp.514–516.

Ragni, D. and Ferreira, C. (2016) ‘Effect of 3D stall-cells on the pressure distribution of a laminar NACA64-418 wing’, *Experiments in Fluids*, Vol. 57, No. 8, pp.1–19.

Raymer, D.P. (2018) *Aircraft Design: A Conceptual Approach*, 6th ed., AIAA Education Series, Washington, DC, USA.

Ross, W.R. (1997) ‘Experimental studies of wake retardation in a simulated high-lift system flow field’, *AIAA 28th Fluid Dynamics Conference*, Snowmass Village, CO, USA.

Rossi, E., Colagrossi, A., Oger, G. and Le Touzé, D. (2018) ‘Multiple bifurcations of the flow over stalled airfoils when changing the Reynolds number’, *Journal of Fluid Mechanics*, Vol. 846, pp.356–391

Sadraey, M.H. (2014) *Aircraft Design A System Engineering Design*, John Wiley & Sons, Daniel Webster College, New Hampshire, USA.

Schnipper, T., Andersen, A. and Bohr, T. (2009) ‘Vortex wakes of a flapping foil’, *Journal of Fluid Mechanics*, Vol. 633, pp.411–423,

Selig, M.S., Donovan, J.F., and Fraser, D.B. (1989) *Airfoils at low speeds*, H.A. Stokely, Virginia Beach.

Shi, L., Yu, Z. and Jaworski, A.J. (2011) ‘Investigation into the Strouhal numbers associated with vortex shedding from parallel-plate thermoacoustic stacks in oscillatory flow conditions’, *European Journal of Mechanics*, B/Fluids, Vol. 30, No. 2, pp.206–217.

Smith, A. (1975) ‘High-lift aerodynamics’, *Journal of Aircraft*, Vol. 12, No. 6, pp.501–530.

Song, Q. (2012) *Design, Fabrication, and Testing of a New Small Wind Turbine Blade*, MSc thesis, University of Guelph, Canada.

Traub, L.W. (2000) ‘Effects of anhedral and dihedral on a 75-deg sweep delta wing’, *Journal of Aircraft*, Vol. 37, No. 2, pp.302–312.

Traub, L.W., Botero, E., Waghela, R., Callahan, R. and Watson, A. (2015) ‘Effect of taper ratio at low Reynolds number’, *Journal of Aircraft*, Vol. 52, No. 3, pp.734–747.

Traub, W.L. (2013) ‘Aerodynamic impact of aspect ratio at low Reynolds number’, *Journal of Aircraft*, Vol. 50, No. 2, pp.626-634.

Van Dam, C.P. (2002) ‘The aerodynamic design of multi-element high-lift systems for transport airplanes’, *Progress in Aerospace Sciences*, Vol. 38, No. 2, pp.101–144.

Washburn, K.E. and Gloss, B.B. (1975) *The Effects of Wing Dihedral and Section Suction Distribution on Vortex Bursting*, NASA TM X-72745

Wentz, W. and Fiscko, K. (1978) *Pressure Distributions for the GA(W)-2 Airfoil with 20% ai-leron, 25% Slotted Flap and 30% Fowler Flap,* NASA CR-2948.

Wentz, W.H.Jr., (1977), *Wind tunnel tests of the GA(W)-2 airfoil with 20% aileron, 25% slotted flap, 30% fowler flap and 10% slot-lip spoiler,* NASA CR-145139.

Wentz, W.H.Jr., and Ostowari, C. (1983), *Additional flow field studies of the GA(W)-1 airfoil with 30-percent chord Fowler flap including slot-gap variations and cove shape modifications*, NASA CR-3687.

Wentz, W.H.Jr., and Seetharam, H.C. (1974), *Development of a fowler flap system for a high performance general aviation airfoil*, NASA CR-2443.

Wilcox, D.C. (2006) *Turbulence modeling for CFD,* 3rd ed., DCW Industries, Inc., La Cañada, California.

Williamson, C. and Roshko, A. (1988) 'Vortex formation in the wake of an oscillating cylinder', *J. Fluids Struct.*, Vol. 2, No. 4, pp.355–381.

Winkelmann, A.E. (1982) 'An experimental study of mushroom shaped stall cells', *AIAA/ASME 3rd Joint Thermophysics, Fluids, Plasma and Heat Transfer Conference*, St. Louis, Missouri, USA.

Woodward, D.S., Hardy, B.C. and Ashill, P.R. (1988) 'Some types of scale effect in low-speed, high-lift flows', *16th Congress of the International Council of the Aeronautical Sciences,* Jerusalem, Israel, pp.1402–1416.

Worasinchai S., Ingram G. and Dominy, R. (2011) 'A low-Reynolds-number, high-angle-of-attack investigation of wind turbine aerofoils', *Proceedings of the Institution of Mechanical Engineers, Part A: Journal of Power and Energy*, Vol. 225, No. 6, pp.748-763.

Worasinchai, S. (2012) *Small Wind Turbine Starting Behaviour*. Ph.D. thesis, Durham University, Durham, England.

Wright, A.K. and Wood, D.H. (2004) 'The starting and low wind speed behavior of a small horizontal axis wind turbine', *Journal of Wind Engineering and Industrial Aerodynamics,* Vol. 92, No.14-15 pp.1265-1279.

Ying, S.X., Spaid, F.W., McGinley, C.B. and Rumsey, C.L. (1999) 'Investigation of confluent boundary layers in high-lift flows', *Journal of Aircraft,* Vol. 36, No. 3, pp.550-562.

Zarutskaya, T. and Arieli, R. (2005) ‘On vertical flow structures at wing stall and beyond’, *35th AIAA Fluid Dynamics Conference and Exhibit*, Toronto, Ontario, Canada.